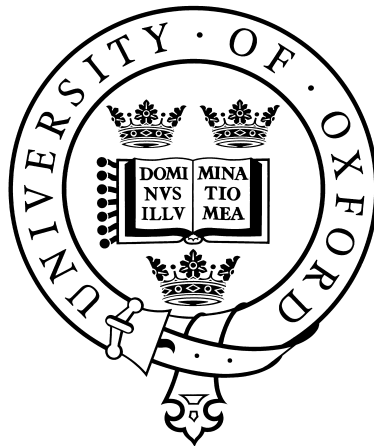


Generation of room-temperature entanglement in diamond with broadband pulses

Ka Chung Lee
New College, Oxford



Submitted for the degree of Doctor of Philosophy
Trinity Term 2012

Jointly supervised by
Prof. Ian A. Walmsley Prof. Dieter Jaksch

Clarendon Laboratory
University of Oxford
United Kingdom

To my parents.

Abstract

Since its conception three decades ago, quantum computation has evolved from a theoretical construct into a variety of different physical implementations. In many implementations, quantum optics is a familiar tool for manipulating or transporting quantum information. Even as some individual components of quantum photonics technologies have shifted from lab-based setups into commercial products, effort is being devoted to the creation of quantum networks that would link these components together to form scalable computation devices.

Here, I investigate optical phonons in bulk diamond, a previously overlooked system, as a physical resource for the construction of these devices. In this thesis, I measured the coherence properties of the diamond phonon, implemented a quantum memory write-read protocol using far-detuned Raman scattering, and entangled the phonon modes from two spatially separated pieces of diamonds in an adaptation of the seminal quantum repeater protocol proposed by Duan, Lukin, Cirac and Zoller (DLCZ). All of these experiments were conducted at room temperature with no optical pumping, using ultrafast broadband pulses (sub 100fs) — this is made possible by the unique physical properties of bulk diamond.

Quantum memories and the creation of entangled states are key ingredients towards a working quantum network. By demonstrating that diamond can be used as a bulk solid in ambient conditions to implement these complex quantum interactions, I show that bulk diamond is a credible candidate for the construction of robust integrated nanophotonics chips capable of operating at THz frequencies.

The quantum dynamics demonstrated here encompasses the motion of $\sim 10^{16}$ atoms, which is several orders of magnitudes larger than the excitations created in other systems. This manifestation of quantum features at room temperature, in a regime that is traditionally described classical physics, is of fundamental interest, and highlights the need for further studies into the transition between quantum and classical physics.

Acknowledgements

I would like to start by thanking my supervisors, Prof. Ian Walmsley and Prof. Dieter Jaksch, who first provided me with the opportunity to contribute to such an interesting project — not many physics students can drop in on a dinner conversation and say “Me? I work with diamonds, but no... really, let’s not talk about my work all the time...!”. Quantum information theory was my favourite part of the undergraduate physics course, and I feel genuinely lucky to have been able to contribute in whatever little way I could as a student researcher.

Of course, for this thesis to have ever happened, I have to give my thanks to Felix Waldermann, whose work on diamond formed such a well-defined starting point for me. Joshua Nunn, Karl Surmacz and Virginia Lorenz have lent me their infinite patience in getting me up to speed when I first joined the group. I am most grateful to Ben Sussman, my long-suffering postdoc (no doubt he would not dispute my choice of words here!) who tried to impart his considerable lab skills to me, and made sure my understanding of the theoretical aspects of the work did not stray too far from physical reality. To Michael Sprague, I can only say that I’ve enjoyed all of our time working together, and doubtless you will have many more publications in *Science* and *Nature* before the end of your DPhil! I also owe much to Nathan Langford and XianMin Jin, who, through their combined eloquence of speech and practicality of mind, persuaded me to make the changes critical to the success of the entanglement experiment. Without being able to name everyone in the Walmsley group by name, I would nonetheless like to give a shout out to Klaus Reim, Patrick Michelberger, Duncan England, and Tessa Champion, my fellow quantum memorisers who made the group that much more enjoyable to be a part of.

Having taken an extra long time to complete the DPhil, I have met and made many friends throughout my time at university. A fair proportion of them, such as John Weir and Lea Lahnstein, have shared my journey towards doctor-hood (albeit completed at a faster pace), and, by balancing my long nights in the lab with equally long nights of fun and games, made the whole experience all the more enjoyable. It was also thanks to the university dancesport lessons that I met my darling and best friend, Maxi Freund, who originally came to the UK for half a year, but subsequently decided to stick by me and has since then made me feel like the luckiest man everyday for the last 4+ years.

But the one constant factor through it all, of course, is the endless supply of home-cooked food and support that came from my parents, to whom this thesis is dedicated. While the “tiger mom” label associated with the stereotypical Asian

parents would be an over-the-top description of what you have been to me, it does describe very well the dedication and tenaciousness with which you have directed towards my upbringing since my baby years. From giving me your undivided tutoring attention in my pre-teenhood to relocating to a foreign country, you have made sure I have all the opportunities I would ever need to be able to get the best education available in the world.

This then brings me finally to perhaps an unusual point on which to finish this acknowledgement section, as it was through the inspiring physics lessons of Tony and Ruth Mead at the Skinners' School, Tunbridge Wells, that truly convinced me to take up physics at university. They have been ever so fantastic at putting up with my snide remarks in class while taking the time to give me glimpses of the most amazing scientific ideas through the simplest of explanations — I suppose that is what physics is really about.

Contents

1	Introduction	1
1.1	Motivation	1
1.2	Thesis outline	6
1.3	Quantum memories overview	7
1.3.1	Electromagnetically Induced Transparency (EIT)	10
1.3.2	Controlled Reversible Inhomogeneous Broadening (CRIB)/ Gradient Echo Memory (GEM)	14
1.3.3	Atomic Frequency Comb (AFC)	22
1.3.4	Raman absorption	24
1.4	A practical entanglement distribution device	31
1.4.1	Nitrogen-vacancy (NV) centres	32
1.4.2	Atomic ensembles	35
2	Stokes Scattering in bulk diamond	39
2.1	Optical phonons as a storage excitation	39
2.2	Raman scattering selection rules in diamond	43

2.2.1	Representation theory	44
2.2.2	Raman cross section	50
2.2.3	Measurements of the selection rule	53
2.2.4	LO/TO phonon	56
2.3	Transient Coherent Ultrafast Phonon Spectroscopy	61
2.3.1	Experiment	64
2.3.2	Results	67
2.3.3	Theory	70
2.3.4	Experimental conditions	80
2.3.5	Discussion	81
2.3.6	Notes on experimental apparatus	83
3	Anti-Stokes readout in diamond	88
3.1	There's something about the phonon...	88
3.2	Theory of Stokes/anti-Stokes production	89
3.3	Population and coherence lifetimes	92
3.4	Anti-Stokes polarisation selection rule	94
3.5	Raman coupling strength	96
3.5.1	Measurement	96
3.5.2	Numerical model	98
3.6	Experimental demonstration of nonclassical motion	
	in bulk diamond	102
3.6.1	Cauchy-Schwarz inequality and quantumness	103

3.6.2	Pump preparation	105
3.6.3	Experimental setup	108
3.6.4	Observation of Cauchy-Schwarz violation	110
3.6.5	Quantum memory interaction	116
3.6.6	Experimental considerations	120
3.6.7	Directional emission	124
3.7	Stimulated Anti-Stokes Ultrafast Correlated Excitation Radiation Spec-	
	troscopy	125
3.7.1	Diamond samples	126
3.7.2	Measured lifetimes	128
4	Diamond Entanglement	131
4.1	The experiment	133
4.1.1	Setup	133
4.1.2	Theory	135
4.2	Experimental techniques	139
4.2.1	Alignment of translation stage	140
4.2.2	Fibre coupling	142
4.2.3	Pulse synchronisation	144
4.2.4	Phase stabilisation	145
4.2.5	Anti-Stokes phase control	148
4.3	Results	149
4.3.1	Anti-Stokes interference	149

4.3.2	Concurrence	154
4.3.3	Quantum (reduced) state tomography	160
5	Conclusions	163
5.1	Summary	165
5.2	Outlook	167

List of Figures

1.1	Illustration of various quantum memory schemes.	8
1.2	Absorption and dispersion of resonant light in an EIT active atomic ensemble.	11
1.3	Schematic of the CRIB memory protocol.	16
1.4	Schematic of Hétet <i>et al.</i> 's version of the GEM memory protocol. . .	18
1.5	HYPER/ROSE memory protocol.	21
1.6	Absorption profile of the atomic ensemble in the AFC memory protocol.	22
1.7	Schematic of Stokes and anti-Stokes scattering.	25
1.8	Comparison of state population evolutions in a λ -system using the full Hamiltonian and using the adiabatic approximation.	27
1.9	Structure of NV^- centre.	33
1.10	Schematic of the DLCZ entanglement protocol.	35
2.1	The diamond lattice.	40
2.2	Phonon dispersion relation in diamond.	41
2.3	Irreducible representations of the D_4 group.	44

2.4	Diagrammatic representation of the Raman scattering process.	51
2.5	Schematic of the setup used to verify the polarisation selection rule of Raman scattering.	53
2.6	Measured polarisation selectivity of the Stokes photons.	54
2.7	Geometry of Stokes scattering.	56
2.8	1D and 2D scattering cross section of Raman signal.	58
2.9	Proportion of Stokes light scattered from the TO branch as a function of collection angle.	60
2.10	TCUPS experimental setup.	63
2.11	Stokes scattering transition in diamond.	63
2.12	Cross polarised images of different diamond samples measured in TCUPS.	66
2.13	Stokes spectral fringe at various pump delays in TCUPS.	68
2.14	Spectral fringe visibility versus pump delay.	69
2.15	The first order Raman spectra of the diamond samples.	71
2.16	Schematic of phonon evolution in the TCUPS pulse sequence.	76
2.17	Pump spectral fringe visibility as a function of optical delay.	84
2.18	Numerical simulation of pump spectral visibility measured by the Andor spectrometer.	86
3.1	Polarisation selectivity of anti-Stokes light.	94
3.2	Pump power scaling of unheralded Stokes and anti-Stokes emissions.	97
3.3	Power scaling of Stokes to anti-Stokes ratio.	98

3.4	Numerical simulation of Stokes photon number state population at different coupling strengths.	101
3.5	Pump pulse preparation setup.	105
3.6	Chromatic aberration with a normally dispersive focussing lens.	107
3.7	SAUCERS experimental setup.	108
3.8	Auto-correlation of Stokes field.	111
3.9	Nonclassical correlation of Stokes and anti-Stokes photons produced from a quantum memory interaction.	112
3.10	Theoretical model of Stokes field auto-correlation decay in the presence of noise.	115
3.11	Population and coherence of non-classical phonons versus read-write delay.	117
3.12	Schematic of the collective optical density of the 3 notch filters used for pump rejection after the diamond.	120
3.13	Setup to measure Stokes-to-pump ratio as a function of d	122
3.14	Ratio of Stokes to pump photons as a function of Fresnel power.	123
3.15	UV photoluminescence images of different diamond samples.	127
3.16	Population and coherence lifetimes of diamond phonons.	128
4.1	Experimental layout for the generation of entanglement between two diamonds.	134
4.2	Schematic of the alignment process for the translation stage.	140
4.3	Free space coupling into Andor spectrometer.	143

4.4	Pump phase stabilisation with a feedback loop.	147
4.5	Interference of readout anti-Stokes photons.	150
4.6	Plot of maximal interference visibility as a function of the cross- correlations from two diamonds.	151
4.7	Density matrix of the heralded anti-Stokes modes.	156
4.8	Reconstructed joint polarisation state of the Stokes/anti-Stokes modes, projected into the sub-space containing one photon in each mode. . .	160

Chapter 1

Introduction

1.1 Motivation

Humans' evolutionary progress rests, to a large degree, on our ability to process information^[1]. Our ever increasing capability to generate information in recent decades is, in turn, driven by our mastery of the computing technologies^[2]. Computers operate by flipping internal switches, whether they are transistors, vacuum tubes or even mechanical hammers, between 2 different states, which we label $|0\rangle$ and $|1\rangle$, to execute instructions at great speed. However, it is worth noting that despite all the technological innovations, each internal switch is fundamentally no more powerful than a single bead from the humble abacus, first invented in Sumeria around 4,500 years ago. As such, the classical computer can not implement any algorithms that are more efficient than what their less sophisticated counterparts can do.

On the other hand, each *qubit*, which is the equivalent of a switch in a quantum computer, can be in a superposition state $|\psi\rangle = c_0|0\rangle + c_1|1\rangle$ with amplitudes c_0, c_1 , and $|c_0|^2 + |c_1|^2 = 1$. In general, the amplitudes are complex numbers and, for a classical computer to simulate an n -qubit quantum computation problem, 2^n complex numbers would have to be stored and then processed. Shor's factorisation algorithm^[3], amongst others^[4], leverage this property to provide an exponential speed up over their equivalent, best known algorithms that can be implemented on classical computers.

The first direct proof that quantum computers can be more than a theoretical concept came in 1995, when Monroe *et al.*^[5] implemented a controlled-NOT gate on a single trapped ion, using the two lowest levels of the harmonic trap states as the control qubit acting on the internal spin states of a ${}^9\text{Be}^+$ ion. Three years later, Jones and Mosca^[6] implemented a quantum algorithm for the first time using Nuclear Magnetic Resonance (NMR) techniques. There, they utilised two coupled proton spin states as a test bed to solve Deutsch's problem^[7] of determining the parity of a one bit function $f : X \rightarrow Y$, where $\{X, Y\} \in \{0, 1\}$. The two spins are placed, one each, into the superpositional states $|\psi^\pm\rangle = (|0\rangle \pm |1\rangle)/\sqrt{2}$ (where $\{|0\rangle, |1\rangle\}$ are the proton spin eigenstates), which act as the function input X . By using the superposition states $|\psi^\pm\rangle$, Jones and Mosca were able to determine the parity with one rather than two queries (minimum required by a classical computer) of any function f . Since then, quantum logical operations have been demonstrated on multiple NMR qubits^[8], though more recent efforts have mainly been directed

at a growing plethora of other systems, as demonstrated by the implementations of Grover's search algorithm in trapped ions^[9] and superconducting circuits^[10], as well as Shor's algorithm in photonic chips^[11].

In order for quantum computation technologies to function alongside, or even replace, current computing architectures, spatially separated quantum computers should have the ability to transmit and share quantum information. Just as the internet has been a paradigm shift of transforming the standard computer from being a standalone glorified typewriter to being *the* indispensable tool for banking and keeping up-to-date with friends, quantum communications protocols have opened up an entirely new range of capabilities for quantum technologies. This includes the well known quantum key distribution protocol conceived by Bennett and Brassard in 1984^[12], which underlies the current generation of commercial systems that promise unconditional security, and teleportation of arbitrary quantum states, first proposed by Bennett *et al.* in 1993^[13] and demonstrated by Bouwmeester *et al.* four years later^[14].

Many quantum communication protocols, including the above examples, rely on the ability to distribute *entangled* states across spatially separated network nodes. When a multi-partite system is entangled, complementary measurements on each particle produce correlated results in a manner which is inconsistent with classical theories — a feature that Einstein dismissed as *spukhafte Fernwirkungen* (spooky actions at a distance)^[15]. In particular, quantum repeater protocols, such as the famous DLCZ scheme by Duan *et al.* in 2001^[16], have the potential to distribute

bi-partite entangled states across distant (inter-continental) nodes. Many variations have been proposed since, and form an area of active research^[17,18].

Key to entanglement distribution and, by extension, a quantum network, is the ability to send quantum information, the *flying qubit*, across network channels, to be processed at the nodes, in the form of *stationary qubits*. Due to its speed, photons represent a natural choice as the medium for a flying qubit. Indeed, Knill *et al.*^[19] have shown in 2001 that linear optics is a feasible approach towards quantum computation, and the *quantum memory*, a device capable of storage and retrieval of the flying qubit, plays an important role in scalable linear optical quantum computing^[20]. Quantum memories can improve single photon production rates (thereby reducing the overhead for optical quantum computing^[21,22]), synchronise multiple single photon sources^[23] as well as being a fundamental building block for quantum repeater networks.

Early studies (from the 1960s) into quantum optics, where the creation/annihilation operator formalism is central to the understanding of light-matter interactions, mainly involved single or few atoms^[24,25]. The weak interaction strengths in these experiments can be ameliorated by placing the atom in a cavity^[26,27]. In general, however, addressing a single atom is a technically challenging task. An alternative approach to enhancing the interaction strength is to use an ensemble of atoms^[28–31]. Here, a single *readin* signal photon can interact with many atoms (e.g. $\sim 10^9$ in a recent demonstration by Reim *et al.*^[32]) and the quantum state of the photon is coherently mapped into a collective excitation of the ensemble before being transferred

into a *readout* photon.

Tremendous progress has been made in recent years on increasing storage efficiencies and lifetimes in ultracold and hot atomic gases, rare-earth-ion (RE) doped crystals as well as other systems^[17,33]. However, they typically require significant resource overhead in their preparation and utilisation, especially when cryogenic techniques are employed. Significant technical challenges remain before these systems find their way into a practical quantum computational device.

In contrast, current computers are already capable of robust operations at room temperature, and lithographic techniques allow features which are 32 nm and smaller to be etched onto a chip^[34]. It is therefore not unreasonable to expect a future practical optical quantum computer to take the form of a nano-photonics device. Here, the quest for a suitable solid in which quantum effects can be observed revolve around two principle materials: silicon, a commonly utilised material for which there already exist a wealth of fabrication techniques^[35]; and diamond, whose stiff lattice structure gives it extraordinary physical properties^[36]. Defect centres in these crystals, consisting of electrons sitting in vacant lattice sites that act as cavities to shield it from the environment, hold one promising route to room temperature quantum computation^[37,38]. While bulk silicon is regularly used in waveguide research^[39,40], its defect centres, such as the oxygen-vacancy in silicon^[41] and isolated vacancies in silicon carbide (SiC), are less well characterised. Atom light interactions in silicon based materials are still at a relatively early stage of development.

Diamond, on the other hand, is already well utilised in a broad range of ap-

plications. For instance, the QCV SPS 1.01 is a commercial single photon source that relies on diamond's nitrogen-vacancy (NV) centres for stable room temperature operations. As diamond consists of the same carbon atoms which make up the human body, nano diamonds are bio-inert and have been used as a fluorescent tracker for real time bio-imaging applications^[42]. Further, acoustic vibrational waves in diamonds have long coherence lengths^[43], leading to diamond having the highest thermal conductivity of any naturally occurring materials. This means that bulk diamond is particularly adept in environments where high thermal loads are expected, and is partly why diamond has been used as the lasing medium of mode-locked picosecond lasers^[44]. With so many proven abilities, it is most likely that diamond will play an important role in the development of thermally robust nano-phonic structures.

1.2 Thesis outline

This thesis is in five chapters. Chapter 1 discusses the importance of entangled states and the role of the quantum memory in achieving scalable quantum computing. An introduction to various quantum memory protocols is given, alongside a review of some experimental approaches towards practical entanglement distribution. Chapter 2 introduces the diamond phonon as a storage excitation, discusses its role in the Stokes scattering process and its use as a spectroscopic tool for diamond (TCUPS). A phonon excitation created by Stokes scattering can be read out by anti-Stokes scattering, and chapter 3 analyses the Stokes/anti-Stokes photon pair

to demonstrate nonclassical behaviour from bulk diamond. This experiment is then adapted as a complementary spectroscopic technique on diamond (SAUCERS), and the results are combined with TCUPS to gain new insights into the material properties of diamond. Extending the setup used for anti-Stokes scattering, chapter 4 reports the creation of the first macroscopic room temperature entanglement using two spatially separated diamonds — where it turns out that the verification process is arguably somewhat more complicated than the entanglement creation. Chapters 2 to 4 are all based on published papers. Finally, chapter 5 concludes this thesis with an outlook on future work.

1.3 Quantum memories overview

A quantum memory functions by coherently mapping a readin signal photon state into a medium excitation (a storage state), which is then read out again into a readout signal photon. In order to preserve the coherence of the stored quantum state, the storage state is usually a long-lived metastable state that is coupled via an intermediate state to the ground state. Figure 1.1 illustrates a selection of quantum memory protocols — Electromagnetically Induced Transparency (EIT), Controlled Reversible Inhomogeneous Broadening (CRIB), Atomic Frequency Comb (AFC) and far-detuned Raman memory — that are based on systems with this type of energy structures, normally known as Λ systems.

For single atoms, each energy level represents an eigenstate of the electronic wavefunction, and the memory lifetime is, in principle, only limited by the lifetime

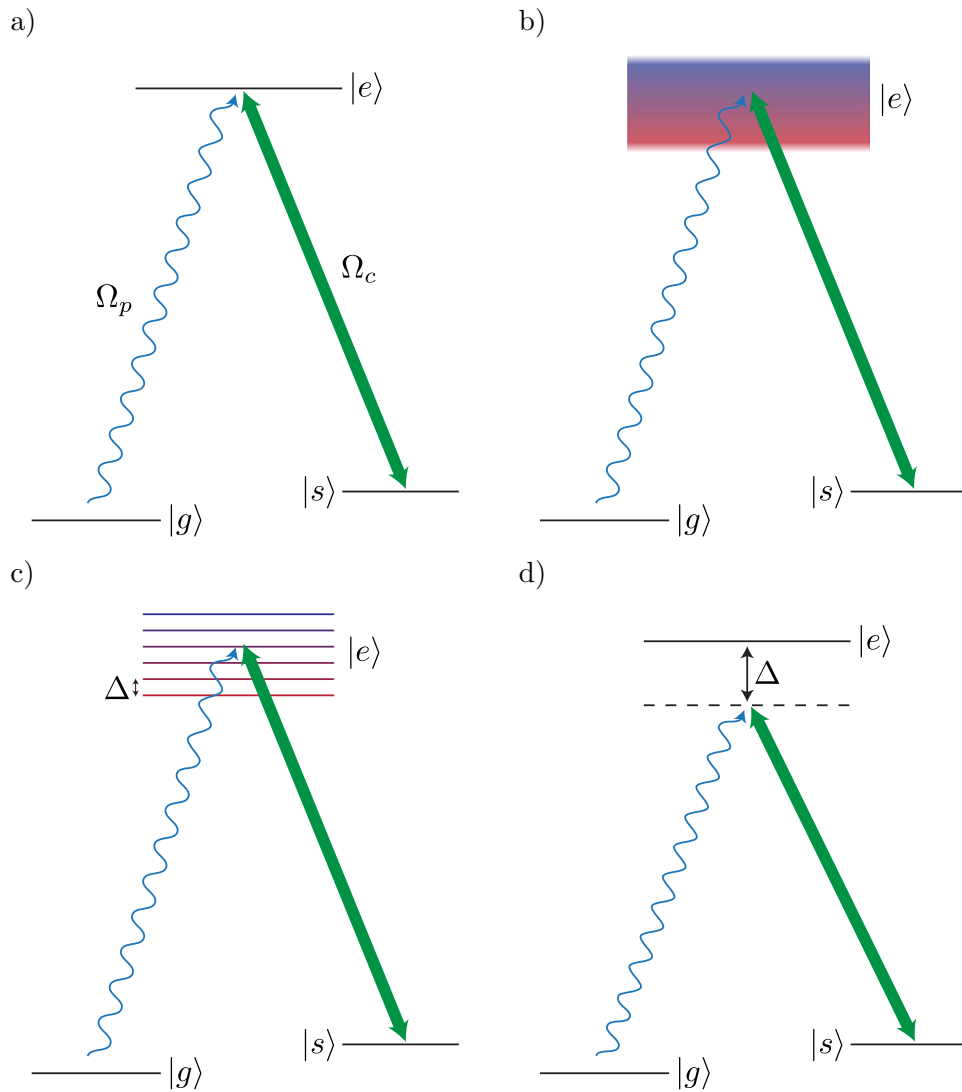


Figure 1.1 Illustration of various quantum memory schemes. In all cases, the bold green arrow represent a strong classical control pump, and the blue wavy arrow represents the weak signal field that is stored and retrieved: a) In EIT, a control field induces a Stark shift on the upper state $|e\rangle$ such that the medium becomes transparent to the signal field, and the group velocity of the signal is also reduced. Absorption of the signal into the storage state $|s\rangle$ is achieved by adiabatically decreasing the pump intensity. CRIB b) and AFC c) are both photon echo techniques. The resonant signal fields are absorbed by the artificially broadened upper level $|e\rangle$. At time $t = \tau$, the applied broadening in CRIB is reversed and the manifold of states $|e\rangle$ rephase to emit the signal field at $t = 2\tau$. For AFC, rephasing occurs naturally at $t = 2\pi/\Delta$. A classical π pulse can transfer the excitation from $|e\rangle$ to a meta-stable $|s\rangle$ to prolong the storage time. Finally, in d), we show the Raman memory, where the signal is directly absorbed into and later re-emitted from the state $|s\rangle$ via the far-detuned (Δ is much greater than signal bandwidth) Raman interaction.

of the excitation $|s\rangle$. The weak coupling from the photon field to atomic excitations is a major technical barrier that has only just been overcome recently by Specht *et al.*^[27] with a high-finesse cavity, which led to a storage efficiency of 9.3%. Though, once stored, the coherence time of the dipole trapped ^{87}Rb atom was found to be $184\ \mu\text{s}$ (compared to an input pulse duration of $0.7\ \mu\text{s}$).

As mentioned in the previous section, replacing the atom/high-finesse cavity combination with an atomic ensemble is an experimentally straightforward approach to strengthen the light-matter interaction. In this case, the ensemble contains many copies of the Λ structure, and, instead of a single ground state (Fig. 1.1), $|g\rangle$, for instance, now stands for the product of N individual ground states $|g\rangle \equiv |g_1 g_2 \dots g_N\rangle$, where g_i represents the ground state of atom i . As a single signal photon is absorbed during the readin process, a *collective* excitation is created such that the ensemble is in a superposition of all combinations of 1 excited atom with $N - 1$ ground state atoms. Instead of representing the meta-stable state of one single atom,

$$|s\rangle \equiv \frac{1}{\sqrt{N}} \sum_i^N c_i |g_1 g_2 \dots s_i \dots g_N\rangle. \quad (1.1)$$

The magnitudes and phases of the complex amplitudes $\{c_i\}$ are determined by the propagation of light through the atomic medium and the positions of atom i within the ensemble. The state in Eq. (1.1) is also known as a *spin wave* in the literature since it takes a similar form to how disturbances to atomic alignments in a magnetic material travel.

To illustrate the increase in interaction strength with an ensemble over that of a free space single atom, we start with an interaction Hamiltonian \hat{H}_1 and look at the diagonal element $\langle 0, s | \hat{H}_1 | 1, g \rangle$, where $|1, g\rangle$ describes the initial system with 1 signal photon and ensemble ground state, coupled to a final state with 0 signal photon and ensemble storage state Eq. (1.1). For a signal photon annihilation operator \hat{a}_s and single atom-light coupling constant α (approximated as being equal for all atoms in the ensemble),

$$\hat{H}_1 = \alpha \hat{a}_s \otimes \sum_i^N |s_i\rangle \langle g_i| + \text{h.c.} \quad (1.2)$$

In the weakly interacting regime, all atoms interact equally with the light field, and $c_i = 1$ ^[45]. The effective coupling constant in this toy model is given by $\langle 0, s | \hat{H}_1 | 1, g \rangle = \alpha \sqrt{N}$. From this, it is clear that the collective coupling strength is enhanced over the single atom case by a factor of the square root of the number of atoms, which can be extremely large for a typical atomic ensemble. Due to propagation and high order effects, storage efficiencies do not scale simply as the effective coupling constant. Efficiencies of the various memory protocols have been analysed, for example, by Nunn *et al.*^[46] and Gorshkov *et al.*^[47]

1.3.1 EIT

In 2001, two groups, Liu *et al.*^[48], and Philips *et al.*^[28] separately demonstrated working quantum memories for the first time using the well established technique of Electromagnetically Induced Transparency (EIT)^[49,50]. The storage process of EIT can broadly be divided into 2 parts: first, a strong control field is applied on

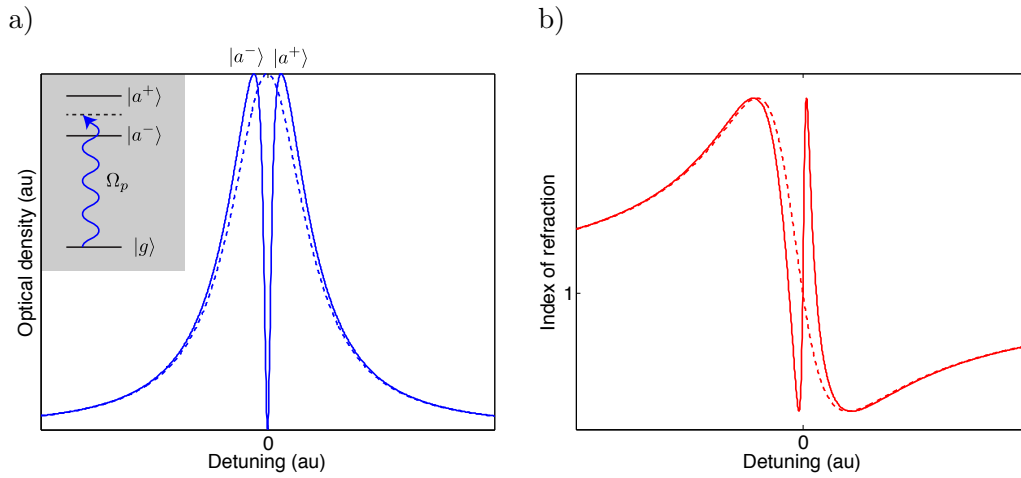


Figure 1.2 In the presence of a strong resonant control (solid lines), a) a transmission window in the medium is opened within a normally absorptive range of frequencies (dashed line representing resonance without the strong control field). The inset shows a dressed state picture of the lambda system shown in Fig. 1.1a — the resonant signal field is transmitted by the medium in the presence of a strong control pump (see text). b) A rapid variation is also introduced in the refractive index around the resonance of the medium such that the group velocity of a signal pulse is reduced. Normal absorption profile and refractive index around the $|s\rangle \rightarrow |e\rangle$ transition are represented by dotted lines.

the $|s\rangle \rightarrow |e\rangle$ transition with coupling Ω_c (Fig. 1.1a), which dresses the excited state such that the transmissive property of the medium is altered, and a weak signal that is resonant with the $|g\rangle \rightarrow |e\rangle$ transition, coupling Ω_p , is no longer absorbed (Fig. 1.2). In the rotating frame, representing a linear combination of the bare atomic eigenstates $|\psi\rangle = \Psi_g|g\rangle + \Psi_s|s\rangle + \Psi_e|e\rangle$ by the vector (Ψ_g, Ψ_s, Ψ_e) , the

interaction Hamiltonian is:

$$\hat{H}_I = -\frac{\hbar}{2} \begin{pmatrix} 0 & 0 & \Omega_p \\ 0 & 0 & \Omega_c \\ \Omega_p^* & \Omega_c^* & -2\Delta \end{pmatrix}, \quad (1.3)$$

where Δ represents a small (red) detuning of the Ω_p, Ω_c fields away from the excited state $|e\rangle$. We assume that the excited state does not decay in this simple model. When operating as a single photon quantum memory, $\{\Omega_p, \Delta\} \approx 0$, and the eigenstates of \hat{H}_I , i.e. dressed states, are:

$$|a^\pm\rangle = \frac{1}{\sqrt{2}}(|s\rangle \pm |e\rangle), \quad (1.4)$$

with the associated eigenvalues:

$$\hbar\omega^\pm = \frac{\hbar}{2}(\Delta \pm \sqrt{\Delta^2 + \Omega_p^2 + \Omega_c^2}). \quad (1.5)$$

Thus a strong control field renders the medium transparent to the signal field (Fig. 1.2a inset). At the same time, the dispersion of the medium is also changed, so as to reduce the group velocity of the signal pulse^[51]. The pulse length is simultaneously compressed and, as the control field is adiabatically switched off, the group velocity of the signal photon reduces to zero. The energy of the portion of the compressed signal which fits inside the storage medium is coherently transferred into an atomic excitation. To retrieve the signal pulse, the control field is adiabatically

turned back on at a user determined time, and the atomic excitation is coherently transferred back into the photon field.

In practice, Δ is chosen to be finite, but within a *resonance limit* of $\Delta \ll d\gamma_{ge}$, where d is the resonant optical depth of the ensemble and γ_{ge} is the decay rate of the $|e\rangle \rightarrow |g\rangle$ transition^[45]. The detuning reduces collision induced fluorescence during the storage and retrieval steps, thereby improving the signal to noise ratio (a crucial criteria when experimenting at the single photon levels)^[52]. Further, within the resonance limit, EIT storage/retrieval efficiency is not particularly sensitive to Δ ^[45,52–54], therefore EIT can be implemented even in mediums which have inhomogeneously broadened $|e\rangle$ without optical pumping. For example, while Liu *et al.* used magnetically trapped sodium atoms, Philips *et al.* used rubidium vapour at 70 – 90°C, and both demonstrated roughly equal storage times.

The transparency window of EIT lies between ω^\pm and scales with the pump intensity [Eq. (1.5)] — though a more careful analysis shows that the window is narrower for a given pump power in the presence of inhomogeneous broadening of $|e\rangle$ ^[54] — thus defining a minimum signal pulse duration that can be stored. At the same time, the compressed pulse must physically fit inside the storage ensemble, thereby placing an upper bound on the duration.

In the initial single photon experiments, caesium (Cs) or rubidium (Rb) atoms were held in a Magneto-Optical Trap (MOT) and used to store $\sim 0.1 \mu\text{s}$ signal photons for typically $0.5 \mu\text{s}$ ^[55,56]. These demonstrations were later extended to warm gases — e.g. Eisaman *et al.* measured a decay time of $1 \mu\text{s}$ for Rb gas using

140 ns long pulses and a combined storage and retrieval efficiency of 10%^[57]. A problem with the warm gases is that the atoms can diffuse out of the interaction volume in between the storage and retrieval processes, and this happens on the timescale of μs . Doped solids, on the other hand, allow the relevant atoms (the doping material) to be held in place like a ‘frozen gas’. As such, praseodymium (Pr) doped in Y_2SiO_5 was the material first used by Turukhin *et al.*^[58] to observe EIT and a subsequent experiment by Longdell *et al.* measured the storage time to be an astonishing 2.3 s^[59] (compared to a 20 μs long signal pulse). However, the exact energies of each Pr atom are highly dependent on the surrounding solid, contributing to significant pure dephasing effects. In these experiments, the solids are held at cryogenic temperatures and a rephasing pulse is applied in the middle of the storage time. This represents a slight drawback on its use as a quantum memory since, to maximise the potential of the medium, the user must then decide when the stored signal will be retrieved before the storage step in order to know when to apply the rephasing pulse.

1.3.2 CRIB/ Gradient Echo Memory (GEM)

In general, inhomogeneous broadening in the storage medium decreases the fidelity of the retrieved signal. A class of protocols, called *photon echo* techniques, can, in principle, use the inhomogeneous broadening instead to store optical pulses. Suppose an ensemble of two level atoms absorbs a single photon on the $|g_i\rangle \rightarrow |e_i\rangle$ transition,

the ensemble is in the state:

$$|e\rangle = \sum_i c_i e^{i\delta_i t} |g_1 g_2 \dots e_i \dots g_N\rangle, \quad (1.6)$$

where δ_i is the frequency shift of the i th atom due to inhomogeneous broadening. Analogous to the Hahn echo technique in NMR^[60], suitable application of π pulses can effectively reverse the shifts such that $\delta_i \rightarrow -\delta_i$ half way through the storage process and allow the atoms to rephase and emit the stored signal (providing the storage time is much shorter than the lifetime of the medium). However, Ruggiero *et al.*^[61] have shown that the storage fidelity is very sensitive to the applied pulse area, and the fluorescence noise following the application of the π pulse would significantly degrade the signal to noise ratio. Further, after applying the rephasing pulse, the population of the atomic ensemble would be inverted, leading to the emission of amplified spontaneous noise^[62], thus such a ‘traditional’ approach cannot work at the single photon level.

Moiseev and Kröll proposed, in 2001, a technique that is now known as Controlled Reversible Inhomogeneous Broadening (CRIB), which provides an alternative route to reversing the shifts δ_i ^[30]. The protocol is as follows (Fig. 1.3): to initialise the ensemble, selective optical pumping creates a spectral hole within the absorption profile of the medium and a narrow anti-hole at the centre. An external field induces different Stark or Zeeman shifts on the atomic transitions so as to broaden the anti-hole peak. The storage process is simply the resonant absorption of a signal

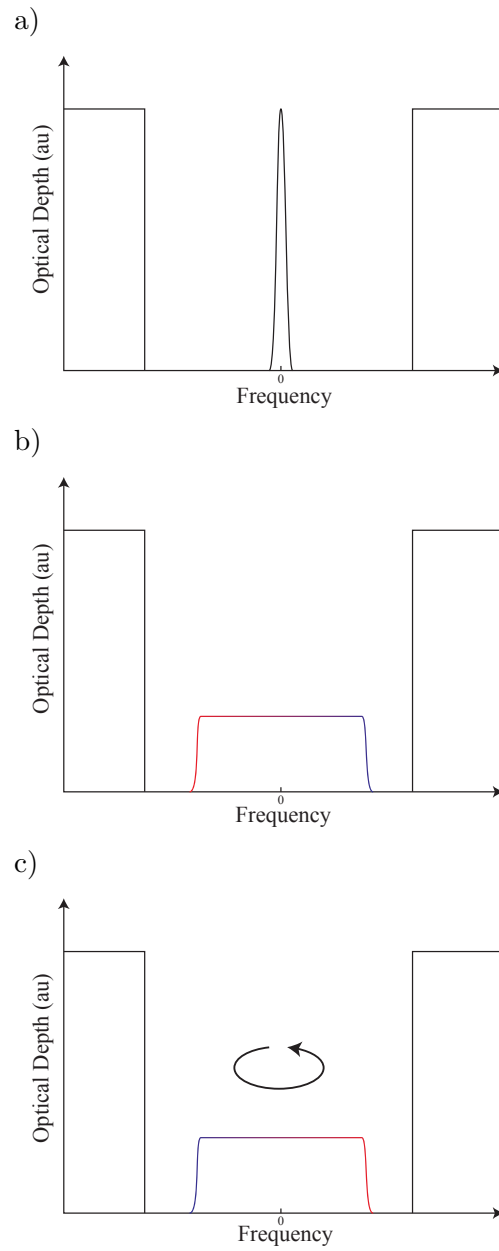


Figure 1.3 CRIB memory protocol schematic. a) An inhomogeneously broadened state is selectively pumped, and an anti-hole is left in the absorption profile. b) The signal field is resonantly absorbed by the artificially broadened anti-hole. c) At time τ , the artificial broadening is reversed, leading to photo-emission when the atoms rephase at time 2τ .

photon within the artificially broadened state $|e\rangle$ [Eq. (1.6)], during which each atom accumulates phase at a different rate δ_i . By cycling the excitation through an auxiliary state $|s\rangle$ with π pulses, followed by the reversal of the external E or B field at time τ , the sign of the atomic shifts goes from $\delta_i \rightarrow -\delta_i$, allowing the atoms to rephase after a further time τ . This leads to a collective enhancement of photon emissions from the atoms^[17], producing a time-reversed copy of the signal pulse in a well defined spatial mode in the reverse direction^[30,63]. The first experimental verification of CRIB was achieved in 2006 by Alexander *et al.*^[63] using cryogenically cooled europium (Eu) doped Y_2SiO_5 as the storage medium, storing 1 μs pulses for $\sim 10 \mu\text{s}$ with $< 1\%$ efficiency.

In early versions of the protocol, CRIB relied on the differential response of each atom to the external field to attain the artificial broadening, and without the π pulses — which introduce noise to the system — the signal is emitted in the forward direction, with an optimal efficiency of 54%^[64] due to re-absorption of the emitted pulse by the ensemble. Hétet *et al.*^[65] then proposed and demonstrated, in 2008, a modification of the protocol which allows unit retrieval efficiency in the forward direction, requiring no control pulses and using only 2 level absorbers. Key to the modified protocol, Gradient Echo Memory (GEM) is that instead of relying on differential atomic responses to an external field, a linear field gradient is applied along the longitudinal direction such that the frequency shifts of the excited level scale linearly with atomic positions along the axis of propagation. Each frequency component of the signal is absorbed by a different slice of atoms along the ensemble, so

the forward emitted signal is subsequently transmitted without resonant absorption. Using cryogenic Pr doped Y_2SiO_5 , Hétet *et al.* stored a $\sim 2 \mu\text{s}$ signal for $\sim 4 \mu\text{s}$ with a combined efficiency of 15% — something of an improvement upon the original CRIB experiment.

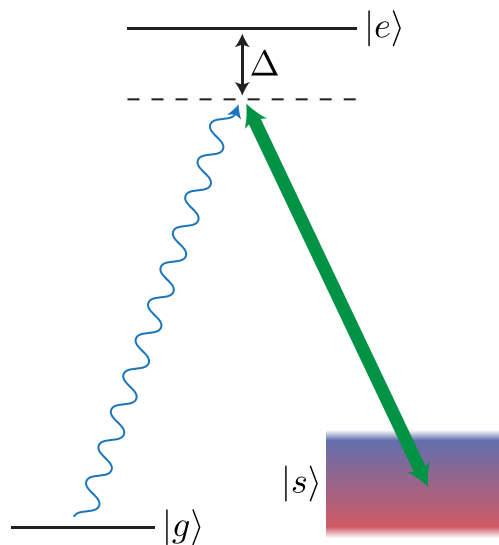


Figure 1.4 Schematic of Hétet *et al.*'s version of the GEM memory protocol^[66]. The storage state $|s\rangle$ is broadened by an applied field, and the signal field is directly absorbed via a Raman transition.

Once absorbed into the broadened $|e\rangle$, the excitation can in principle be transferred to an auxiliary state $|s\rangle$ to extend the storage time, but in demonstrating GEM in an atomic gas Rb (which has a Λ energy structure) for the first time, Hétet *et al.*^[66] introduced another modification — in the presence of a strong control beam (Fig. 1.4), signal photon absorption is accompanied by coherent transfer of population, via off-resonance Raman coupling, from $|g\rangle$ directly to a broadened $|s\rangle$. In effect, the two hyperfine ground states $|g\rangle, |s\rangle$ act as a two level system through the

Raman interaction. Signal pulses of $1 \mu\text{s}$ duration were stored and the retrieved echo was observed to decay with a time constant of $\sim 1.5 \mu\text{s}$ — consistent with dephasing time associated with atomic diffusion out of the interaction region.

One barrier against single photon operation with CRIB/GEM in a two-level system is the fluorescence noise that results from excited state decay following the optical pumping initialisation. For example, in erbium (Er) doped Y_2SiO_5 , the excited state has a lifetime of $\sim 11 \text{ ms}$ ^[67], thus rather problematic for observation of CRIB interactions which typically evolve on μs timescales. Lauritzen *et al.* navigated around this obstacle by stimulating decay into an auxiliary short-lived state, thereby depleting the excited state population^[68]. They observed the storage and retrieval of single photon level 200 ns pulses (stored for $< 500 \text{ ns}$ at 2.6 K) at telecoms wavelength ($1.5 \mu\text{m}$) with 0.25% combined efficiency.

Compared to EIT, this class of photon echo techniques hold the advantage that no *a priori* knowledge of the signal pulse shape is needed. This is contrary to EIT and the far-detuned Raman absorption memory (discussed in section 1.3.4), which require control pump profiles to be tailored to the signal field profiles for optimal storage/retrieval^[47,69,70]. As a comparison, Novikova *et al.*^[71] saw an increase from $< 5\%$ to 45% in EIT efficiency following pulse shape optimisation, while Hedges *et al.*^[72], Hosseini *et al.*^[73] measured 69%, 87% respectively through careful choice of material and an improved optical pumping configuration.

Requiring only two level absorbers and no optimised control fields, CRIB/GEM is also arguably more flexible as a protocol, both in terms of the choice of medium

as well as optical alignment. However, a major weakness of the protocol lies in its need for a narrow absorption peak, which calls for extensive optical pumping, effectively discarding a majority of the atoms from the storage/retrieval process and thereby decreasing the overall efficiency. Aside from the more complicated pumping configurations used in Hedges *et al.* and Hosseini *et al.*'s demonstrations, typical efficiencies are $< 1\%$. In addition, the stored signal bandwidth is limited by the induced broadening, which must be smaller than the hyperfine splitting within the involved states, and the full width at half maximum (FWHM) value of the anti-peak feature, which sets an upper bound on the memory lifetime, cannot be narrower than the homogenous linewidth of the atom. In practice, $1 \mu\text{s}$ pulses are stored for $\sim 3 \mu\text{s}$ in typical implementations, and the time bandwidth product — given by ratio of storage lifetime to the pulse duration — is only $\sim 3 - 4$. This is equivalent to saying that the memory is only capable of storing quantum coherence for 3-4 computation cycles.

In light of the complexities of the experimental setups in CRIB and GEM protocols, the original photon echo approach, which utilises the full bandwidth of the excited state, has recently gained renewed attention. I conclude this section with a brief summary of two of these protocols, which are both backed up by proof of principle demonstrations (reported in 2011^[74,75]). Like the traditional photon echo approach, a signal is first absorbed by a two level atomic ensemble (Fig. 1.5a) and a rephasing pulse inverts the ensemble population (Fig. 1.5b), but the atomic ensemble is then left to evolve beyond its rephasing point, during which echo emission is

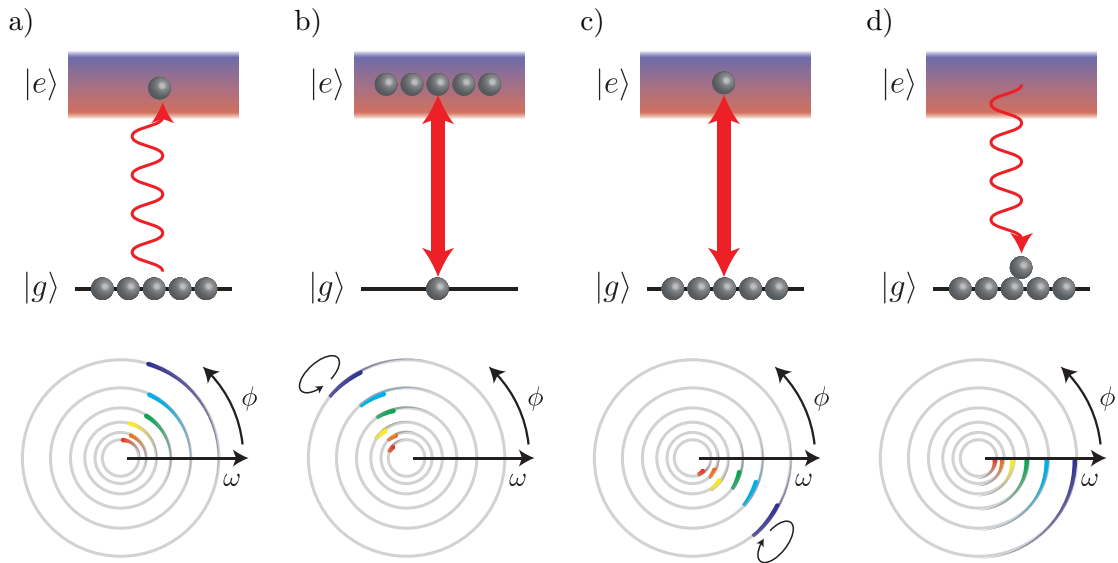


Figure 1.5 Both the HYPER and ROSE protocols can be implemented on a two-level ensemble. The top halves of each panel depict the sequence of signal absorption/emission [curly arrow in a), d)], rephasing pulses [bold arrows in b), c)] and ensemble populations. The lower halves represent the temporal evolution of phase ϕ for each frequency component (ω) within the medium. The x -axis represents the ‘rephasing point’ of the ensemble.

suppressed by experimental design. After this, a second rephasing pulse is applied (Fig. 1.5c), and the emission of the echo is allowed to take place as the ensemble evolves back towards the rephasing point. As the emission occurs after the second rephasing pulse (Fig. 1.5d), the atomic ensemble is close to the ground state during pulse retrieval, and amplified spontaneous noise is curbed, in principle allowing single photon level operation.

To suppress echo emission, McAuslan *et al.*^[75] applied an electric field gradient across the ensemble to prevent rephasing via the Stark shift effect in the Hybrid Photon-Echo Rephasing (HYPER) protocol, and Damon *et al.*^[74] relied on phase

mismatch between the emitted echo and the rephasing pulse in a physically thick ensemble in the Revival of Silenced Echo (ROSE) protocol. The HYPER experiment demonstrated the storage of a $1.8 \mu\text{s}$ long weak pulse for $120 \mu\text{s}$ with 2% storage and retrieval efficiency using a helium cooled Pr doped Y_2SiO_5 , while the ROSE experiment stored a $3 \mu\text{s}$ weak pulse for $82 \mu\text{s}$ pulse in helium cooled Er doped YSO crystal, with a storage and retrieval efficiency of 12%.

1.3.3 AFC

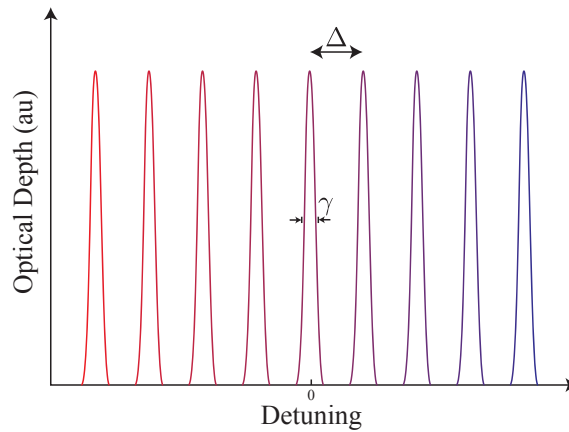


Figure 1.6 In AFC, an inhomogeneously broadened line is optically pumped to leave a regular series of absorption peaks, each of width γ and separated by Δ , in the storage ensemble. The pre-programmed storage time is determined by Δ , though it can be extended by transferring the stored excitation to a storage state (Fig. 1.1c).

Atomic Frequency Comb (AFC) is also a photon echo technique that is closely related to CRIB. Whereas the efficiency of CRIB is inherently limited by the need to discard many atoms during the initialisation step, AFC aims to use the inherent inhomogeneous broadening to its advantage. Instead of initialising with one anti-hole

peak in the absorption profile, the scheme, as proposed by Afzelius *et al.*^[76] in 2008, calls for a regular series of N peaks, each of width γ and separated by Δ in frequency, i.e. a frequency comb (Fig. 1.6). Even though the absorption profile consists of discrete peaks, an incoming signal pulse of bandwidth Γ is entirely absorbed when $N\Delta \gg \Gamma \gg \Delta$. This can be understood by appreciating that the uncertainty in frequency associated with a pulse is roughly its bandwidth, thus perfect absorption is possible providing that there is sufficient density of atoms within the peaks. The ensemble excitation is also of form Eq. (1.6), but here the frequency shifts δ_i are discrete rather than continuous (as in CRIB), due to the frequency comb. Key to AFC is that once stored, the atoms would rephase naturally at $t = 2\pi/\Delta$, leading to collective emission into a well defined spatial mode. Optimal efficiency for a forward emitted signal is also 54% due to reabsorption, and can approach unity for backward emission, like CRIB, with the use of π pulses to cycle through a storage state.

The first AFC experiment by de Riedmatten *et al.* in 2008^[77] was also the first demonstration of a solid light-matter interface at the single photon level. With Neodymium (Nd) doped in YVO_4 , they stored two 20 ns pulses and demonstrated coherence was preserved by interference measurements. The measured combined storage and retrieval efficiency was $< 0.5\%$. A study of the Maxwell-Bloch equations by Bonarota *et al.* in 2010 concluded that the efficiency is sensitive to the shape of the absorption peaks^[78]. In particular, using square rather than sine shaped peaks they demonstrated an increase of total efficiency from 10 to 17%, storing 450 ns pulses for 1.5 μs in cryogenic Thulium (Tm) doped YAG. A similar experiment by

Amari *et al.* increased storage efficiency to 35% in Pr doped Y_2SiO_5 [79].

Without transferring the excitation to a storage state, an AFC memory has a predetermined storage time, essentially acting like a delay line. Afzelius *et al.* thus proceeded to demonstrate the storage state transfer and stored 450 ns pulses for a user-programmable period of $\sim 20 \mu\text{s}$ in cryogenic Pr doped Y_2SiO_5 [80]. In general, to initialise an AFC ensemble, an auxiliary shelving state $|\text{aux}\rangle$ and nontrivial optical pumping techniques are required. This means a 4-level system ($\Lambda+|\text{aux}\rangle$) is needed to implement the full AFC protocol, thus restricting the choice of storage medium — cryogenic solid crystals remain the predominant material in experimental demonstrations so far. Similar to CRIB, the maximum storage bandwidth of AFC is bounded by the splitting between $|g\rangle$ and $|s\rangle$. With the exception of a recent experiment where Saglamyurek *et al.* [81] stored 200 ps pulses, typical stored pulse durations are $\sim 1 \mu\text{s}$ and a time bandwidth product of only ~ 3 .

1.3.4 Raman absorption

Raman absorption is possibly the most conceptually straight forward memory protocol. The Raman interaction is, in essence, the inelastic scattering of an incident photon, where the photon exchanges energy with the scattered medium (Fig. 1.7). First documented by Raman and Krishnan in 1928 [82], Raman scattering has been studied extensively [83–85] and has found applications in a range of spectroscopic [86–88] and lasing [89–91] techniques. Its use as a quantum memory was first proposed by Kozhokin *et al.* in 2000 [31].

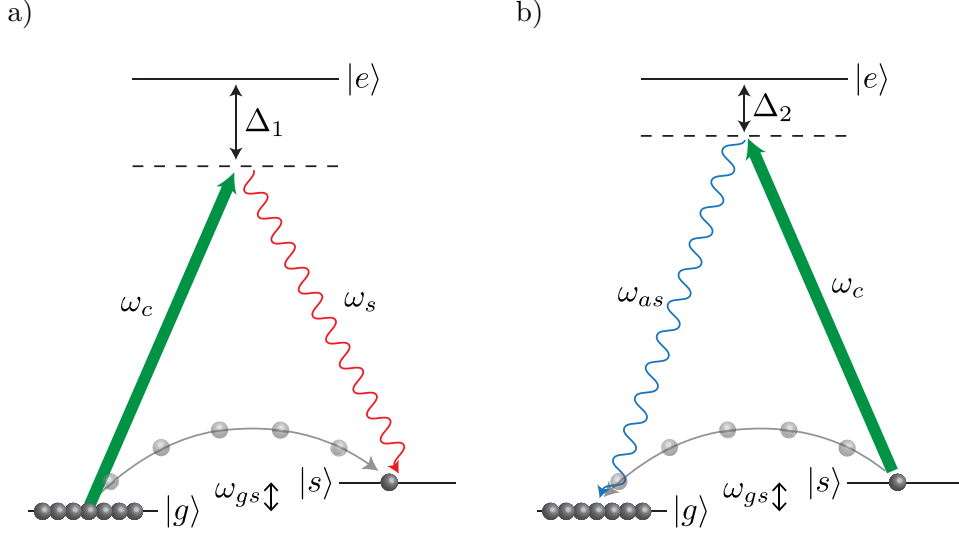


Figure 1.7 Different types of Raman scattering in atomic ensemble with ground state splitting ω_{gs} : a) In Stokes scattering, an incident photon of frequency ω_c , detuned from the $|g\rangle \rightarrow |e\rangle$ transition by Δ_1 , scatters from the medium, and leaves with a reduced frequency ω_s ($\omega_s = \omega_c - \omega_{gs}$). The energy imparted into the ensemble promotes one of the atoms into the storage state Eq. (1.1). b) When $|s\rangle$ is populated, a photon of frequency ω_c , detuned from $|s\rangle \rightarrow |e\rangle$ by Δ_2 , can undergo anti-stokes scattering, absorbing energy from the medium and leaves with increased frequency ω_{as} ($\omega_{as} = \omega_c + \omega_{gs}$).

In a Λ system with two ground states $|g\rangle, |s\rangle$ connected to an optical excitation $|e\rangle$ (Fig. 1.1d), a strong control field, with frequency ω_c , and a weak signal photon, with frequency ω_s , are incident on the storage medium. The two fields are in two-photon resonance with the two ground states — i.e. the frequency difference $\omega_s - \omega_c$ is equal to the ground state splitting ω_{gs} — and both are far detuned from the optical transition by Δ . The setup is almost identical to EIT, but the dynamics are different due to the large detuning Δ .

To illustrate, we start once again from the interaction Hamiltonian \hat{H}_I in Eq. (1.3),

and also representing the general state $|\psi\rangle = \Psi_g|g\rangle + \Psi_s|s\rangle + \Psi_e|e\rangle$ with the vector (Ψ_g, Ψ_s, Ψ_e) , we obtain the following expression for the time dependent solution $\Psi_e(t)$ using the relation $|\psi(t)\rangle = e^{i\hat{H}_I t}|\psi(0)\rangle$ (setting $\hbar = 1$ for convenience):

$$\Psi_e(t) = \frac{e^{-i\frac{\Delta t}{2}}}{\Xi} \left[i(\Omega_p \Psi_{g0} + \Omega_c \Psi_{s0}) \sin \frac{\Xi t}{2} + \Psi_{e0} \left(i\Delta \sin \frac{\Xi t}{2} + \Xi \cos \frac{\Xi t}{2} \right) \right], \quad (1.7)$$

where $\Xi = \sqrt{\Delta^2 + |\Omega_c|^2 + |\Omega_p|^2}$ and $\Psi_{g0,s0,e0} = \Psi_{g,s,e}(t=0)$. In the far detuned regime, $\Delta \gg \{|\Omega_c|, |\Omega_p|\}$ and the excited state population is approximately

$$|\Psi_e(t)|^2 \approx \left(\frac{|\Psi_{e0}| \Delta}{\Xi} \right)^2 + \text{Small oscillatory terms.} \quad (1.8)$$

Equation (1.8) shows that: a) in the absence of decay, the excited population is broadly a constant — the oscillatory terms scale as Δ^{-2} — and b) there is negligible transfer of population from the ground states $|g\rangle, |s\rangle$ to $|e\rangle$.

It follows that we can take $\dot{\Psi}_e = 0$, and using $\hat{H}_I|\psi\rangle = i\frac{d|\psi\rangle}{dt}$, the state $|e\rangle$ can be eliminated from the system of equations, and we end up with an effective Raman Hamiltonian \hat{H}_{Raman} that directly couples the two ground states:

$$\hat{H}_{\text{Raman}} = \frac{1}{2\Delta} \begin{pmatrix} |\Omega_p|^2 & \Omega_p \Omega_c^* \\ \Omega_c \Omega_p^* & |\Omega_c|^2 \end{pmatrix}. \quad (1.9)$$

Figure 1.8 compares state population evolution under the full three level Hamiltonian \hat{H}_I [Eq. (1.3)] and the approximate two level version \hat{H}_{Raman} [Eq. (1.9)]. As expected from the above analysis, starting with zero population, $|e\rangle$ remains almost

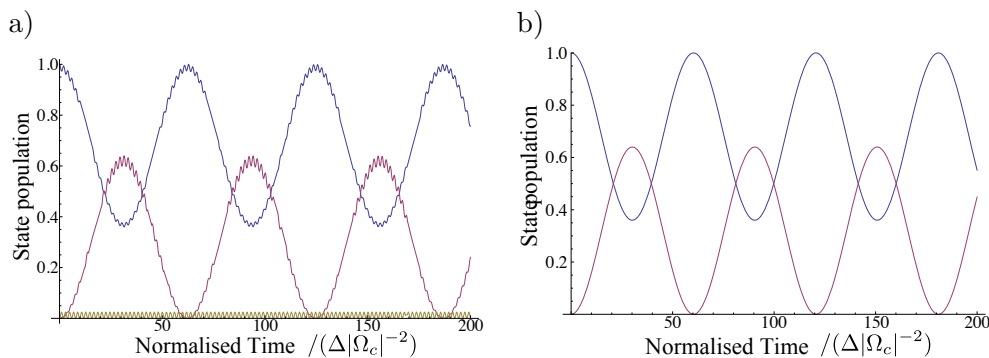


Figure 1.8 Comparison of state population evolutions in time for a) the full Hamiltonian \hat{H}_I and b) the approximate two level version \hat{H}_{Raman} . Populations in the $|g\rangle, |s\rangle, |e\rangle$ states are drawn in blue, red, yellow lines respectively in both graphs. All populations are in $|g\rangle$ initially, $|\Omega_c| = 2|\Omega_p|$ and $\Delta = 3|\Omega_c|$.

empty throughout (yellow line in Fig. 1.8a) and the two level model (Fig. 1.8b) captures the slowly varying envelope of the population transfer between $|g\rangle$ and $|s\rangle$ faithfully.

To summarise, the presence of a far detuned control field turns the Λ system effectively into a two level system where $|s\rangle$ becomes a state that is energetically $\omega_{gs} + \omega_c$ above $|g\rangle$. A signal photon that is resonant with this virtual two level structure can therefore be absorbed, simultaneously creating a unit of excitation in the storage ensemble state $|s\rangle$. To retrieve the signal photon, a second control pulse is applied on the medium after a user-determined interval, and the energy in the medium excitation is coherently transferred into an anti-Stokes photon as shown Fig. 1.7b.

Theoretical analyses of the Raman memory protocol in the literature take into account propagation effects by combining Maxwell's wave equation with the Hamil-

tonian calculations outlined above^[31,45,70]. The off-diagonal elements of the density matrix associated with the optical transition $|g\rangle\langle e|$ act as a source term, the atomic polarisation $P(z, t)$, for the wave equation (z is the longitudinal coordinate, parallel to wave propagation, and t is the time). Further, treating the signal as a quantum field (the control field remains classical) and taking into account dephasing $\gamma_{ge,gs}$ from the $|e\rangle \rightarrow |g\rangle, |s\rangle \rightarrow |g\rangle$ transitions respectively, the resulting set of equations, known as the Maxwell-Bloch equations, govern the system evolution:

$$c \left(\partial_z + \frac{1}{c} \partial_t \right) A(z, t) = \kappa P(z, t) \quad (1.10)$$

$$\begin{aligned} \partial_t P(z, t) &= -(\gamma_{ge} + i\Delta)P(z, t) + i\kappa^* A(z, t) \\ &\quad + \Omega_c(z, t)B(z, t) \end{aligned} \quad (1.11)$$

$$\partial_t B(z, t) = -\gamma_{sg}B(z, t) - \Omega_c^*(z, t)P(z, t). \quad (1.12)$$

Here, the complex conjugate quantities are denoted by $*$; $A(z, t) = \sum_{\mathbf{k}} \hat{a}_{\mathbf{k}} \exp\{i[\omega_s(t - z/c) + \mathbf{k}z]\}$ is a linear combination of single photon annihilation operator $\hat{a}_{\mathbf{k}}$ with wave vectors \mathbf{k} ($k = |\mathbf{k}|$); κ is the coupling associated with a single signal photon to the optical transition; $B(z, t)$ is the position dependent version of the spin wave Eq. (1.1) — where the spatial positions of the atoms relative to the ensemble determine the phase of superposition; and coupling $\Omega_c(z, t)$ due to the control pulse has a smoothly varying spatial and temporal profile. A 1D approximation is used in Eqs. (1.10) to (1.12), which is valid providing the Fresnel number associated with the optical setup is < 1 ^[92].

Given a sufficiently large detuning, population of the intermediate state $|e\rangle$ remains constant (see Fig. 1.8) and the optical polarisation also remains unchanged over the time scale of the Raman absorption. Thus $\partial_t P \approx 0$ and Eqs. (1.10) to (1.12) reduce to coupling between the optical and storage modes only

$$\left(\partial_z - i\frac{|\kappa|^2}{\Pi}\right)A(z, \tau) = \frac{\kappa\Omega(\tau)}{\Pi}B(z, \tau) \quad (1.13)$$

$$\left(\partial_\tau - i\frac{|\Omega(\tau)|^2}{\Pi}\right)B(z, \tau) = -\left(\frac{\kappa\Omega(\tau)}{\Pi}\right)^*A(z, \tau), \quad (1.14)$$

where we have transformed to a co-moving time coordinate $\tau = t - z/c$; $\Pi = \Delta - i\gamma_{ge}$ is the complex detuning of the polarisation; and $\gamma_{gs} \approx 0$, since decay from the storage state is negligible during Raman interaction — in a warm gas experiment led by K. Reim^[32], my fellow graduate student in the Oxford quantum memory group, atomic motion causes dephasing of storage excitation on a time scale of μs , significantly longer than the interaction time of 300 ps.

In a theoretical investigation of the Raman interaction in an ensemble memory, J. Nunn (also from the Oxford quantum memory group) found a linear map between signal photon field $A(z, \tau)$ and medium excitation $B(z, \tau)$ from Eqs. (1.13) and (1.14), characterised by a coupling parameter $C = |\kappa| \sqrt{L\Omega_{c,T}} / |\Pi|$ for an ensemble of length L and integrated Rabi frequency $\Omega_{c,T} = \int_{-\infty}^{\infty} |\Omega_c(\tau)|^2 d\tau$. Analysing the linear map with singular value decomposition (SVD) techniques, Nunn *et al.*^[70] have shown that it is convenient to decompose the spatial profile of $B(z, \tau)$ into a set of orthonormal modes $\{\phi_{B,i}(Cz/L)\}$, one of which ($\phi_{B,1}$) is preferentially

selected by the Raman interaction (i.e. easiest for an incident photon field to map into). Incidentally, although it is experimentally challenging to implement, optimal coupling into this $\phi_{B,1}$ mode can be achieved by tailoring the control pulse profile to that of the signal^[45,70,71]. Further, the readout process is the reverse of the readin, and the equivalent set of orthonormal modes for readout $\{\phi'_{B,i}(Cz/L)\}$ is spatially symmetric with respect to the readin modes, i.e. $\phi'_{B,i}(Cz) = \phi_{B,i}[C(1-z/L)]$. Thus, the readin and readout control pulses should propagate in opposite directions for optimal storage and retrieval of the signal field.

On the other hand, the experiments described in this thesis are carried out within a power regime that obviates the need for this potentially challenging reverse readout configuration. By keeping the Raman interactions within the spontaneous limit (the average number of Raman scattered Stokes/anti-Stokes per pump pulse is $\ll 1$) using sufficiently weak control pulses, the coupling parameter C can remain low. Given that the set of orthonormal modes $\phi_{B,i}$ are functions of the scaled spatial coordinate Cz/L , $B(z, \tau)$ tends towards a flat function within the length of the ensemble. Physically, this is consistent with the lack of stimulated emission/absorption effects during the scattering process, and all of the atoms interact with the incident photon field in the same manner. In this case, propagation effects can be ignored, and, for instance, spontaneous Stokes scattering (Fig. 1.7a) in an ensemble can be described without the Maxwell wave equation — simply by the Hamiltonian

$$\hat{H}_{I,\text{spont}} = g\hat{A}^\dagger\hat{B}^\dagger + g^*\hat{A}\hat{B}, \quad (1.15)$$

where g is the effective Raman coupling; \hat{A}, \hat{B} are the annihilation operators for the Stokes photon mode and collective storage excitation respectively. Experimentally, since $B(z, t)$ created from spontaneous scattering is spatially flat, it is spatially symmetric and readout efficiency is broadly independent of the readout direction (forwards/backwards).

The far detuned nature of the Raman interaction means that this protocol is the most robust, out of all the aforementioned protocols, against inhomogeneous broadening of the excited state. As such, it is also most uniquely suited to implementations in warm atomic gas and other easily accessible macroscopic systems without the need for complicated cryogenic setups or technically demanding optical pumping requirements. In 2010, Reim *et al.*^[32] first demonstrated the Raman memory with warm Cs gas by storing 300 ps pulses for 12.5 ns with a total efficiency of 15%. The bandwidth of the stored photon is ultimately only limited by the ground state splitting ω_{gs} , which is 9.2 GHz for Cs, and the time-bandwidth product, in this case, is ~ 1000 — at least an order of magnitude larger than any other room temperature quantum memory demonstrations. Subsequent experiments have seen extensions of Raman memory operations into the single photon regime (as well as storage time of μs)^[93] as well as storage and retrieval of a polarisation qubit^[94].

1.4 A practical entanglement distribution device

Finally, I would like to review some of the experimental realisations towards distributed entanglement generation. I have already mentioned entangled states as

being a useful resource for quantum computation. Complementary measurements on different parts of an entangled state yield correlated results which are inconsistent with classical explanations (as shown by Bell in 1964^[95]). This quantum correlation in turn enables scalable quantum computation to achieve exponential speed up over the best known classical algorithms. Significant efforts have been devoted to creating and observing entanglement in a variety of systems over the last decade, each of which has particular advantages.

For instance, tripartite entangled GHZ and W states have been created with multiple trapped ions^[96], other entangled states have been created between ions and photons^[97,98], as well as between different superconducting qubits^[99]. In these experiments, the individual ions/Josephson junctions act as single atom quantum memories, capable, in principle, of storing coherence for seconds. However, the resource overheads required for these systems are likely to prevent their use as any robust, room temperature devices. In the following sections, I will highlight two strands of research which hold relevance to this thesis, citing examples which are more likely to be the basis of the quantum versions of a PC than the Colossus¹.

1.4.1 Nitrogen-vacancy (NV) centres

On the other end of the spectrum, NV^- centres in diamond provide a promising route towards a solid-state room temperature device. In diamond, a carbon atom within the lattice can sometimes be displaced by a nitrogen atom, which has one

¹Colossus was the room-sized Enigma code-breaking vacuum tube computer used at Bletchley Park during World War II.

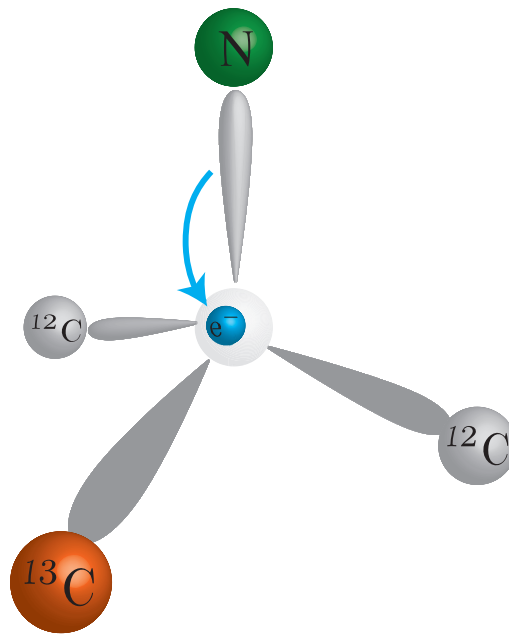


Figure 1.9 Structure of NV^- centre. A substitutional nitrogen atom donates an electron to a neighbouring vacant site to form the well known point defect in diamond. If there is also a ^{13}C atom next to the vacancy, hyperfine structures would appear in the electronic energy levels.

extra valency electron compared to carbon. If there happens to be a vacant lattice site adjacent to the nitrogen atom, the extra valence electron will be confined within this effective cavity in the lattice structure, so that discrete electronic energy levels form (Fig. 1.9). Moreover, about 11% of the electronic wave function overlaps with the neighbouring atoms^[100], and hyperfine splitting of the electron levels develops if there are nonzero nuclear spins within the overlap regions — 1.1% of naturally occurring carbon atoms exist as ^{13}C isotopes, with a nuclear spin of 1/2. Using a mixture of optical and resonant microwave pulses, Dutt *et al.*^[101] demonstrated coherent transfer of qubit states between an NV centre electron and nuclear spin at

room temperature. They also measured the coherence lifetime of the nuclear spin to be ~ 0.5 ms, which compares well against the μs lifetimes of typical warm atomic gases.

Easily susceptible to localised crystal strain, no two NV centres are truly alike. As well, coupled with the low single photon/particle interaction strength, creating entanglement with NV centres through optical manipulations is therefore a challenging task. Steady progress in recent years has seen, for example, a proof of principle experiment by Neumann *et al.*^[100], in which the nuclear spins of two ^{13}C nuclei sharing the same NV centre were entangled. Further, by etching out cavity structures directly in diamond, Faraon *et al.*^[102] enhanced the coupling strength to single photons by a factor of 10.

The techniques developed in these and other experiments have culminated in two recent parallel efforts in which two spatially separated NV centres were entangled. In 2013, Dolde *et al.*^[103] entangled the electron spins of two closely spaced NV centres at room temperature. Spatially separated by ~ 25 nm, the spins of the electron pairs are coupled to each other predominantly via the magnetic dipole interaction, creating 4 distinct energy eigenstates which are robust against environmental noise. Application of a suitable resonant optical pumping sequence then created the desired Bell state. On the other hand, Bernien *et al.*^[104] were able to use the Stark shift to tune the energy level of one NV centre against another at cryogenic temperature, thereby creating an indistinguishable NV pair. Subsequent projective measurements on the joint electron spin states created the resulting entanglement,

which is distributed over an impressive 3 m in distance.

1.4.2 Atomic ensembles

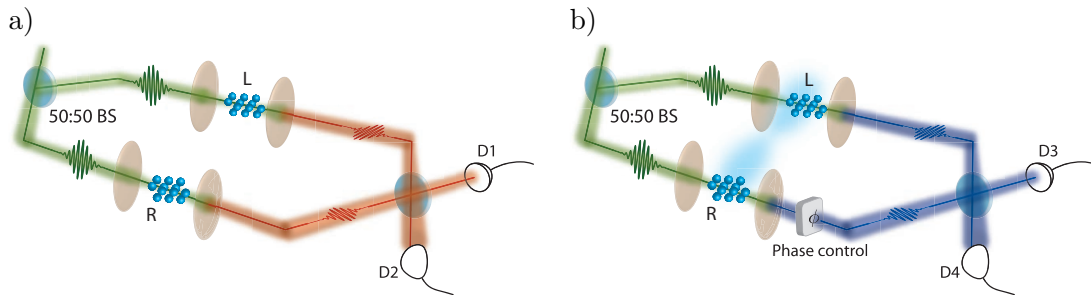


Figure 1.10 Entanglement generation with the DLCZ protocol by Raman scattering of pump light (green) and its verification: a) Single Stokes photon (red) detected at either detector D1, D2 projects ensembles L , R into a Bell State. b) Probability of anti-Stokes (blue) detection at D3, D4 can be controlled by varying the relative phase ϕ between the interferometer paths. 50:50 beamsplitters (BS) are used to produce identical pump pulses and combine the spatial paths of Raman scattered photons.

Due to its strong interaction with light, the atomic ensemble is a desirable testbed for quantum optics implementations, and with this in mind, in 2001, Duan, Lukin, Cirac and Zoller proposed the seminal DLCZ protocol^[16]. It was devised as a means to bypass the limited coupling associated with single particle quantum memories (such as the aforementioned trapped ions and NV systems), and to achieve entanglement distribution using only linear optics tools.

In the DLCZ scheme, two spatially separated atomic ensembles are first entangled via a joint measurement, and from there entanglement between more distant nodes can be achieved through entanglement swapping and purification. Figure 1.10a

shows the initial entanglement creation: a pump pulse is sent simultaneously into each of the two ground state ensembles L , R . The pulses are sufficiently weak that the average number of Stokes scattering event — the creation of a lower energy photon, accompanied by one spin wave excitation in the ensemble (Fig. 1.7a) — is much less than one. The beam paths of the Stokes fields are combined on a subsequent beamsplitter (BS) and detected on the single photon detectors D1, D2. When either of the detectors registers a click, there is no way, even in principle, of determining from this detection event which ensemble is now excited. Quantum mechanically, the two ensembles are now described by the generalised Bell state (the interaction will be discussed again in greater depth in chapter 4)

$$|\psi\rangle_{LR} = \frac{1}{\sqrt{2}} \left(|01\rangle + e^{i\theta} |10\rangle \right), \quad (1.16)$$

where $|ij\rangle_{LR}$ denote $i(j)$ quanta of excitations in the $L(R)$ ensemble, and θ is phase shift associated with the relative path difference in the interferometer.

Equation (1.16) is a maximally entangled state, and to verify its existence, a second pair of pump pulses is directed into the ensembles L , R . There is now a finite probability of an anti-Stokes scattering event happening (Fig. 1.7b), in which the joint medium excitation Eq. (1.16) is coherently mapped onto a higher energy anti-Stokes photon, i.e. the entanglement is transferred from the medium to the readout photon, which now exists in *both* arms of the interferometer. By adjusting the relative phase delay ϕ in Fig. 1.10b and combining the anti-Stokes photon beam

path with a BS, the probability of detecting the photon at detectors D3, D4 can be controlled. This is in contrast to the classical description, where a photon can only exist in the L or R arm, and it would be detected by D3, D4 50% of the time, irrespective of any adjustments of ϕ .

One major advantage of the DLCZ scheme is that the entanglement creation is heralded by the detection of a Stokes photon — once it is detected, the entanglement is stored in the ensemble until retrieved at a later, user-determined time. This setup was realised physically in 2004 by Matsukevich and Kuzmich^[105], who demonstrated quantum state transfer between the light field and two Rb atomic clouds held in MOTs. In 2005, Chou *et al.*^[106] created and verified entanglement in spatially separated (3 m apart) cryogenic Cs ensembles as outlined above. As an asides, to contrast with these DLCZ experiments, in 2007, Moehring *et al.*^[107] were able to entangle two individual Ytterbium (Yb) ions placed 1 m apart by interfering the indistinguishable photons scattered from the atoms.

Following a slightly different approach towards distributed entanglement generation, in 2011, three groups, Zhang *et al.*^[108], Saglamyurek *et al.*^[81] and Clausen *et al.*^[109] entangled an atomic ensemble memory with a photon. In their experiments, they generated a pair of entangled photons by down conversion, stored one of them in a memory (EIT using Rb atoms in a MOT in Zhang's case, and AFC using RE doped solids for the other two) before retrieval and verified that the entanglement survived the storage and retrieval process. At around the same time as the publication of the results in chapter 4 of this thesis, Usamani *et al.*^[110] have extended this

to include storage and retrieval of both constituents of the entangled photons from spatially separated solids.

It is worth noting that, with the exception of NV centres, all of these entanglement demonstrations require cryogenic conditions to operate. Also, in the case of the AFC entanglement experiments, the ensembles are acting more as delay lines than as true memories (though it has already been demonstrated, separately, that AFC is capable of on-demand retrieval^[80]). As yet, there is not a definitive demonstration of a physical system which can be used in a scalable quantum computation device that can operate in room temperature environment, and requiring only a modest amount of overhead.

Chapter 2

Stokes Scattering in bulk diamond

2.1 Optical phonons as a storage excitation

Atomic gases are isotropic, and consequently light-matter scattering interactions are not dependent on the orientation of the atomic ensemble with respect to the incident light. This contrasts with scattering in crystals, which have regular spatial features, and the orientations of the atomic arrays with respect to the incident light determine the range of allowed interactions as well as the nature of the excitation created within the crystal. The crystal structure of diamond is formed by a convolution of the face-centred cubic space lattice with the basis consisting of carbon atoms at $(0,0,0)$, and $(\frac{1}{4}, \frac{1}{4}, \frac{1}{4})$ relative to each lattice point and each carbon has 4 nearest neighbours^[111] in a tetrahedral configuration as shown in Fig. 2.1. The resulting

structure has octagonal symmetry, i.e. is invariant under a set of reflections, rotations and inversions that form the point group $m\bar{3}m$ (O_h) as well as the space group $Fd\bar{3}m$ (O_h^7), which consists of the point group, plus a set of translational operations which leave the crystal invariant^[112].

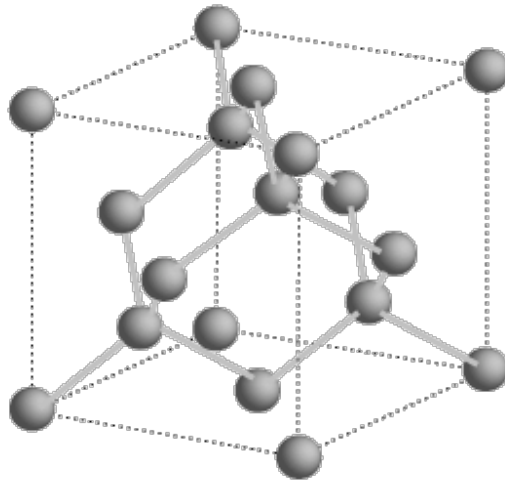


Figure 2.1 The diamond lattice comprises a stack

Being a regular array of carbon atoms, there exist multiple normal modes of collective vibrational excitations, known as *phonons*, in diamond where all of the atoms vibrate at the same frequency. In general, there are two different branches of vibrations: i) *acoustic* phonons — where adjacent lattice sites vibrate in phase with each other; ii) *optical* phonons — where adjacent lattice sites vibrate out of phase to each other. By definition, acoustic phonons are travelling waves, carrying no energy as the phonon momentum approaches zero, whereas optical phonons can exist as an energetic standing wave vibration with zero phonon momentum. Energy and momentum conservation ensures that only the optical modes in a typical solid are

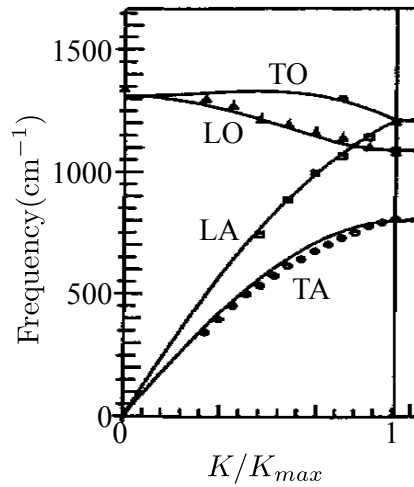


Figure 2.2 Phonon dispersion relations for diamond. The solid lines are obtained from *ab initio* calculations and inelastic neutron scattering data is plotted as dots [graph is obtained from^[113]]. T(L)O(A) label the transverse (longitudinal) optical (acoustic) phonon branches. The wave vector K is parallel to the $[100]$ crystal axis and its magnitude is in units of the maximal allowable K_{max} (the ‘Brillouin zone edge’) due to the finite lattice spacing.

coupled to the photon modes (whose range of momentum is typically much smaller than that of the phonon) during a light scattering interaction in crystals (hence the name)^[111].

Figure 2.2 shows the dispersion relations of the different phonon branches in diamond. Note that the optical phonon modes (LO and TO) are much higher in energy compared to the acoustic modes at zone centre (i.e. $K = 0$), and the dispersion curve is much flatter compared to the acoustic modes (LA and TA). This brings about multiple advantages when considering optical phonon as a storage excitation for a room temperature quantum memory:

1. The energy of an optical phonon scales with the square root of the linear

coupling constant^[111,112], and the extraordinary stiffness of diamond translates to 40 THz (1,332 cm⁻¹ in spectroscopic units) in this case. Optical phonon occupation at room temperature is only $e^{-\frac{\hbar\omega}{k_B T}} \sim 0.17\%$, implying that the optical phonon mode is well isolated from thermal noise. Therefore, unlike all other systems (atomic gases, ions, NV centres etc.), ground state initialisation by optical pumping is not required.

2. The ground and storage state splitting ω_{gs} of a user programmable quantum memory determines the maximum allowable bandwidth of a stored photon. The $\omega_{ph} = 40$ THz splitting in diamond compares well against the typical GHz splittings for NV centres, atomic gas etc. A quantum memory with diamond phonons would therefore be well suited for operations at high repetition rates.
3. When storing a broadband excitation, a range of phonon frequencies $\Delta\omega_{ph}$ is excited, leading to dephasing of the storage state. Assuming a zone centre phonon is created using a 10 THz pulse ($\Delta K \sim 2 \times 10^5$ m⁻¹, typical ultrafast solid-state laser bandwidth), and applying Taylor's expansion to the optical phonon dispersion

$$\omega_{ph}(K) \approx \omega_{ph}(0) + WK^2, \quad (2.1)$$

with $W \sim 1.297 \times 10^{-6}$ m²/s for diamond^[114], we can estimate the dephasing time to be ~ 100 μ s. This is seven orders of magnitude greater than the population lifetime of the phonon (see chapter 3), and therefore pure dephasing effects can be ignored as long as the storage excitation exists.

4. One final advantage of using diamond phonon is that it is a bulk excitation. Its coupling to an external light field can be increased just by using a thicker piece of crystal, and the experiments in this thesis show that significant interaction with light can be achieved with sub-millimetre thick crystals (compared to the cm interaction lengths of typical atomic gas experiments) due to its high Raman scattering cross-section.

Section 2.3 (with the exception of the last subsection) in this chapter is an edited version of my published paper^[115], for which I have carried out the experimental measurements and data analysis. The theoretical discussions therein were developed in conjunction with J. Nunn and B.J. Sussman (amongst other inputs from my fellow co-authors on the paper).

2.2 Raman scattering selection rules in diamond

When light scatters from matter, certain transitions are allowed and others are forbidden due to symmetries in the physical system. For example, the off-diagonal element of a dipole operator $\hat{d} = e\hat{r}$ (where e is the electron charge, and \hat{r} is the quantum mechanical position operator) describing an electronic transition from state ψ_i to ψ_f is:

$$\langle \psi_f | \hat{d} | \psi_i \rangle = e \int_{\text{Vol}} \psi_f^*(\mathbf{r}) \mathbf{r} \psi_i(\mathbf{r}) d^3\mathbf{r}, \quad (2.2)$$

where the integral is over a three dimensional volume. The function \mathbf{r} in the integral has odd parity, i.e. $\mathbf{r} \rightarrow -\mathbf{r}$ changes sign on inversion of spatial coordinates, and for

the integral to be non-zero, the functions $\psi_f^*(\mathbf{r}), \psi_i(\mathbf{r})$ must likewise have different parities. In general, symmetry arguments reveal whether a transition is possible without knowledge of the precise form of the wavefunctions. Experimentally, the polarisation selection rule provides an extra means to filter the pump from the Raman scattered signal, or even, as in the later experiments in this thesis, to optically resolve two Raman signals whose temporal separation is too small for electronic gating.

2.2.1 Representation theory

$$\begin{array}{cc}
 \text{a)} & \text{b)} \\
 \begin{array}{cccc}
 1 & + & - & 2 \\
 3 & - & + & 4
 \end{array} & & \begin{array}{cccc}
 1 & + & - & 2 \\
 3 & + & - & 4
 \end{array} & \longleftrightarrow & \begin{array}{cccc}
 1 & + & + & 2 \\
 3 & - & - & 4
 \end{array}
 \end{array}$$

Figure 2.3 Basis of a) 1D and b) 2D irreducible representations of the D_4 group. The numbers $x = \{1, 2, 3, 4\}$ label the vertices of a square, and $+[-]$ represent the result of the function on x , $f(x) = +1$ [$f(x) = -1$].

In a crystal, the lattice configuration determines symmetry considerations, which are described mathematically by representation theory — the representation of group actions with linear algebra. Consider the function $f(x)$ defined by $f(1) = f(4) = 1, f(2) = f(3) = -1$, where x labels the four vertices of a square (Fig. 2.3a), and we label this function as state $|\phi_A\rangle$ [in this case represented by the vector $(1, -1, -1, 1)$ in the function basis $\{f(1), f(2), f(3), f(4)\}$]. The dihedral group D_4 contains the set of reflections and rotations which leave a square invariant. A 90° clockwise rotation about the centre is clearly an element, r , from this group, but applying the rotation

on the function space (Fig. 2.3a) would produce a new function $f(x) \xrightarrow{r} f'(x)$, with $f'(1) = f'(4) = -1, f'(2) = f'(3) = 1$, or, $|\phi_A\rangle \longrightarrow -|\phi_A\rangle$. Similarly, reflection about a vertical or horizontal axis also give $|\phi_A\rangle \longrightarrow -|\phi_A\rangle$, whereas 180° rotations and reflections along the diagonals gives $|\phi_A\rangle \longrightarrow |\phi_A\rangle$. For this particular ‘function state’ $|\phi_A\rangle$, we have found a 1D representation of the group D_4 , where each element is represented by a 1D ‘matrix’ of either 1 or -1, acting on $|\phi_A\rangle$.

There is also a 2D representation of D_4 : labelling the function on the LHS (RHS) of Fig. 2.3b by $|\phi_{B1}\rangle$ ($|\phi_{B2}\rangle$), 90° clockwise rotation is described by the orbit $|\phi_{B1}\rangle \xrightarrow{r} |\phi_{B2}\rangle \xrightarrow{r} -|\phi_{B1}\rangle \xrightarrow{r} -|\phi_{B2}\rangle \xrightarrow{r} |\phi_{B1}\rangle$, or, more succinctly, by the 2D matrix $\begin{pmatrix} 0 & -1 \\ 1 & 0 \end{pmatrix}$. Likewise, reflection along the axis running through vertices 2, 3 is represented by $\begin{pmatrix} 0 & -1 \\ -1 & 0 \end{pmatrix}$. Both of these representations are examples of *irreducible representations* of the group D_4 , i.e. within the space spanned by the basis states associated with each representation, there exists no subspace that is invariant under the action of all D_4 elements. The trace of all these matrices in the irreducible representations can be tabulated as a *character table*, which has remarkable mathematical properties that can be used to reveal hidden symmetries in a complicated system.

Table 2.1 is the character table of the octahedral O_h group. Each row (labelled by A_{1g}, A_{2g} etc.) is associated with a different irreducible representation (known as the *character* of the representation in the literature), and each column with a different *conjugacy class*. Here the irreducible representations are classified using

	E	8C ₃	6C ₂	6C ₄	3C ₂ =(C ₄) ²	I	6S ₄	8S ₆	3σ _h	6σ _d
A _{1g}	1	1	1	1	1	1	1	1	1	1
A _{2g}	1	1	-1	-1	1	1	-1	1	1	-1
E _g	2	-1	0	0	2	2	0	-1	2	0
T _{1g}	3	0	-1	1	-1	3	1	0	-1	-1
T _{2g}	3	0	1	-1	-1	3	-1	0	-1	1
A _{1u}	1	1	1	1	1	-1	-1	-1	-1	-1
A _{2u}	1	1	-1	-1	1	-1	1	-1	-1	1
E _u	2	-1	0	0	2	-2	0	1	-2	0
T _{1u}	3	0	-1	1	-1	-3	-1	0	1	1
T _{2u}	3	0	1	-1	-1	-3	1	0	1	-1

Table 2.1 Character table for the O_h group.^[116]

the Mulliken notation, details of which can be found in the standard group theory texts^[117,118]. The conjugacy class of each group element a is the set of operators given by $\{gag^{-1} : g \in O_h\}$, where g^{-1} is the inverse of g , and gag^{-1} must be a member of the same group by definition of a group^[119]. Further, each element in the group can belong to only one of these conjugacy classes, within which all elements share the same trace under each representation. The labels for the classes are written in the form $n_l S_l$, where n_l is the number of elements within the l th conjugacy class S_l [$S_l = \{E, C_3, i, S_4, \dots\}$].

It can be shown from Representation theory that the weighted inner product of the vectors formed by each character (i.e. each row of the character table) with itself is 1, and 0 between two different characters: If we label the characters in Table 2.1 by χ_{α_k, S_l} , where subindices α_k identifies the irreducible representation

($\alpha_k \equiv \{A_{1g}, A_{2g}, E_g, \dots\}$), and let $N = \sum_l n_l$, then^[119]

$$\frac{1}{N} \sum_l n_l \chi_{\alpha_k, S_l} \chi_{\alpha_{k'}, S_l}^* = \begin{cases} 0 & \text{if } k \neq k' \\ 1 & \text{if } k = k' \end{cases}, \quad (2.3)$$

where the * denotes a complex conjugate. Providing we can express an arbitrary interaction/system as a vector, we can represent the symmetry operations using the corresponding basis and calculate the traces of these operators. The traces from this representation form a character which we could then ‘decompose’ into the characters of the irreducible representations through the orthogonality relationship Eq. (2.3) to determine the symmetry properties of the interaction. For instance, the dipole operator is $\mathbf{d} = e\mathbf{r} \propto (x, y, z)$, and, in this basis, the identity operation, referred to as E in the literature (first column in Table 2.1) has trace 3; C_2 is a 180°

rotation, and one of the matrices in this conjugacy class is rotation around the z

axis, $\begin{pmatrix} -1 & 0 & 0 \\ 0 & -1 & 0 \\ 0 & 0 & 1 \end{pmatrix}$, which has trace -1; and as would be expected from the fact

that the dipole operator does not have inversion symmetry, the inversion matrix,

$I = \begin{pmatrix} -1 & 0 & 0 \\ 0 & -1 & 0 \\ 0 & 0 & -1 \end{pmatrix}$ has a negative trace -3. Extending this calculation through

all of the conjugacy classes S_l , we obtain the characters $\chi_{\mathbf{d}, S_l}$, which decomposes into χ_{T_{1u}, S_l} only — in other words, the dipole operator obeys the same symmetries represented by T_{1u} in Table 2.1.

From the dipole integral Eq. (2.2), we have shown that the dipole operator \hat{d} and the atomic transition $|\psi_f\rangle\langle\psi_i|$ must have the same inversion symmetry in an allowed transition. In representation theory this argument is extended to include all symmetric operations: for an allowed transition, the same irreducible representation must appear in the decompositions of the interaction Hamiltonian as well as the atomic transition^[112,120]. For example, a cubic lattice is invariant under 90° rotations, and therefore any allowed interactions must also be invariant under 90° rotations, since rotation of the lattice or the incident beam around the lattice are physically equivalent.

Having established that the symmetry of the dipole operator is equivalent to the T_{1u} representation, I now examine the symmetries of the transition from ground state $|\psi_i\rangle$ to a phonon excitation $|\psi_f\rangle$. The character of the transition χ_{ph,S_l} can be formed simply by^[112]

$$\chi_{\text{ph},S_l} = \chi_{\psi_i,S_l}^* \chi_{\psi_f,S_l}, \quad (2.4)$$

where χ_{ψ_i,S_l} (χ_{ψ_f,S_l}) is the character of the ground (excited) state. The character of a phonon can be obtained by analysing the atom displacements within the primitive cell (the smallest repeating unit in a lattice)^[112]. In the ground state, all atoms are stationary and therefore the ground state is invariant under all of the symmetry actions contained in the O_h group — χ_{ψ_i,S_l} is equivalent to the character of the ‘trivial’ representation χ_{A_{1g},S_l} . In this representation, $\chi_{\psi_i,S_l} = 1$ for all S_l ’s, so, $\chi_{\text{ph},S_l} = \chi_{\psi_f,S_l}$ by Eq. (2.4). Similar to the above analysis for the dipole operator, we can generate matrices for O_h group actions using $3n_{\text{prim}}$ basis vectors to represent

atomic displacements (3 spatial dimensions associated with each of n_{prim} atoms in the primitive cell). Calculating the traces of these matrices give the character of the phonon excitation

$$\chi_{\text{ph},S_l} = \chi_{T_{1u},S_l} + \chi_{T_{2g},S_l}. \quad (2.5)$$

The first term on the RHS is the acoustic phonon mode^[121,122], which is a dipole active mode, since it has the same irreducible representation (T_{1u}) as the dipole operator. This contrasts with the optical phonon mode, whose representation is equivalent to T_{2g} , and is therefore dipole forbidden. In the presence of two photon fields (e.g. in Raman scattering), however, the character of the interaction Hamiltonian is

$$\chi_{H_I,S_l} = \chi_{\mathbf{d},S_l}^* \chi_{\mathbf{d},S_l} \quad (2.6)$$

$$= \chi_{A_{1g},S_l} + \chi_{E_g,S_l} + \chi_{T_{1g},S_l} + \chi_{T_{2g},S_l}. \quad (2.7)$$

Equation (2.7) is obtained using the orthogonality condition Eq. (2.3). Since the irreducible representation T_{2g} appears in both Eqs. (2.5) & (2.7), we can conclude that the diamond optical phonon is Raman active. In fact, this is consistent with the ‘rule of mutual exclusion’, which states that vibrational modes must either be infrared or Raman active (but not both) in a centrosymmetric crystal (such as diamond)^[122,123].

2.2.2 Raman cross section

The Stokes scattering process is shown schematically in Fig. 1.7a: in diamond, the Λ structure is made up of $|g\rangle$ representing no phonons, an optical phonon as the $|s\rangle$ storage state (such that $\omega_{gs} = \omega_{\text{ph}}$), intermediated by the electronic conduction band $|e\rangle$. In the macroscopic theory of light scattering, the Raman scattering cross section (which expresses the strength of an interaction in terms of the scattered light intensity) for a non-polar crystal such as diamond can be written as a function of the Raman tensor $T_{ij,k}$, and polarisation vectors $\boldsymbol{\varepsilon}_p, \boldsymbol{\varepsilon}_s, \mathbf{Q}$ for the pump, Stokes and phonon fields respectively^[122]

$$\frac{dS}{d\Omega} \propto \left| \sum_{ijk} T_{ij,k} \varepsilon_{p,i} \varepsilon_{s,j} Q_k \right|^2, \quad (2.8)$$

where the LHS is the *differential cross section* — the change in beam energy, collected within an elemental solid angle $d\Omega$. The subindices i, j, k indicates the components of the vectors along the $\{x, y, z\}$ axes, which are defined to be parallel to the principle axes of the face-centred cubic diamond structure.

To determine the form of the Raman tensor $T_{ij,k}$, note that the optical phonon modes represented by \mathbf{Q} have an irreducible representation T_{2g} by the arguments in Section 2.2.1. For the optical phonon to be Raman active, the components of the photon fields $\boldsymbol{\varepsilon}_p, \boldsymbol{\varepsilon}_s$ must also combine such a way in Eq. (2.8) so as to contain the same irreducible representation. As well as listing the characters of each irreducible representation, character tables in the literature also list the basis functions that

generates the associated representation. In this case, the vector formed by the function $\{yz, xz, xy\}$ has characters χ_{T_{2g}, S_l} ^[116], and they are the only nonzero elements in the Raman tensor^[122]:

$$\hat{T}_x = \begin{pmatrix} 0 & 0 & 0 \\ 0 & 0 & a \\ 0 & a & 0 \end{pmatrix} \quad \hat{T}_y = \begin{pmatrix} 0 & 0 & a \\ 0 & 0 & 0 \\ a & 0 & 0 \end{pmatrix} \quad \hat{T}_z = \begin{pmatrix} 0 & a & 0 \\ a & 0 & 0 \\ 0 & 0 & 0 \end{pmatrix}. \quad (2.9)$$

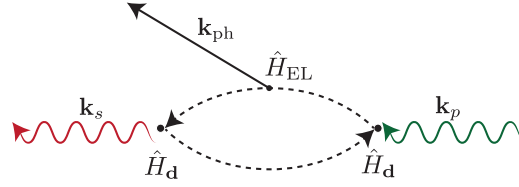


Figure 2.4 Diagrammatic representation of the Raman scattering process.

The Raman cross section $\frac{dS}{d\Omega}$ can also be written in terms of quantised operators from microscopic theory of Stokes scattering — a brief outline is given here as it illustrates the physical mechanism behind the inelastic scattering process. Figure 2.4 shows the dominant mechanism for optical phonon creation. First, an incoming pump photon with wave vector \mathbf{k}_p creates a virtual electron-hole pair in diamond via the interaction Hamiltonian^[112]

$$\hat{H}_d = \frac{e}{m} \sum_j \hat{A}(\mathbf{r}_j) \cdot \hat{p}_j \quad (2.10)$$

that couples the quantised vector potential of the pump field $\hat{A}(\mathbf{r}_j)$, with the mo-

momentum \hat{p}_j of the j th electron at position \mathbf{r}_j . Lattice vibration (phonon mode with wave vector \mathbf{k}_{ph}) is then induced by the electron-hole pair via the *deformation potential* $\Xi_{\sigma,\beta\alpha}$ contained within the Hamiltonian \hat{H}_{EL} (its full form can be found in the literature^[112])

$$\langle \beta, n_{\text{ph}} + 1 | \hat{H}_{\text{EL}} | \alpha, n_{\text{ph}} \rangle \propto \sum_{\sigma, \mathbf{k}_{\text{ph}}} \mathbf{Q} \cdot \boldsymbol{\xi}_{\sigma, \mathbf{k}_{\text{ph}}} \frac{\Xi_{\sigma, \beta\alpha}}{d}, \quad (2.11)$$

where $\boldsymbol{\xi}_{\sigma, \mathbf{k}_{\text{ph}}}$ is a unit vector pointing parallel to the relative displacement between adjacent atoms in the primitive cell, σ represents the phonon branch, d is the lattice constant, and the Left-Hand Side (LHS) describes a transition from an electron-hole pair state $|\alpha\rangle$ with n_{ph} phonons to electron-hole state $|\beta\rangle$ with $n_{\text{ph}} + 1$ phonons. Subsequent recombination of the electron-hole pair produces a Stokes photon (wave vector \mathbf{k}_s). Conservation of momentum ensures that

$$\mathbf{k}_p = \mathbf{k}_{\text{ph}} + \mathbf{k}_s, \quad (2.12)$$

and conservation of energy requires

$$\omega_p = \omega_{\text{ph}} + \omega_s, \quad (2.13)$$

where $\omega_{p,\text{ph},s}$ are the energies of the pump, phonon and Stokes respectively. The intensity of the Stokes light is inverse to the transition rate, which can be obtained from Eqs. (2.10), (2.11) using perturbation theory.

2.2.3 Measurements of the selection rule

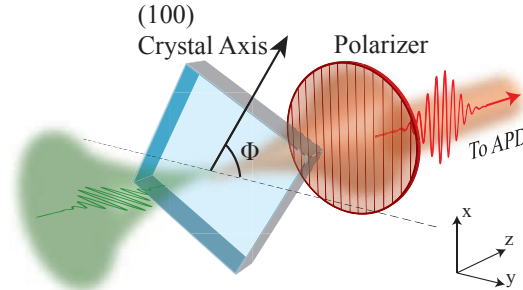


Figure 2.5 Schematic of the setup used to verify the polarisation selection rule of Raman scattering. An H polarised pump (green) is focussed into a diamond sample, and the intensity of vertically polarised Stokes signal (red) is measured on an APD as the diamond is rotated in the xy -plane.

The form of the Raman tensor Eq. (2.9) determines the selection rule of the pump/Stokes polarisation. I test this using a simple setup shown schematically in Fig. 2.5. A train of collimated (2 mm beam width) H-polarised, 80 MHz 60 fs pulses centred at 808 nm from a home built Ti:sapphire oscillator is focussed, with a 5 cm lens, into a diamond sample that is cut parallel to the the set of $\{100\}$ faces [an ‘electronic grade’ Chemical Vapour Deposited (CVD) sample provided by Element 6 Ltd.]. Light is collected from the forward direction using another 5 cm lens and the pump is rejected with dielectric filters, while a polarisation filter transmits the remaining V-polarised Stokes light centred at 905 nm. The Stokes signal is coupled into a single-mode fibre (SMF) and detected on a single photon sensitive Geiger-mode Avalanche Photodiode (APD) (PerkinElmer SPCM-AQ4C). Intensity of the V-polarised Stokes light is measured as the diamond is rotated through Φ in the xy plane, perpendicular to the propagation axis of the pump light, and is shown in

Fig. 2.6.

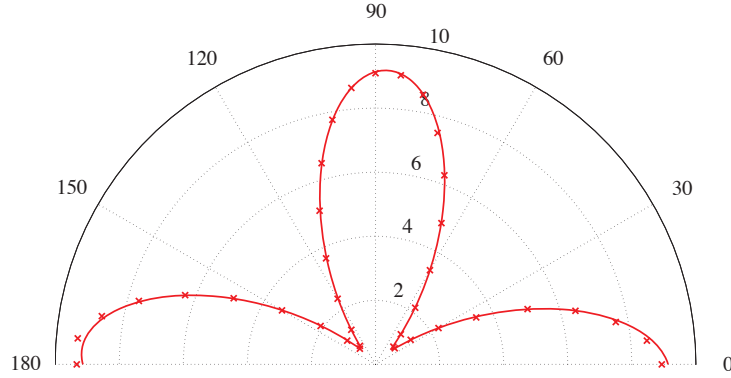


Figure 2.6 Measured intensity of Stokes light that is orthogonally polarised to the pump (in arbitrary units in the radial direction) as a function of diamond rotation Φ (in angular direction). Plotted are the measured values (crosses) and the theoretical curve (solid line).

Using the axes defined in Fig. 2.5, scattering cross section Eq. (2.8) and the Raman tensor Eq. (2.9), the theoretical intensity variation as a function of Φ can then be evaluated. Let

$$\epsilon_p = \begin{pmatrix} 1 \\ 0 \\ 0 \end{pmatrix}; \quad \epsilon_s = \begin{pmatrix} 0 \\ 1 \\ 0 \end{pmatrix},$$

and rotation around the xy plane by $\hat{R}(\Phi) = \begin{pmatrix} \cos \Phi & -\sin \Phi & 0 \\ \sin \Phi & \cos \Phi & 0 \\ 0 & 0 & 1 \end{pmatrix}$, then

$$I(\Phi) \propto \left| \sum_{k=\{x,y,z\}} \varepsilon_p^\dagger \hat{R}(\Phi) \hat{T}_k \hat{R}^\dagger(\Phi) \varepsilon_s \right|^2 \quad (2.14)$$

$$\propto a^2 \cos^2(2\Phi). \quad (2.15)$$

The quality of the measured Raman scattering selection rule depends both on the presence of defects in the diamond lattice^[124,125], and photon noise coupled into the APD — a mixture of imperfect pump filtering, fluorescence from the diamond and stray photons entering the APD enclosure. Motivated by Eq. (2.15), the measured values (marked by crosses) are plotted against a function of form $A \cos^2(2\Phi + B) + C$ (solid line in Fig. 2.6), where the parameters A, B, C are found by least square fitting to take into account of extra noise and an angular offset due to the mounting of the diamond sample. About 200 mW of average pump power was incident on the diamond sample, and each data point was measured for 60 s, with the dark counts of the APD (measured over 5 mins) subtracted from the measured values. Figure 2.6 clearly shows the expected 4-fold rotational symmetry, while the ratio A/C obtained from the fit is ~ 12 , indicating the experimental setup achieves a good level of stray photon filtering and the diamond sample is free of obvious lattice defects.

2.2.4 LO/TO phonon

One further point of interest that can be derived from the Raman tensor is the proportion of excitation of the longitudinal optical (LO) versus the transverse optical (TO) phonon given the geometry of the experimental setup. This has relevance to photon storage since one might expect, for example, that a storage excitation consisting of part LO and part TO to decay faster than the individual modes — in the theoretical analysis by Klemens^[126] the matrix element corresponding to an optical phonon decaying into two acoustic phonons consists of a sum over all phonon polarisations.

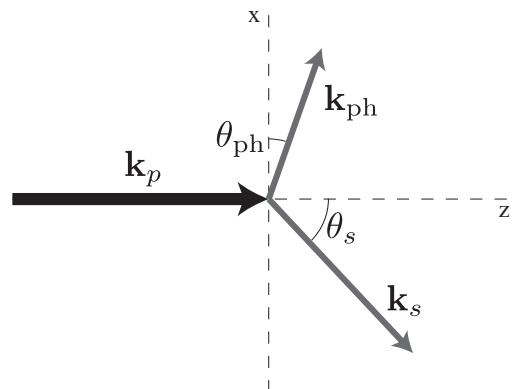


Figure 2.7 Geometry of Stokes scattering.

Consider the scattering geometry shown in Fig. 2.7. Let an incident pump, with wave vector \mathbf{k}_p parallel to the z axis and polarised along the y direction scatter from a diamond sample orientated with its principle axes parallel to x, y, z . A detector collects Stokes light emitted at an angle θ_s from the z axis and polarised in the xz

plane, such that the polarisation unit vectors are

$$\boldsymbol{\varepsilon}_p = \begin{pmatrix} 0 \\ 1 \\ 0 \end{pmatrix}, \quad \boldsymbol{\varepsilon}_s = \begin{pmatrix} \cos \theta_s \\ 0 \\ \sin \theta_s \end{pmatrix}. \quad (2.16)$$

Combining the conservation equations Eqs. (2.12), (2.13), the magnitude and direction of phonon wavevector are

$$|\mathbf{k}_{\text{ph}}(\theta_s)|^2 = \frac{1}{c^2} [n^2(\lambda_p)\omega_p^2 + n^2(\lambda_s)(\omega_p - \omega_{\text{ph}})^2 - 2n(\lambda_p)n(\lambda_s)\omega_p(\omega_p - \omega_{\text{ph}})\cos\theta_s], \quad (2.17)$$

$$\cos\theta_{\text{ph}} = \frac{n(\lambda_s)(\omega_p - \omega_{\text{ph}})}{c|\mathbf{k}_{\text{ph}}(\theta_s)|}\sin\theta_s, \quad (2.18)$$

where the wavelength dependent refractive index $n(\lambda)$ can be obtained from Sellmeier's equation for diamond (wavelength in μm)^[127]

$$n(\lambda) = \sqrt{1 + \frac{4.3356\lambda^2}{\lambda^2 - 0.1060^2} + \frac{0.3306\lambda^2}{\lambda^2 - 0.1750^2}}, \quad (2.19)$$

wave vectors $|\mathbf{k}_{p,s}| = n(\lambda_{p,s})\omega_{p,s}/c$, and $\lambda_{p,s}$ the pump, Stokes wavelengths are related by $\lambda_s^{-1} = \lambda_p^{-1} - \omega_{\text{ph}}/(2\pi c)$ in SI units.

Given that the Stokes field is detected at angle θ_s , the LO and TO phonon

polarisation vectors are

$$\mathbf{Q}_{\text{LO}} = \begin{pmatrix} \cos \theta_{\text{ph}} \\ 0 \\ \sin \theta_{\text{ph}} \end{pmatrix}, \quad \mathbf{Q}_{\text{TO}} = \begin{pmatrix} \sin \theta_{\text{ph}} \\ 0 \\ -\cos \theta_{\text{ph}} \end{pmatrix}. \quad (2.20)$$

Inserting Eqs. (2.16), (2.20) into Eq. (2.8), for pump wavelength $\lambda_p = 808$ nm, the contribution of the LO/TO modes to the Stokes scattering in the xz plane can be calculated and is shown in Fig. 2.8a. At $30^\circ < \theta_s < 330^\circ$, the cross sections in

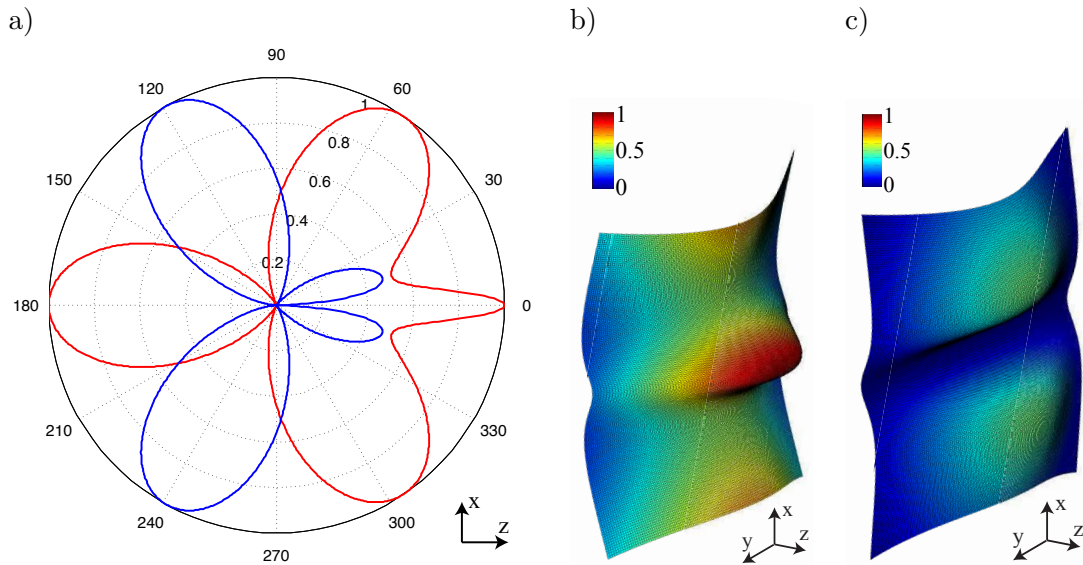


Figure 2.8 a) Scattering cross section (radial direction in normalised units) for the LO (red) and TO (blue) modes in diamond as a function of Stokes emission angle θ_s . 2D intensity profile of Stokes light b), c) scattered in the forward direction by LO and TO phonons respectively (the xy -plane represents the spatial coordinates of a collimation lens, and the intensity is plotted in the z direction).

Fig. 2.8a seem to indicate a pattern with 3-fold rotational symmetry, which may seem surprising at first given the cubic structure of diamond. As it turns out,

at large θ_s $\left[\sin^2 \frac{\theta_s}{2} \gg \left\{ \frac{\Delta n^2}{2n^2(\lambda_p)}, \frac{n(\lambda_s)\Delta n\omega_{\text{ph}}}{2n(\lambda_p)\omega_p}, \frac{n^2(\lambda_s)\omega_{\text{ph}}^2}{4n^2(\lambda_p)\omega_p^2} \right\}, \text{ where } \Delta n = n(\lambda_p) - n(\lambda_s) \right]$, taking the approximations $\omega_p \gg \omega_{\text{ph}}$, and $n(\lambda_p) \approx n(\lambda_s) = n_p$, Eqs. (2.17), (2.18) simplify to:

$$\begin{aligned} |\mathbf{k}_{\text{ph}}| &\approx \frac{2n_p\omega_p}{c} \left| \sin \frac{\theta_s}{2} \right| \\ \theta_{\text{ph}} &\approx \frac{\theta_s}{2}. \end{aligned}$$

The differential cross sections for the LO and TO mode scales in this regime are approximately $\frac{dS_{\text{LO}}}{d\Omega} \propto \sin^2 \frac{3\theta_s}{2}$, $\frac{dS_{\text{TO}}}{d\Omega} \propto \cos^2 \frac{3\theta_s}{2}$ respectively, which are both 3 fold rotationally symmetric functions.

In the experiments of this thesis, Stokes emission is collected in the forwards direction (along z axis). From the symmetry of the setup, collecting Stokes light emitted at an angle Φ from the xz plane is physically equivalent to rotating the diamond by the same angle (Fig. 2.5) and detecting in the xz plane. So, we combine the momentum conservation condition Eqs. (2.17), (2.18) with the angular dependence Eq. (2.14) and, using the polarisation vectors Eqs. (2.16), (2.20), the 2D emission patterns of the LO/TO scattering can be calculated. Figure 2.8b(c) map the emission profile of LO(TO) scattered light onto a planar lens placed in the forward direction, with the intensity $I(x, y)$ plotted along the z axis. Integrating

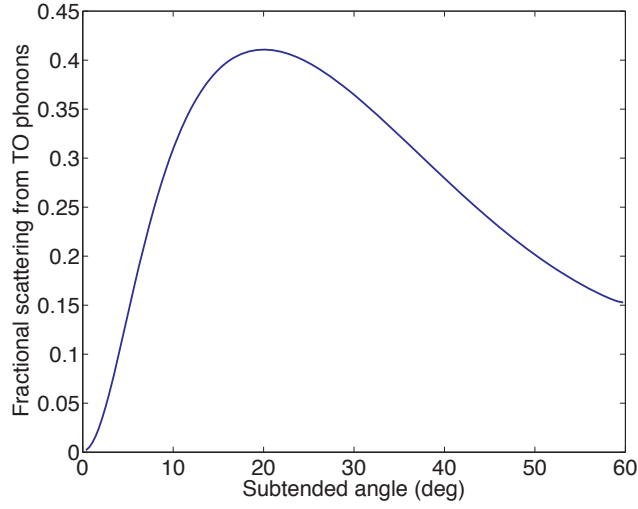


Figure 2.9 Proportion of Stokes light scattered from the TO branch as a function of collection angle.

the emission profiles over a circular area,

$$S_{\text{LO,TO}} = \int \frac{dS_{\text{LO,TO}}}{d\Omega}(\theta_s, \Phi) d\Omega$$

$$S_{\text{LO,TO}}(\theta) = \int_{-\theta}^{\theta} \int_{-\alpha(\theta_s)}^{\alpha(\theta_s)} \frac{dS_{\text{LO,TO}}}{d\Omega}(\theta_s, \Phi) \sin \theta_s d\theta_s d\Phi,$$

where $\alpha(\theta_s) = \sqrt{\tan^2 \theta - \tan^2 \theta_s}$, the resulting cross section $S_{\text{LO,TO}}$ represents the energies of the LO, TO scattered beams that are collimated by a lens which subtends the half angle θ . Figure 2.9 plots the fraction of the total Stokes beam energy that is scattered from the TO mode, $S_{\text{TO}}/(S_{\text{LO}} + S_{\text{TO}})$, as a function of θ . In the single photon experiments described in chapters 3 and 4, the Stokes beam is collimated by a 5 cm lens, and approximately 2 mm of the beam is coupled to SMF, so $\theta \sim 2.5^\circ$, corresponding to a fractional TO beam energy of $< 5\%$.

2.3 Transient Coherent Ultrafast Phonon Spectroscopy

The extraordinary physical properties of diamond and diamond-like materials continue to be an area of extensive research^[100,124,128,129]. Recent advancement in synthetic fabrication techniques has resulted in increased industrial and scientific application^[36,130,131]. A central source of diamond's uncommon electronic and thermal properties is its unique lattice and corresponding phonon features. A new spectral technique has been developed to characterize phonon decay: Transient Coherent Ultrafast Phonon Spectroscopy (TCUPS)^[129]. TCUPS is a convenient, spectral method for measuring phonon dephasing. Here, TCUPS is used to compare the phonon lifetime of natural, CVD, and High Pressure High Temperature (HPHT) diamond. The measurements are highly precise and repeatable, showing a significant variation between the CVD sample and the others.

Traditionally, the phonon lifetime has been indirectly measured via the inverse of the first order Raman linewidth^[86]. More recently, time-domain techniques have been developed that directly probe the time evolution of sample reflectivity or transmissivity, following impulsive phonon excitation with few-femtosecond laser pulses^[87,132]. While Raman spectroscopy employs steady-state fields and impulsive scattering utilizes short pulse durations comparable to vibrational times, TCUPS makes use of the intermediate, or transient regime^[133], where the pulse durations are comparable to the decay time of the phonon. Use of the transient regime reduces

some experimental challenges of impulsive studies, since readily available Ti:sapphire oscillators (of duration ~ 80 fs) can be used. TCUPS is also applicable in the spontaneous limit, and thus avoids heating and the excitation of the large phonon populations that can alter the apparent decay rate in stimulated Raman experiments^[134].

TCUPS can be understood from the perspective of the Young's slits experiment. In TCUPS two coherent and temporally separated broadband pump pulses are inelastically scattered from the diamond lattice and the scattered Stokes light is detected by an imaging spectrometer. At low power, strictly below threshold for stimulated Raman scattering, only one Stokes photon is spontaneously produced per pump pulse pair. The production of a Stokes photon from the first pump corresponds to one pathway and the production of a Stokes photon from the second corresponds to another. By detecting the Stokes photon on a slow detector, we project the Stokes photon to a superposition of the two pathways, resulting in spectral fringes provided that the two pathways are phase coherent. This mirrors the Young's slits case where the two pathways correspond to different spatial paths which a photon can take going through the slits. The spatial fringes in Young's slits and the spectral fringes in TCUPS arise irrespective of whether the photon itself was created coherently or not. As pump pulse separation is increased, phonon coherence decays, thus 'which-way' (or rather 'which-time') information becomes available to the environment and the Stokes spectral fringe visibility decreases.

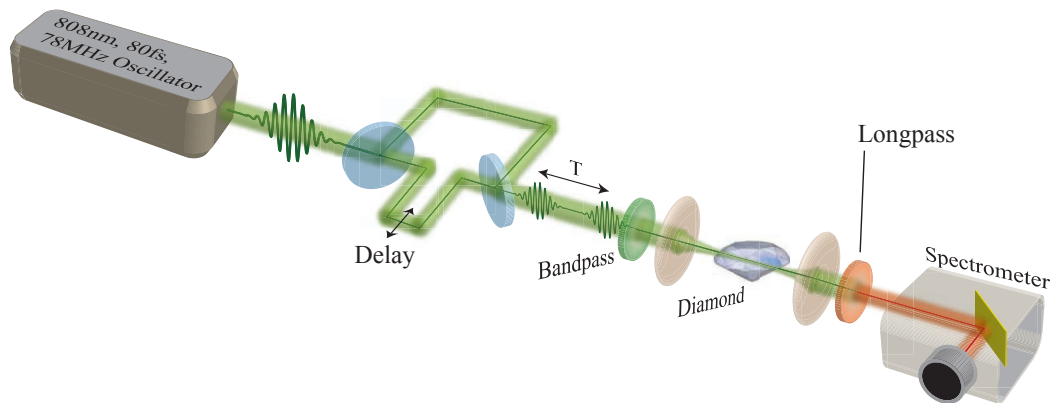


Figure 2.10 Experimental setup. An oscillator pulse is split into two time delayed pulses and focused through the diamond sample. A bandpass filter removes background oscillator modes before the diamond and a longpass filter rejects the pump and transmits the Stokes before the spectrometer.

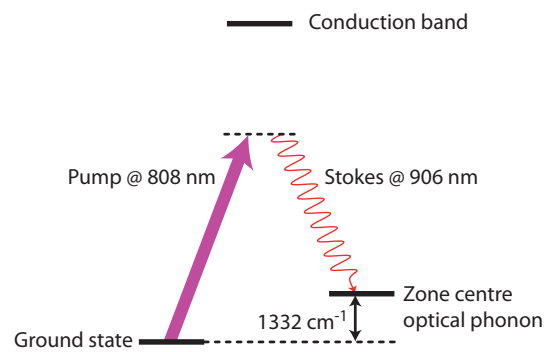


Figure 2.11 Stokes scattering transition in diamond. Ground state phonons are excited with the incident 808 nm pump, via a Raman transition, to the optical phonon mode, emitting an 906 nm Stokes pulse.

2.3.1 Experiment

In the experiment (Fig. 2.11), a pair of coherent pump pulses temporally separated by a few picoseconds are incident upon the diamond. The first pump pulse spontaneously Raman scatters off the diamond to create a Stokes photon and an optical phonon. Stokes generation from the second pulse is also spontaneously initiated by the vacuum fluctuation and both Stokes pulses are incident upon a slow detector. The two Stokes pulses are phase coherent with each other provided that they are initiated within the coherence time of the phonon, in which case they can interfere in a spectrometer to produce spectral fringes. As the pulse separation is increased, the visibility of the fringes decreases, thus permitting a measurement of the phonon dephasing time.

The pump is generated by a modelocked Ti:sapphire laser (Coherent Mira) of 80 fs duration, centered at 808 nm, is propagated through a Mach-Zehnder interferometer with an adjustable delay. Spectral fringes are created at the final beam splitter as a result of the interference, and the fringe spacing as a function of carrier wavelength, λ_0 , and time difference T , is given by $\Delta\lambda = \lambda_0^2/(cT)$. Care is taken to minimise phase fluctuations through the interferometer and in this experiment, no measurable phase drift is observed in the pump spectral fringes over the time scales of the measurements.

The pump pulses are then focused with a 50 mm AR-coated lens down to an area $\sim 600 \mu\text{m}^2$ through up to 0.5 mm of diamond (*i.e.*, Fresnel number ~ 0.1). A 30 cm spectrometer coupled to a Charge-Coupled Device (CCD) camera is used to

observe the spectral fringes of the Stokes light. The spectral fringe visibility is then measured as a function of the delay on the interferometer, which is tuned from 2 to 11.5 ps.

To obtain the coherence lifetime of the phonons in the diamond, I record the decay in spectral fringe visibility of the Stokes light with increasing temporal delay. Factors such as mechanical imprecision in the translation stage used in the interferometer and finite pixel widths of the CCD camera are also sources of fringe visibility reduction. The fringes are well sampled by the CCD at all delays. Other errors are mitigated by normalising the visibility of the Stokes light fringe visibility against that of the pump.

Diamond is a face-centered cubic lattice, with two carbon atoms per unit cell. The space group is $Fd\bar{3}m$ (O_h^7) and the crystal group is $m\bar{3}m$ (O_h). There is a triply degenerate optical phonon mode with vibrational symmetry T_{2g} (Γ_5^+). The first order Raman shift is 1332 cm^{-1} . The samples were all polished with faces on $\langle 100 \rangle$ such that polarization selection rules produce output Stokes light orthogonally polarized to the input^[112].

The Stokes-to-pump-photon ratio is of order 10^{-12} . A cooled CCD camera was used (iXon DU-897). To reduce noise from the laser oscillator, bandpass filters are utilised to eliminate high order spectral frequencies (Fig. 2.10). Visibility measurements at each time delay are taken over a period of 100 seconds.

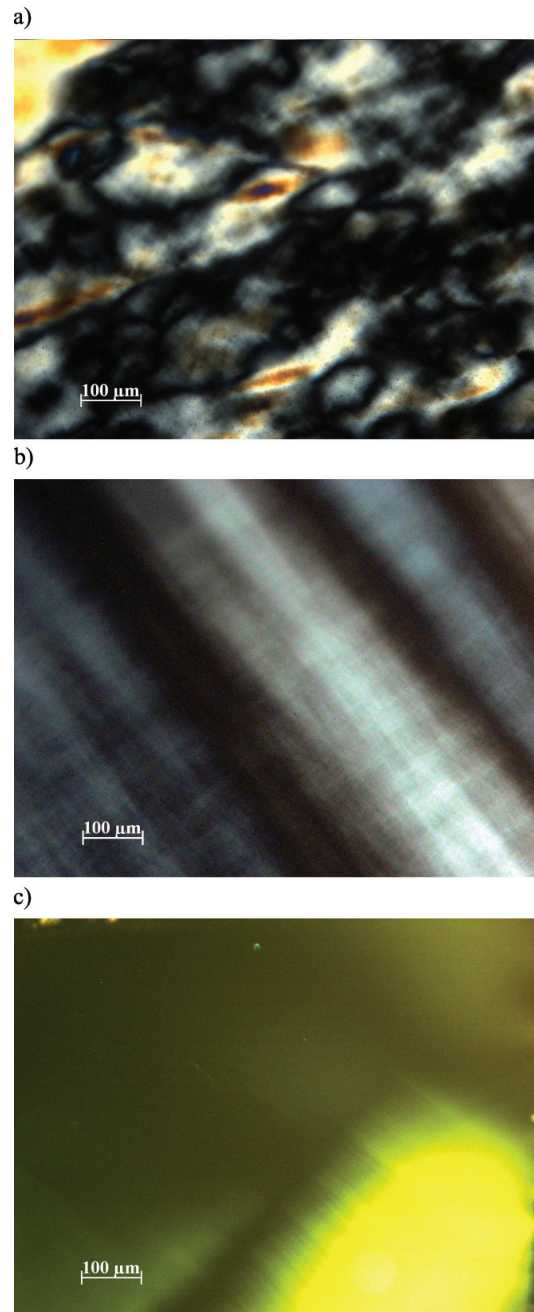


Figure 2.12 Cross polarised images of different diamonds at 10× magnification: a) CVD; b) natural IIa; c) HPHT.

2.3.2 Results

Three different types of diamonds were investigated. The first was a single crystal diamond plate ($3 \times 3 \times 0.5$ mm) synthesized by Chemical Vapour Deposition (CVD). The manufacturer (Element 6) specifications are that the impurity level is < 1 ppm N and < 0.05 ppm B with a low dislocation density at $< 10^4$ cm^{-2} (Fig. 2.12a). Whilst the cross polarised image reveals irregular birefringence patterns caused by local stress and strain, there are no significant straight line features associated with dislocations. The second sample was a natural type IIa slab of dimensions $3 \times 3 \times 0.25$ mm. Such samples, whilst typically pure, with a N and B concentration of less than 1 ppm, have high dislocation density of order $\sim 10^8 - 10^9$ cm^{-2} ^[135]. Indeed imaging under cross polarizers (Fig. 2.12b) reveals a dense network of dislocations, which appear as alternating dark and bright stripes. The last sample studied was a high pressure, high temperature diamond ($3.2 \times 3.2 \times 0.42$ mm), yellow in colour, with a N concentration of between 10 and 100 ppm (Fig. 2.12c). This sample showed similar dislocation density to the CVD, if not lower. The yellow and black parts in Fig. 2.12c represent different growth sectors of the diamond where the crystal lattice orientations are different from each other. Ultraviolet photoluminescence images of the diamond samples have shown that both the nitrogen impurities and dislocations are uniformly distributed in the 3 samples.

Figure 2.13 shows the Stokes fringe visibility as a function of pump delay time (given on the left of each column). As expected, the spectral fringes in the Stokes spectrum are observed with fringe visibility decaying exponentially with pump delay.

A least squares fit to the function $A_0 + A_1 \cos[A_2\lambda + A_3]$ (where A_i 's are the fitted numbers and λ is the wavelength) was applied to the data and the extracted fringe visibility, defined as A_1/A_0 , is plotted as a function of delay time in Fig. 2.14 for each of the 3 various diamonds in one run of the experiment.

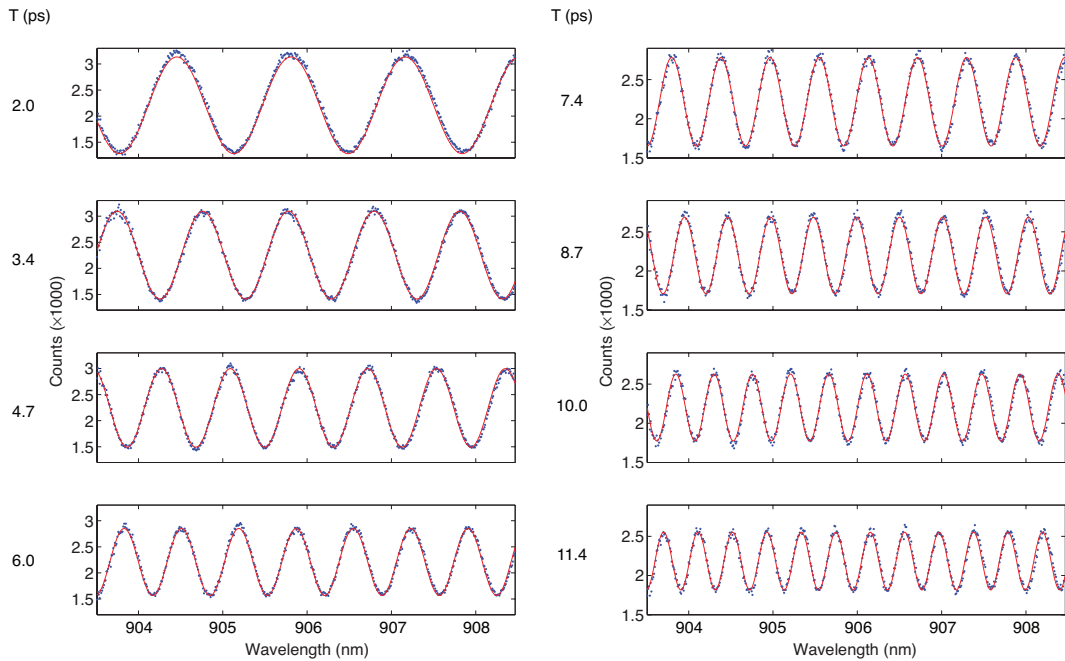


Figure 2.13 Stokes spectral fringe visibility as a function of pump delay (on the left of each column). For clarity, we have plotted half of the data generated from one run of TCUPS measurement, and we have used different “Counts” scales for the left (2 to 6ps) and right (7.4 to 11.4ps) columns. The spectral fringes in the Stokes spectrum are observed with fringe visibility decaying exponentially with pump delay. The blue dots represent actual data and the red lines are the least square best fit lines used to calculate the visibility of the spectral fringes.

From the data in Fig. 2.14 the phonon decoherence time may be deduced for each sample. The lifetimes are summarised in table 2.2, which also shows the corresponding FWHM linewidths. It should be noted that each piece of diamond was measured

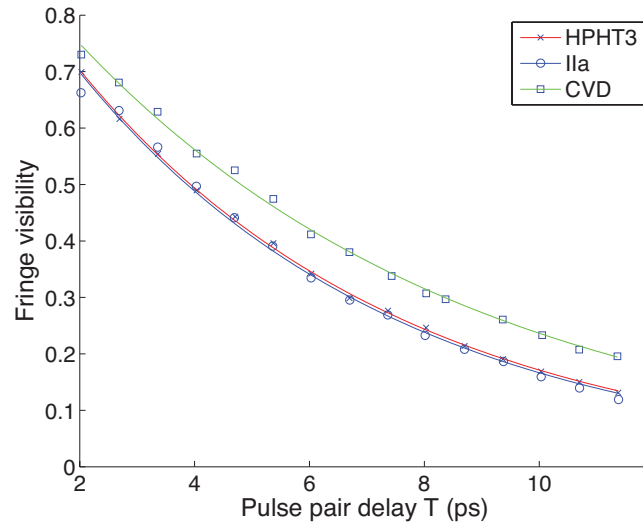


Figure 2.14 A plot of spectral fringe visibility versus path delay set by the interferometer. These are typical runs obtained from the 3 diamonds.

five times, non-sequentially, and the combined lifetime values have a variance of less than 0.2 ps. In order to achieve such repeatability, care has to be taken to ensure that the focusing lens following the diamond is well positioned to collect the Stokes light and that it is brought sharply into focus as it enters the spectrometer.

For comparison, the phonon linewidths have also been measured with the traditional Raman spectroscopy technique by P. Spizzirri, one of my co-authors in the associated publication^[115]. A 532 nm Continuous Wave (CW) pump was used in conjunction with a Renishaw inVia microscope, and the first order Raman spectra are shown in Fig. 2.15 — a detailed discussion of the linewidth function is found in^[136,137]. As expected, the CVD sample has a narrower linewidth than the other two samples, at $\sim 2.1 \text{ cm}^{-1}$ and 2.4 cm^{-1} ($\pm 0.07 \text{ cm}^{-1}$) respectively. To enable

Diamond Type	TCUPS			
	Lifetime ps	Error ps	Linewidth cm^{-1}	Error cm^{-1}
CVD	7.0	± 0.2	1.5	± 0.07
IIa	5.7	± 0.2	1.9	± 0.07
HPHT	5.7	± 0.2	1.9	± 0.07

Table 2.2 Diamond decoherence times and linewidths, as measured by TCUPS and conventional Raman spectroscopy. The errors, in both cases, correspond to the standard deviation of the lifetimes from 5 separate measurements on each diamond.

direct comparison of linewidths, the spectroscopic data were fitted to a Lorentzian linewidth function, though the absolute linewidth values obtained from curve fitting processes vary significantly depending on the form of the function being used. Factors such as the response function of the Renishaw spectrometer and a finite pump bandwidth require full characterisation of the setup and further processing of spectroscopic data. This is beyond the scope of the current work. However, it is worth noting that both TCUPS and the Raman spectroscopic measurements showed identical differences in phonon linewidths within the accuracy of both techniques.

2.3.3 Theory

The first control pulse is inelastically scattered from the optical phonon of the diamond, creating Stokes light. The second pulse then inelastically scatters off the diamond to create a second Stokes pulse; there exists a definite phase relation between the two Stokes pulses which is limited by phonon decoherence time. The main source of decoherence in this picture is the anharmonic decay of the optical phonon^[126].

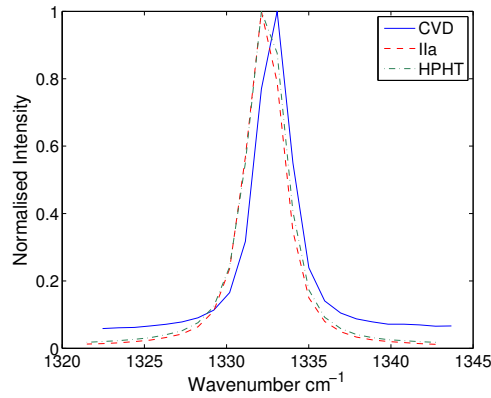


Figure 2.15 The first order Raman spectra of the diamond samples. The CVD sample showed an intensity offset due to the presence of a broadband background fluorescence.

Due to collective enhancement arising from the coherence and geometry of the excitation pulse, Stokes light is principally scattered from one phonon mode into one optical mode in the forward direction^[138]. Consequently, the dynamics can be understood in terms of a single phonon mode operator \hat{B} and a signal optical mode operator \hat{A} , as shown below.

Effective Hamiltonian

In complete analyses of the Raman interaction^[45,70,139,140], propagation effects of the Stokes light are taken into account by using Maxwell's wave equation, where the excitation of the medium acts as a source term. Both the Stokes light and excitation in the medium are decomposed into longitudinal and transverse modes. The analysis here can be simplified for two reasons, which allow the theoretical modelling of the full 3D interaction to be restricted to one longitudinal and transverse mode. The

single longitudinal mode behaviour arises from the linearity of the Raman scattering in the spontaneous limit (in my experiment, the probability of Stokes generation is $\sim 0.1\%$ per pulse). Consequently every atom in the medium interacts with the input field in the same way and therefore the propagation effects, responsible for the various longitudinal modes, can be ignored^[138] (see section 1.3.4). Furthermore, as the Fresnel number of the optical setup in my experiment is smaller than 1, all higher transverse modes can also be ignored^[140].

With the rotating wave approximation, the Raman Hamiltonian is given by

$$\hat{H}(t') = \kappa E_P(t') \hat{E}_S^\dagger(t') \hat{B}^\dagger(t') + \text{H.c.} \quad (2.21)$$

where \hbar is again set to 1 for convenience, t' is the co-moving time $t' = t - z/c$, z is the distance along pump beam propagation, $E_P(t')$ is the classical pump, and $\hat{E}_S^\dagger(t')$ is the Stokes mode operator. The phonon creation operator is given by $\hat{B}^\dagger(t')$ and κ represents the coupling responsible for the Stokes creation, which is the product of various matrix elements associated with the different exciton-phonon interactions in Stokes generation^[112].

To understand the spectral characteristics of the generated Stokes light, I re-write Eq. (2.21) in terms of $\tilde{E}_P(\omega)$, $\hat{\tilde{E}}_S^\dagger(\omega)$, $\hat{\tilde{B}}^\dagger(\omega)$, the Fourier transformed quantities of $E_P(t')$, $\hat{E}_S^\dagger(t')$, $\hat{B}^\dagger(t')$ respectively assuming the phonon to be sharply peaked at ω_{ph}

$$[\hat{B}^\dagger(t') = \hat{\tilde{B}}^\dagger(\omega_{ph}) \exp\{-i\omega_{ph}t'\}]$$

$$\begin{aligned} \hat{H}(t') \simeq & \kappa \int \int \tilde{E}_P(\omega) \hat{\tilde{E}}_S^\dagger(\omega') \hat{B}^\dagger e^{i(\omega - \omega' - \omega_{ph})t'} d\omega d\omega' \\ & + \text{H.c.} \end{aligned} \quad (2.22)$$

For brevity I now take \hat{B}^\dagger to mean $\hat{\tilde{B}}^\dagger(\omega_{ph})$. This is followed by integration over z to give an effective Hamiltonian treating the whole ensemble as a single system

$$\hat{H}_{\text{eff}} = g \hat{S}^\dagger \hat{B}^\dagger + \text{H.c.} \quad (2.23)$$

where $\hat{S} = \int \Omega(\omega) \hat{a}(\omega) d\omega$ is the superposition annihilation operator for Stokes light [$\hat{a}(\omega)$ is the individual Stokes mode annihilation operator],

$$\Omega(\omega) = \frac{\tilde{E}_P(\omega)}{\sqrt{\int |\tilde{E}_P(\omega')|^2 d\omega'}} \quad (2.24)$$

is the normalised pulse envelope, the effective coupling in the frequency domain is^[70,141]

$$g = \kappa \sqrt{\int |E_P(\omega)|^2 d\omega}. \quad (2.25)$$

Here, $\kappa \propto \Delta^{-2}$ ^[112], where Δ is the detuning of the pump away from the intermediate exciton state which is at 5.2 eV above the ground state^[142]. Since the detuning Δ is much larger than the bandwidth of the pump pulse, I take g to be constant. Starting from Eq. (2.23), I provide both the Heisenberg and Schrödinger pictures to explain

the presence of spectral fringes in the Stokes spectrum and the decay of these fringes.

Heisenberg picture

Stokes generation The sequence of Stokes generation and phonon decay is analysed in a piecewise manner (Fig. 2.16). By ignoring dephasing effects during the short duration of the pump, the equation of motion of the operators obtained from Eq. (2.23) are

$$\dot{\hat{S}}(t) = ig\hat{B}^\dagger(t) \quad (2.26)$$

$$\dot{\hat{B}}(t) = ig\hat{S}^\dagger(t). \quad (2.27)$$

After time $t = \tau$, the pump duration, the solutions are given by

$$\hat{S}^\dagger(\tau) = \cosh(g\tau)\hat{S}_0^\dagger - i\sinh(g\tau)\hat{B}_0 \quad (2.28)$$

$$\hat{B}(\tau) = i\sinh(g\tau)\hat{S}_0^\dagger + \cosh(g\tau)\hat{B}_0. \quad (2.29)$$

\hat{S}_0, \hat{B}_0 are the annihilation operators for Stokes photon and phonon respectively at $t = 0$. I then obtain the Stokes spectrum by calculating the expectation value of the operator $\hat{a}^\dagger(\omega, \tau)\hat{a}(\omega, \tau)$. Note that the Heisenberg equation of motion for the Stokes photon annihilation operator can also be obtained from Eq. (2.23)

$$\dot{\hat{a}}(\omega, t) = ig\Omega^*(\omega)\hat{B}^\dagger(t) \quad (2.30)$$

$$\hat{a}(\omega, \tau) = i\Omega^*(\omega) \left\{ -i[\cosh(g\tau) - 1]\hat{S}_0 + \sinh(g\tau)\hat{B}_0^\dagger \right\}. \quad (2.31)$$

The solution given in Eq. (2.31) requires the solution given in Eq. (2.29). Thus the Stokes spectrum is

$$I(\omega) = \langle \hat{a}^\dagger(\omega, \tau) \hat{a}(\omega, \tau) \rangle \quad (2.32)$$

$$= |\Omega(\omega)|^2 \sinh^2(g\tau) \langle \hat{B}_0(\omega) \hat{B}_0^\dagger(\omega) \rangle \quad (2.33)$$

$$= |\Omega(\omega)|^2 \sinh^2(g\tau), \quad (2.34)$$

assuming there is negligible phonon population in the thermal state. For small coupling $g\tau$ the spectral shape of $I(\omega)$ is proportional to the spectrum of the pump light $|E_P(\omega)|^2$.

Phonon decay In between the two pump pulses, the effects of phonon dephasing are included by adding a phenomenological decay term:

$$\dot{\hat{B}}(t) = -\Gamma \hat{B}(t). \quad (2.35)$$

A full quantum treatment would include a Langevin operator in Eq. (2.35) to maintain commutator relations for \hat{B} such that $\langle [\hat{B}_i(t), \hat{B}_i^\dagger(t)] \rangle = 1$ for all times. Alternatively the normally ordered operator may be used when calculating expectation values for the same effect^[129,141].

The solution after time $t = T$, the delay between the two pump pulses, is given by

$$\hat{B}(T + \tau) = \hat{B}(\tau) e^{-\Gamma T}. \quad (2.36)$$

Pulse sequence For the last part of the pulse sequence, the Stokes generation is once again governed by Eqs. (2.28) & (2.29). Since the pump pulses are temporally separated, I assume that the second Stokes generation is initialised by $\hat{B}(T + \tau)$ in Eq. (2.36) only.

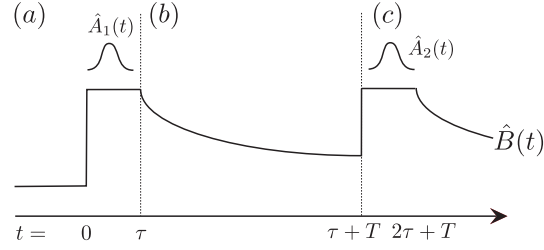


Figure 2.16 Evolution of the phonon. (a) Phonon is spontaneously created by a pump pulse and evolves as Eqs. (2.28) & (2.29). (b) The phonon decays for time T via Eq. (2.35). (c) A second pump pulse scatters off $\hat{B}(T + \tau)$.

To differentiate between Stokes and phonon modes involved in the first and second pulses, I use subscripts $i \in \{1, 2\}$, thus, $\hat{S}_1(t), \hat{B}_2(t)$ denote the Stokes operator during the first pulse and phonon operator during the second pulse respectively. From the above arguments, I also write the initial phonon operator of the second pulse as $\hat{B}_{0,2} = \hat{B}(T + \tau) = \hat{B}_1(\tau)e^{-\Gamma T}$. Using this notation, the signal detected by the spectrometer is represented by the operator

$$\hat{a}_D(\omega) = \frac{1}{\sqrt{2}} [\hat{a}_1(\omega, \tau) + \hat{a}_2(\omega, \tau)e^{i\omega T}]. \quad (2.37)$$

In terms of the initial operators, the Stokes spectrum is given by

$$I(\omega) = \langle \hat{a}_D^\dagger(\omega) \hat{a}_D(\omega) \rangle \quad (2.38)$$

$$\begin{aligned} &= |\Omega(\omega)|^2 (g\tau)^2 \langle \hat{B}_{0,1} \hat{B}_{0,1}^\dagger \rangle + |\Omega(\omega)|^2 (g\tau)^2 e^{-\Gamma T} \cos(\omega T) \langle \hat{B}_{0,1} \hat{B}_{0,1}^\dagger \rangle \\ &\quad + O[(g\tau)^4]. \end{aligned} \quad (2.39)$$

Motivated by the fact that the Raman interaction is in the weak coupling spontaneous regime, I only keep terms that are up to second order in the effective coupling ($g\tau$). The first term represents spontaneously scattered Stokes light from both pulses. Spectral fringes are generated by the second term, which decays. The exponential factor represents the decay of coherence, which is measured in this experiment. Assuming negligible thermal phonon population, I calculate the expectation values of the operators to give

$$I(\omega) \simeq |\Omega(\omega)|^2 (g\tau)^2 (1 + e^{-\Gamma T} \cos \omega T). \quad (2.40)$$

Even though there is no stimulation at the lowest order, the Stokes pulses are coherent within the lifetime of the phonon.

Standard diamond lifetime measurements in the literature^[134,143,144] involve the direct measurement of phonon lifetime, which in the operator language is given by

$$\langle \hat{B}^\dagger(T) \hat{B}(T) \rangle \propto e^{-2\Gamma T} \langle \hat{B}^\dagger(0) \hat{B}(0) \rangle. \quad (2.41)$$

The Raman linewidth in frequency space is given by $\Gamma = 2/T_2$ where T_2 is the coherence lifetime^[145]. In cm^{-1} , the linewidth is $\delta\nu = (\pi c T_2)^{-1}$.

It has been shown (see^[146,147] and references therein) that the anharmonic phonon self energy, the term in the Hamiltonian describing phonon-phonon interactions and is the main cause of phonon decay, is a frequency dependent term. This implies that the spectral fringe visibility would not decay exponentially with pump pulse separation. However, note that in the single phonon regime and at room temperature, the experimental data fit the predicted exponential decay curve (Fig. 2.14) well, and the more sophisticated modelling of phonon decay which includes such frequency dependence can be ignored.

Schrödinger picture

In the Heisenberg picture, I have derived the evolution of the joint photon-ensemble system by calculating the time evolution of the operators and deriving the expectation values. It is worthwhile to contrast the solutions with those obtained from the Schrödinger picture. For short pulses, the unitary operator \hat{U} corresponding to evolution of the initial (vacuum) state by the Hamiltonian Eq. (2.23) can be perturbatively expanded up to first order,

$$\hat{U}(\tau) = e^{i\hat{H}\tau} \quad (2.42)$$

$$\Rightarrow |\psi_f\rangle \simeq (\mathbb{1} + i\hat{H}\tau) |0\rangle \quad (2.43)$$

where the initial vacuum state $|0\rangle$ is connected to the final state $|\psi_f\rangle$ via the Raman interaction. The higher order terms, including the stimulated emission, are not included.

Denoting operators associated with the first and second pulse with the subscripts 1, 2 respectively, the two pulse interaction is written as

$$|\psi_f\rangle = \hat{U}_2(\tau)\hat{U}_1(\tau)|0\rangle \quad (2.44)$$

$$\simeq \left[\mathbb{1} + ig\tau \left(\hat{S}_2^\dagger \hat{B}_2^\dagger + \hat{S}_1^\dagger \hat{B}_1^\dagger \right) \right] |0\rangle. \quad (2.45)$$

As in the Heisenberg treatment, I obtain the Stokes spectrum by taking the expectation value of the operator $\hat{a}_D^\dagger(\omega)\hat{a}_D(\omega)$ in Eq. (2.37), this time, with state $|\psi_f\rangle$.

The detected signal is

$$I(\omega) = \langle \psi_f | \frac{1}{2}(\hat{a}_1^\dagger \hat{a}_1 + \hat{a}_2^\dagger \hat{a}_2) + \mathbb{R} \left\{ \hat{a}_1^\dagger \hat{a}_2 e^{i\omega T} \right\} | \psi_f \rangle \quad (2.46)$$

$$= (g\tau)^2 |\Omega(\omega)|^2 \left[\langle 0 | \frac{1}{2}(\hat{B}_1 \hat{B}_1^\dagger + \hat{B}_2 \hat{B}_2^\dagger) | 0 \rangle + \cos(\omega T) \langle 0 | \hat{B}_1 \hat{B}_2^\dagger | 0 \rangle \right]. \quad (2.47)$$

As before, I take the normally ordered operators and use the same arguments in section 2.3.3 to relate \hat{B}_1 and \hat{B}_2 , after which $I(\omega)$ becomes (2.40).

The utility of the Schrödinger picture is that it emphasizes the analogy with Young's two-slit experiment. After the full TCUPS interaction, the joint photon-ensemble state $|\psi_f\rangle$ is given by Eq. (2.45), where the subscripts denote the two

pathways for Stokes photon generation. The state $|\psi_f\rangle$ contains a coherent superposition of the two pathways and spectral fringes in the Stokes spectrum appear after the two pathways are allowed to interfere in a slow detector. It is also useful to note that the Raman Hamiltonian is of the same form as that of parametric down conversion^[148]. In this sense, the generated state is expected to be a two-mode squeezed state which can be used to entangle the optical phonon and the Stokes photon.

2.3.4 Experimental conditions

TCUPS is a robust tool for investigating material properties at the picosecond time scale, and allows a high degree of freedom in the choice of experimental parameters. The theoretical analysis above assumed three main conditions: spontaneous Stokes generation, pump pulse duration within the transient regime for the medium excitation, and single mode interactions.

In order to avoid any stimulated scattering, the effective Raman coupling strength g should be kept low. The measured rate of Stokes photon generation in my experiment corresponds to $g\tau \sim 10^{-2}$. A low coupling strength could be achieved providing the peak field strength of the pump pulse is not too strong and the Raman detuning from the exciton state, Δ , is large (see Fig. 2.11). For diamond, the conduction band is 5.5 eV above the ground state, which corresponds to 225 nm^[149]. This is energetically well above the pump pulse photons in my experiment.

As well as keeping the parameter $g\tau$ small, a short pulse serves to keep the Raman interaction within the transient regime. The coupled equations Eqs. (2.26)

& (2.27) model the Raman interaction in the absence of any dephasing effects. In this case, the phonon coherence lifetime can be as short as 5 ps, which limits pump pulse durations to less than 500 fs.

For accurate results, both pump pulses must address the same single excitation mode in the diamond. By maintaining the Fresnel number of the confocal setup at < 1 , only one transverse mode is excited in the diamond. This therefore sets an upper limit to the spot size that could be sampled in the diamond. In my measurements, the focused spot size was arbitrarily chosen to be $600 \mu\text{m}^2$ and I have found that T_2 lifetimes measured on different spots on the diamond are identical within the accuracy of TCUPS. I anticipate, however, that measurements made with a more tightly focused spot size and sampling volume may be more sensitive to local variations in the diamond samples. Thus, if the sample contains uneven concentration of dislocations and impurities, then T_2 measurements would be location specific.

2.3.5 Discussion

The anharmonic decay time of diamond at zero temperature and pressure has been calculated as 10.5 ps (1.01 cm^{-1})^[150]. This calculated lifetime is based upon the spontaneous decay of an optical phonon into two acoustic phonons. The observed widths of the literature, however, vary considerably from 1.2 cm^{-1} to 4.75 cm^{-1} ^[86,87,134,143,144]. The large variance is due to a number of factors including: spectrometer limitations, source linewidths, isotopic mass defects, nitrogen impurities, crystal boundaries, and stress gradients^[124].

Here, TCUPS has been used to differentiate the optical phonon lifetimes of CVD, HPHT and natural (IIa) diamonds. The results in table 1 reveal a somewhat unexpected difference between the three type of diamond samples that would normally be difficult to observe using more standard Raman scattering techniques. The CVD sample consistently shows a longer lifetime than either the natural or HPHT samples. Two obvious sources of phonon scattering in diamonds are impurities (most notably N) and dislocations. Despite the fact that the type IIa sample is clear and contains a low level of N, whereas the HPHT sample is yellow containing up to 100 ppm of N, there appears to be very little difference in the phonon lifetime. On the other hand, the CVD sample, with an N concentration of the same order of magnitude as the IIa sample, shows a lifetime approximately 20% longer. The dislocation density is much higher in the IIa sample than the single crystal CVD. A tentative conclusion might therefore be that reducing the dislocation density results in an increase in the lifetime and might be a more important factor in phonon scattering than the N impurities.

It is noteworthy that the present technique is sufficiently sensitive to reveal such differences. Measurement of the absolute peak width in Raman scattering is often subject to much higher errors than the 0.07 cm^{-1} achieved here. It is also noteworthy that the present technique samples a comparatively large volume of the sample ($\sim 10^{-4} \text{ mm}^3$) as compared to micro-Raman sampling whilst avoiding issues resulting from the presence of hot phonons.

While the decoherence time of diamond is long for phonon modes in solids,

it is short in comparison to many other molecular, atomic, and nuclear degrees of freedom. Nevertheless, diamond's large Raman shift allows for easy spectral filtering and the convenience of working with a room temperature solid. As noted, the Raman interaction Hamiltonian can be used to create a two-mode squeezed state between the optical phonon and the Stokes photon. In TCUPS this phonon coherence was created and measured using femtosecond pulses. Whilst the absolute lifetime of the phonon is short, it is still 2 orders of magnitude longer than the interaction time needed to create the excitation, and one can also in principle perform many coherent operations within the phonon lifetime. Thus there is the interesting possibility that diamonds and their phonon modes might be useful for implementations of quantum information protocols.

2.3.6 Notes on experimental apparatus

As mentioned earlier, mechanical imprecision of the translation stage in the interferometer and finite pixel size of the CCD camera adversely affects the accuracy of the measured visibility of the Stokes spectral fringes. The full alignment procedure for the translation stage will be detailed in section 4.2 since it is a recurring component in all of the experiments in this thesis. For the moment, I would like to discuss a few issues that arose from using the Andor spectrometer.

Figure 2.17 shows the drop off in the visibility of the pump spectral fringes with optical delay — due to a mixture of beam walk-off and limited spectrometer resolution, as will shortly be explained. The visibility is obtained via the same least

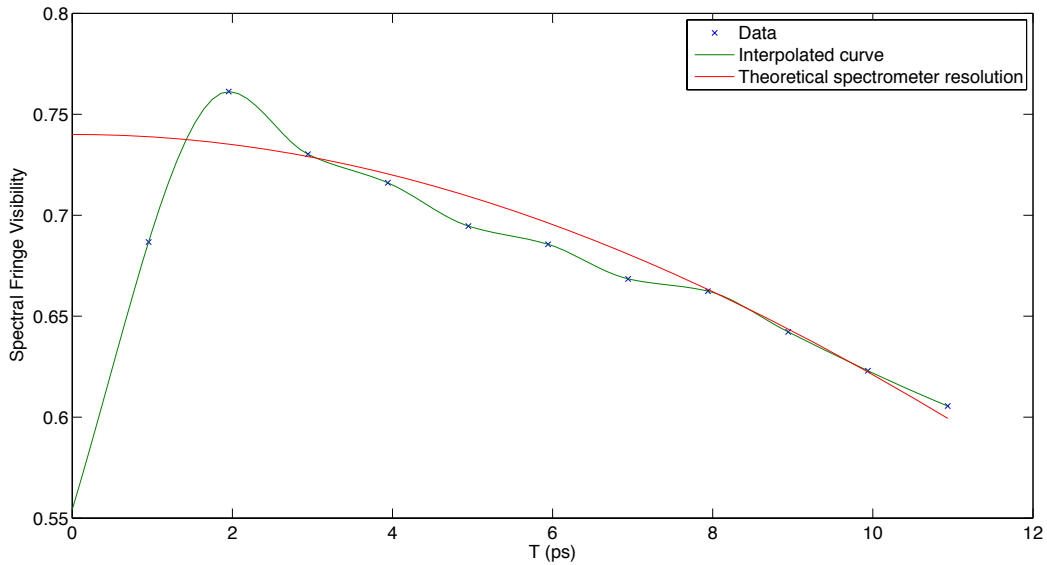


Figure 2.17 Pump spectral fringe visibility as a function of optical delay, used for normalisation in the TCUPS experiment.

square fitting process used for the Stokes pulse (marked by crosses). At the time of the experiment, I only had access to a standard Thorlabs 50:50 BS, which has a highly polarisation dependent reflectivity, for use in the interferometer. As a result, the first pump pulse had more than twice the energy of the second, limiting the maximal achievable visibility in the spectral fringes.

In the Andor spectrometer, a reflection grating maps different frequency components of the incident light into a range of reflection angles, and a CCD camera records this distribution of light, where each pixel records the total intensity emitted within a small spread of frequencies. The output recorded on a computer is therefore a version of the ‘true’ incident spectrum that has been discretised both in frequency space as well as intensity [through the analogue-to-digital (A/D) conversion process

during signal readout]. This process leads to a degradation of the measured spectral fringe visibility at high pump pulse separations (when the peak-to-peak separation of the spectral fringes is smaller). To obtain an analytical expression for this effect, I evaluated the following two integrals to obtain an estimate of the ‘discretised visibility’ V_{dis} :

$$I_{\text{max}} = \int_{-w}^w \int_{\lambda_{\text{max}} + \delta - \frac{w}{2}}^{\lambda_{\text{max}} + \delta + \frac{w}{2}} [A_0 + A_1 \cos(A_2\lambda + A_3)] d\lambda d\delta \quad (2.48)$$

$$I_{\text{min}} = \int_{-w}^w \int_{\lambda_{\text{min}} + \delta - \frac{w}{2}}^{\lambda_{\text{min}} + \delta + \frac{w}{2}} [A_0 + A_1 \cos(A_2\lambda + A_3)] d\lambda d\delta \quad (2.49)$$

$$V_{\text{dis}} = \frac{I_{\text{max}} - I_{\text{min}}}{I_{\text{max}} + I_{\text{min}}}. \quad (2.50)$$

I_{max} represents the total power incident on a pixel of spectral width w (integration over λ) around one of the maxima in the spectral fringe (at wavelength λ_{max}) — the intrinsic spectral distribution reflected from the grating is given by the integrand. Each spectral intensity maxima can also be centred on different spots within the pixel, and in a typical measurement, multiple peaks appear, thus a second integral in Eq. (2.48) over δ represents the averaging of all the discretised maxima signals. I_{min} calculates the equivalent averaged discretised minima signal around the minima points λ_{min} .

Using Eq. (2.50), the discretised visibility is

$$V_{\text{dis}} = \frac{A_1}{D_0} \text{sinc} \frac{A_2 w}{2} \text{sinc} A_2 w, \quad (2.51)$$

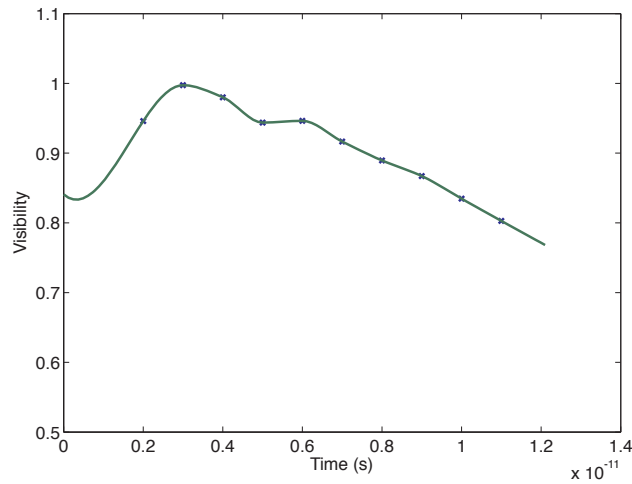


Figure 2.18 Numerical simulation of the effect of finite pixel size of the CCD on the measured spectral fringe visibility. The green line is an interpolated curve for the sampling points denoted by the crosses.

where A_2 is a function of optical delay T , and the spectral width w is found by fitting against the measured data in Fig. 2.17 (red line). The fitted width w is around 5 times the actual pixel size of the CCD. This is probably due to a mixture of charge leakage between adjacent pixels in the CCD and coupling of higher order pump modes into the spectrometer.

As well as the analytical solution, I simulated the finite pixel effect by generating a set of discretised spectrums by numerical integration and applied the least square fitting methods employed for the experimental data. Figure 2.18 shows the resulting simulated visibility drop off as a function of optical delay using the fitted w obtained from the analytical solution, assuming that both pump pulses have the same energy (therefore achieving unit visibility at short optical delays). Note that the interpolated curves in Fig. 2.17, 2.18 share similar features, and in particular, the ‘wobble’

of the fitted data around the theoretical curve in Fig. 2.17 is most likely due to inaccuracies (though insufficient to affect the measured lifetimes significantly) caused by the curve fitting algorithm rather than any beam walk off due to misalignment of the translation stage. It should be noted, however, that the phonon lifetimes are not significantly affected by the use of the theoretical (red) or interpolated (green) lines in Fig. 2.17 as the normalisation curve.

Chapter 3

Anti-Stokes readout in diamond

3.1 There's something about the phonon...

In the previous chapter, I have analysed the Stokes scattering process which leads to the simultaneous creation of a Stokes photon and an optical phonon, where an incident pump photon scatters from the crystal and transfers energy from the photon field into a lattice vibrational mode. This chapter deals with what happens when a second, classical probe pulse scatters from the phonon. Here, the energy transfer can be reversed — a probe photon can absorb the energy from the existing lattice vibration and leaves with increased energy in a process that is normally referred to as anti-Stokes scattering (see Fig. 1.7 for a comparison between the two scattering events). A classical analogy to this second type of scattering can be found in the manner in which a ball thrown against a vibrating wall can sometimes bounce back with a higher energy. Observing many of these events where the ball bounces back

with more energy, one may learn about the nature of the vibration. In the case of diamond, since the lattice vibration is created initially by Stokes scattering, one may learn about the phonon by analysing correlations between Stokes and anti-Stokes photons created from the scattering of a pump-probe pair. The Raman scatterings described in this thesis take place in the single photon regime, where the phase information created in a single quanta of phonon is coherently transferred to a single anti-Stokes photon. Through the scattering mechanism, the results from the main experiments reported in this and the following chapters reveal correlations between the anti-Stokes photon and the bulk vibrational mode of diamond — through observations of photon-phonon pair productions, as well as the manipulation of the relative phase between the anti-Stokes modes from two spatially separated diamonds prepared in a Bell state — that defy classical explanations.

Section 3.6 in this chapter is an expanded version of my published paper^[151], for which I have carried out the experimental measurements (with assistance from my co-author M. S. Sprague) as well as the accompanying data analysis (unless explicitly stated otherwise). It has been significantly re-written here to better link with the various themes I have tried to develop in this thesis, most of which were omitted from the paper due to length constraints.

3.2 Theory of Stokes/anti-Stokes production

A signature of the phonon creation and anti-Stokes readout event described above is the generation of a heralded anti-Stokes photon (its emission from the probe pulse

is accompanied by an emission of a Stokes photon from the pump pulse). In this section we extend the Schrödinger picture analysis of section 2.3.3 to describe this correlated Stokes/anti-Stokes production, providing the mechanism to measure the population, as distinct from the coherence, lifetime of the diamond optical phonon. Following the same arguments which lead us to conclude that contributions from the higher order transverse and longitudinal spatial modes are negligible given the experimental setup, we incorporate an anti-Stokes generating term to the Stokes scattering Hamiltonian of Eq. (2.23) as a pair of pump-probe pulses scatter from a diamond lattice. For effective coupling strengths g_α ($\alpha = \{S, A\}$), Stokes and anti-Stokes annihilation operators \hat{S}, \hat{A} , and phonon annihilation operator \hat{B} , the interaction Hamiltonian for the Raman process (with index $i = \{1, 2\}$ denoting the pump-probe sequence) is

$$\hat{H}_i = \hbar g_S \hat{S}_i^\dagger \hat{B}_i^\dagger + \hbar g_A \hat{A}_i^\dagger \hat{B}_i + \text{h.c.} \quad (3.1)$$

This single (phonon) mode dynamics is valid in the low power and transient regime, where the pump pulse duration is several phonon oscillatory periods. The second term in Eq. (3.1) represents the absorption of a phonon accompanied by the emission of an anti-Stokes photon, and the couplings g_α 's are functions of pump-probe detunings from the intermediate level in the Raman interactions. Since all interactions are far detuned from the conduction band, we simplify the theoretical analysis by approximating $g_S \sim g_A = g$.

We use unitary operators $\hat{U}_i = \exp[-i\hat{H}_i\tau/\hbar]$, for pulse duration τ , to calculate the evolution of the vacuum state during the pump-probe sequence [where the phonon mode decays freely, according to Eq. (2.35), between the pump-probe interactions represented by \hat{U}_1, \hat{U}_2],

$$|\psi_f\rangle = \hat{U}_2\hat{U}_1|0\rangle \quad (3.2)$$

$$\simeq \left[1 - ig\tau \left(\hat{S}_2^\dagger \hat{B}_2^\dagger + \hat{S}_1^\dagger \hat{B}_1^\dagger \right) - (g\tau)^2 \left(\hat{S}_2^\dagger \hat{B}_2^\dagger \hat{S}_1^\dagger \hat{B}_1^\dagger + \hat{A}_2^\dagger \hat{B}_2 \hat{S}_1^\dagger \hat{B}_1^\dagger + \hat{S}_2^{\dagger 2} \hat{B}_2^{\dagger 2} + \hat{A}_2^\dagger \hat{B}_2 \hat{S}_2^\dagger \hat{B}_2^\dagger + \hat{S}_1^{\dagger 2} \hat{B}_1^{\dagger 2} + \hat{A}_1^\dagger \hat{B}_1 \hat{S}_1^\dagger \hat{B}_1^\dagger \right) \right] |0\rangle. \quad (3.3)$$

The higher order $(g\tau)$ terms are negligible in the low power regime. In TCUPS the coherence time is obtained from the expectation value of the Stokes photon operator $\langle \psi_f | \hat{a}_{SD}^\dagger \hat{a}_{SD} | \psi_f \rangle$, where T is the pump-probe separation, and $\hat{a}_{SD} = (\hat{a}_{S1} + \hat{a}_{S2} e^{i\omega T})/\sqrt{2}$ is a superposition of the annihilation operators for the Raman scattered Stokes photons from the pump (\hat{a}_{S1}) and probe (\hat{a}_{S2}) pulses. It follows from Eq. (3.3) that spectral fringe visibility decay is due to the term

$$\langle \hat{a}_{SD}^\dagger \hat{a}_{SD} \rangle \propto \langle 0 | \hat{B}_1 \hat{B}_2^\dagger | 0 \rangle = e^{-\frac{T}{T_2}}, \quad (3.4)$$

whose magnitude decreases exponentially with storage time T between the pump-probe sequence, with a coherence lifetime of T_2 .

On the other hand, the phonon readout process can be detected by a pair of APDs, each capturing either a Stokes or anti-Stokes photon. The probability of obtaining a coincidence detection within a pump-probe pair, P_c , is obtained by

calculating the expectation value of the photon operators $\langle \psi_f | \hat{A}_2^\dagger \hat{A}_2 \hat{S}_1^\dagger \hat{S}_1 | \psi_f \rangle$.

$$P_c = |g\tau|^4 \langle 0 | \hat{B}_1 \hat{S}_1 \hat{B}_2^\dagger \hat{A}_2 (\hat{A}_2^\dagger \hat{A}_2 \hat{S}_1^\dagger \hat{S}_1) \hat{A}_2^\dagger \hat{B}_2 \hat{S}_1^\dagger \hat{B}_1^\dagger | 0 \rangle \quad (3.5)$$

$$= |g\tau|^4 \langle 0 | \hat{B}_1 \hat{B}_2^\dagger \hat{B}_2 \hat{B}_1^\dagger | 0 \rangle \quad (3.6)$$

In evaluating Eq. (3.5) we have used the bosonic commutation relations of the photonic and phononic operators \hat{S}_i , \hat{A}_i and \hat{B}_i such that, for example, $[\hat{A}_i, \hat{A}_i^\dagger] = \mathbb{1}$. The term containing the phonon operators on the Right-Hand Side (RHS) of Eq. (3.6) also decays exponentially with a time constant T_1 (known as the population lifetime in the literature), in general different from the T_2 decay constant in Eq. (3.4) — as will be shown in the following section.

3.3 Population and coherence lifetimes

Phonon decay can be modelled as a 2 level system coupled to the environment, and the master equation in Lindblad form^[152] describes the evolution of a quantum system, $\hat{\rho}_{sys}$, coupled to a thermal bath. It is given by:

$$\frac{d\hat{\rho}_{sys}}{dt} = -\frac{i}{\hbar} [\hat{\mathcal{H}}, \hat{\rho}_{sys}] + \sum_{\nu} \left\{ \hat{L}_{\nu} \hat{\rho}_{sys} \hat{L}_{\nu}^\dagger - \frac{1}{2} \hat{L}_{\nu}^\dagger \hat{L}_{\nu} \hat{\rho}_{sys} - \frac{1}{2} \hat{\rho}_{sys} \hat{L}_{\nu}^\dagger \hat{L}_{\nu} \right\}. \quad (3.7)$$

In the absence of coupling to the environment, the first term on the RHS of Eq. (3.7) describes the unitary time evolution of $\hat{\rho}_{sys}$ under the system Hamiltonian $\hat{\mathcal{H}}$. Coupling to the environment gives rise to the summation terms, and $\{\hat{L}_{\nu}\}$ is a set of

jump operators representing the different effects of this coupling on $\hat{\rho}_{\text{sys}}$.

We can use Eq. (3.7) to show the relationship between T_1 and T_2 in the presence of population and coherence decays. Let $\{|s\rangle, |g\rangle\} \equiv$ the excited phonon and ground states respectively, and state density elements written as $\hat{\rho}_{ij} \equiv \langle i|\hat{\rho}_{\text{sys}}|j\rangle$, where $\{i, j\} \in \{s, g\}$. The free evolution of phonon is given by $\hat{\mathcal{H}} = \omega_{gs}|s\rangle\langle s|$ for a phonon energy of $\omega_{gs} = \omega_{\text{ph}}$, and population decay process is given by $\hat{L}_1 = \sqrt{\Gamma_1}|g\rangle\langle s|$, where $\Gamma_1 = 1/T_1$. We also include the effect of phase jumps by the operator $\hat{L}_2 = \sqrt{\Gamma^*}|s\rangle\langle s|$ and find that the phonon population and coherence evolutions are governed by, respectively,

$$\frac{d\rho_{ss}}{dt} = -\Gamma_1\rho_{ss} \quad (3.8a)$$

$$\frac{d\rho_{sg}}{dt} = -i\omega_{gs} - \frac{\Gamma_1}{2}\rho_{sg} - \frac{\Gamma^*}{2}\rho_{sg}. \quad (3.8b)$$

The solutions of Eq. (3.8) are $\rho_{ss}(t) = \rho(0)e^{-t/T_1}$; $\rho_{sg}(t) = \rho_{sg}(0)e^{-t/T_2}$, and the relation

$$\frac{2}{T_2} = \frac{1}{T_1} + \frac{1}{\gamma}, \quad (3.9)$$

where $\gamma = 1/\Gamma^*$, the pure dephasing time, follows. T_1 and T_2 are referred to as the population and coherence lifetimes in the literature respectively. In the absence of any phase jumps, the Raman linewidth is purely lifetime broadened, such that $\gamma = \infty$, and $T_2 = 2T_1$. Conversely, loss of phonon phase coherence due to \hat{L}_2 process shortens T_2 , and $T_2 < 2T_1$. To see how these two lifetimes are related to the TCUPS and heralded anti-Stokes measurements, we first note that by equating $|s\rangle = \hat{B}_1^\dagger|0\rangle$,

the LHS of Eq. (3.4) can alternatively be written as $\text{Tr}\{\hat{B}_2^\dagger \hat{\rho}_{sys}(T)\}$. TCUPS is therefore a measurement of the ρ_{sg} element in the density of state $\hat{\rho}_{sys}$ (associated with T_2). In contrast, the term on the RHS of Eq. (3.6) in the heralded anti-Stokes detection can be expressed as $|g\tau|^4 \text{Tr}\{\hat{B}_2^\dagger \hat{B}_2 \hat{\rho}_{sys}(T)\}$, thus only the diagonal rather than the off-diagonal element of $\hat{\rho}_{sys}$ is measured here (associated with T_1). Recent spectroscopic studies performed on optical phonon lifetimes suggest, for example, that $T_2/T_1 \sim 0.1$ in graphene and graphite^[153].

3.4 Anti-Stokes polarisation selection rule

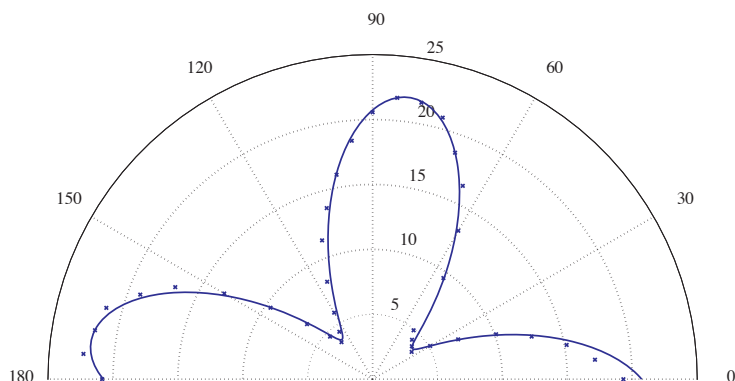


Figure 3.1 Measured intensity (radial direction, in arbitrary units) of anti-Stokes light orthogonally polarised to the pump as the diamond is rotated through 180° (in angular direction).

Anti-stokes scattering is subject to the same symmetry constraints as Stokes scattering. As in section 2.2.3, we focus H-polarised pump into a diamond sample (Fig. 2.5), and measure the intensity of V-polarised anti-Stokes light as the diamond sample is rotated around the axis of the pump propagation. A polar plot of the

intensity as a function of diamond rotation (Fig. 3.1) shows, unsurprisingly, the same 4-fold rotationally symmetric pattern seen in Fig. 2.6 for the Stokes light. Each data point represents a measurement made over 1 minute and the dark count of the APD has been subtracted from the plotted values. The maxima intensities in Fig. 3.1 should be centred on 0° , 90° , 180° in the ideal optical geometry. The angular offset indicates that the diamond axis has been aligned at an angle with respect to its mount — this has been corrected for in subsequent measurements.

Due to the low thermal occupancy of diamond optical phonon, which is why the excitation has been identified as a promising practical resource in the first place, the intensity of the scattered anti-Stokes beam is around three orders of magnitude lower than the Stokes beam. Thus the choice of spectral filters is critical to ensure that the anti-Stokes signal is measured accurately. Semrock dielectric filters are found to have the necessary transmissive properties without introducing significant levels of extra fluorescence noise (in contrast to alternative brand filters) to single photon level measurements — the extinction ratio of the pump is estimated to be $\sim 10^{-18}$ from the manufacturer's specifications. Still the ratio of the maximum to minimum intensities in Fig. 3.1 is found to be ~ 4.6 from curve fitting, and significantly lower than the equivalent ratio for Stokes light, since contributions from the remaining filter and diamond fluorescences form a larger fraction of the scattered anti-Stokes intensity than to the Stokes intensity.

3.5 Raman coupling strength

3.5.1 Measurement

Ultimately, a useful quantum memory must be able to store a single excitation, and the theoretical analysis in this thesis has been developed on the assumption that the effective Raman coupling for the Stokes and anti-Stokes fields is small, such that $|gt| \ll 1$ (approximating $g_S \approx g_A = g$) — in other words, in the spontaneous Raman scattering regime. To fully test the transition between that and the stimulated regime, I measured the scattered Stokes and anti-Stokes intensities using pump pulses from an oscillator as well as an amplifier. The oscillator is the same Coherent Mira system used in section 2, with the Stokes and anti-Stokes light coupled into separate SMFs and detected by APDs. For the second part of the measurement, the Mira is used to seed a Coherent RegA system (regenerative amplifier), generating a train of 80 fs at 250 kHz repetition rate. Typical pulse energies of the RegA system is two orders of magnitudes greater than those from Mira, producing brighter Raman signals. As a result, for ease of experimental setup, I detected the Raman signals using the same free space coupled spectrometer and cooled CCD camera in section 2. To increase its sensitivity, I utilised the hardware-binning mode of the camera whereby multiple pixels of the CCD sensing element detect signals collectively.

Figure 3.2a shows the scaling of Stokes and anti-Stokes intensities with oscillator pulse energy, which is close to the linear growth as expected from spontaneously sourced Raman signals. Each data point represents the number of counts registered

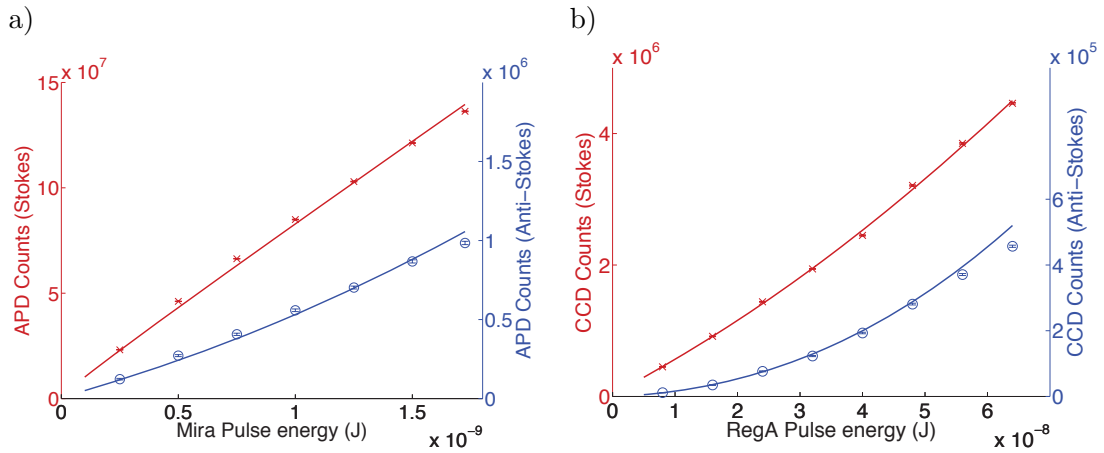


Figure 3.2 Measured Stokes (red crosses) and anti-Stokes (blue circles) intensities as a function of pump pulse energy. Calculated signal intensities [see Eq. (3.12) and the accompanying text] have been re-scaled and drawn as the solid fitted lines on the plots. An oscillator pumps the diamond in a) and the signals are measured on APDs, whereas the signals generated from an amplified pulse are measured by a cooled CCD in b).

by an APD within a minute. In contrast, the power scaling of signal intensities in Fig. 3.2b is reminiscent of exponential growth due to stimulated scattering. Here, to measure the signal intensities, a hardware binning function of the CCD camera has been utilised in which all of the accumulated charges within several pixels of the CCD are jointly transferred into the built-in A/D convertor within the camera for signal readout at the end of exposure period. Effectively, a user-defined collection of pixels act as a super-pixel, providing a straightforward way of increasing the signal-to-noise ratio, at the cost of reduced spatial and spectral resolution as well as decreased dynamic range of detection. Each data point in Fig. 3.2b represents a measurement spanning 30 s, and the hardware binning capability enables accurate signal acquisitions without the need to engage the electron multiplying gain mode of

the camera, which minimises noise contribution from the A/D conversion process, but amplifies stray photon noise.

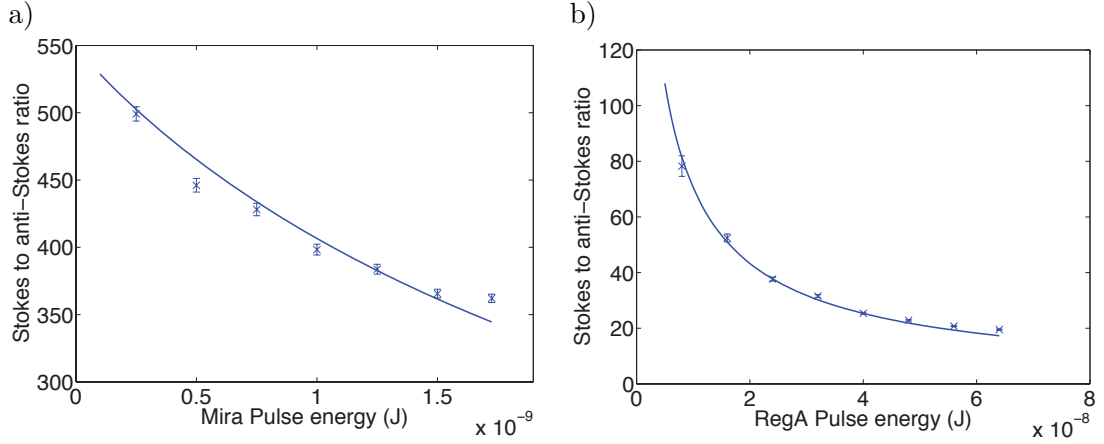


Figure 3.3 The Stokes to anti-Stokes intensity ratios from Fig. 3.2 are displayed as functions of a) oscillator and b) amplifier pulse energy. The fitted lines are obtained from re-scaling theoretical calculations and the errors on each point are calculated assuming Poissonian errors on the measured data.

3.5.2 Numerical model

To model the power scaling of the Raman signals, I wrote a script to calculate the temporal evolution of the joint Stokes/anti-Stokes/phonon state density $\hat{\rho}_{S,A,B}(t)$ (where the subscripts represent the Stokes, anti-Stokes and phonon modes respectively) using the Raman Hamiltonian in Eq. (3.1), where

$$\hat{\rho}_{S,A,B}(t) = e^{-i\hat{H}t} \hat{\rho}_{S,A,B}(0) e^{i\hat{H}t}. \quad (3.10)$$

The Stokes annihilation operator, for example, is implemented as a matrix of the form

$$\hat{S} = \begin{pmatrix} 0 & 1 & & & & \\ & 0 & \sqrt{2} & & & \\ & & \ddots & \ddots & & \\ & & & 0 & \sqrt{n_s} & \\ & & & & 0 & \end{pmatrix} \quad (3.11)$$

in the photon number basis, where n_s is the maximum Stokes photon number included within the model. The phonon initially is in a mixed state of the form $\hat{\rho}_{S,A,B}(0) = |0\rangle_S\langle 0| \otimes |0\rangle_A\langle 0| \otimes (p_n \sum_n |n\rangle_B\langle n|)$, and the Boltzmann distribution is used here to approximate the Bose-Einstein statistics, which describes ensembles of indistinguishable bosons such as the phonon, to evaluate the probabilities p_n 's of finding n phonons in the ensemble. This approximation is valid as long as the mean number of phonons in the ensemble ($\langle n \rangle \ll 1$, as evidenced by the low anti-Stokes scattering rate measured) is much lower than the number of degenerate phonon modes^[154]. In the 1D approximation, the degeneracy is lower-bounded by the ratio of the phonon wave vector bandwidth ΔK ($\sim 2 \times 10^5 \text{ m}^{-1}$, as mentioned in chapter 2) to the spacing between adjacent phonon modes in wave vector space, $\delta K = 2\pi/L \sim 2 \times 10^4 \text{ m}^{-1}$ (L is the length of the diamond sample) — in our case, $\langle n \rangle \ll \Delta K/\delta K$, and therefore it is highly unlikely for multiple phonons to occupy the same state, obviating the need for Bose-Einstein statistics. To obtain the reduced state density of the Stokes mode $\hat{\rho}_S(t)$, for instance, I imple-

mented a partial trace procedure with the matrix $\hat{M}_{k,l} = \mathbb{1}_S \otimes |k\rangle_A \otimes |l\rangle_B$, such that $\hat{\rho}_S(t) = \sum_{k,l} \hat{M}_{k,l}^\dagger \hat{\rho}_{S,A,B}(t) \hat{M}_{k,l}$. The probability of obtaining a Stokes photon, P_S , can then be calculated as a function of the Raman coupling parameter $P_S(gt)$, as

$$P_S(gt) = \text{Tr}\{\hat{S}^\dagger \hat{S} \hat{\rho}_S\} \quad (3.12)$$

— anti-Stokes probability $P_A(gt)$ can be calculated likewise.

Equating the measured signal intensities in Fig. 3.2 with the ‘true’ intensities emitted from the diamond would require thorough characterisation of detection and coupling efficiencies. Instead, I used the measured intensities to calculate the Stokes to anti-Stokes ratio P_S/P_A in Fig. 3.3, taking into account of the differential responses of the detectors at the Stokes and anti-Stokes wavelengths. Fitted onto the data is the theoretically calculated function $\frac{P_S}{P_A}(gt = \sqrt{\beta \varepsilon_p})$, where ε_p is the pump pulse energy, and we have used Eq. (2.25), which states that g is proportional to the magnitude of the pump electric field. Two approximations to the parameter β are found by least squared fitting into the oscillator (a) and amplifier (b) data — $\beta = 4.6 \times 10^{-7}$ and 3.7×10^{-7} respectively. Both values for β imply that a 1 nJ pulse (typical energy for the oscillator used in the experiments within this thesis) corresponds to $|gt| \sim 0.05$, which is well within the spontaneous scattering regime.

The Hamiltonian in Eq. (3.1) assumes the operators can operate in an infinite dimensional Hilbert space. This is obviously impossible to model with a mere classical computer, and for the numerical modelling here, I have included 24 dimensions

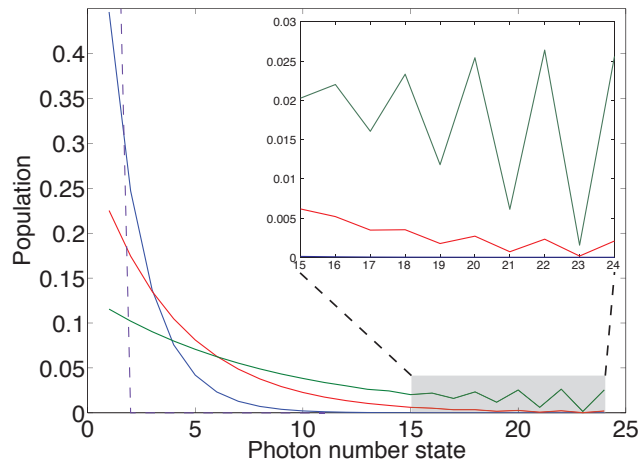


Figure 3.4 Population of Stokes number states from numerical modelling. Mean number of Stokes photon increases with pump pulse energy: $|gt| = 0.05$ (dotted purple), 1 (blue), 1.5 (red) and 2 (green).

in each Stokes, anti-Stokes and phonon mode (making e.g. $n_s = 23$). As the Raman coupling g increases, the finite dimension constraint would prevent accurate simulation of stimulated processes (which requires ever higher number states to be included in the model). Figure 3.4 shows the diagonal elements of the Stokes state density $\hat{\rho}_S$ for different Raman couplings g . Up to $|gt| = 1.5$, the Stokes population is well behaved, but at higher coupling strengths, e.g. $|gt| = 2$, non-physical features (the zig-zag distortions in the figure inset) become more pronounced as the mean Stokes photon number is increased. Both the oscillator and amplifier scatter from the diamond with a coupling strength $|gt| < 1$, therefore the chosen n_s in this simulation is large enough to avoid these non-physical artefacts, and the fitted curves in Fig. 3.3 are likely to be reasonably accurate representations of the true Stokes/anti-Stokes ratio.

3.6 Experimental demonstration of nonclassical motion in bulk diamond

For several centuries, Newton's theories of force and motion have proven to be highly adept at describing the behaviours of every day object, until the experiments of the early twentieth century reveal phenomena in the atomic and sub-atomic world that defy classical predictions. A range of theories have since been developed, which, together, form a framework that is commonly referred to as quantum mechanics. The concepts of wave function amplitudes, quantum superpositions and entanglements etc. have been remarkably successful for the understanding of many of these previously unexplainable phenomena. However, standard quantum mechanics is agnostic to the size of the system, and the question of why these exotic quantum features are not found in the macroscopic world is an active area of research^[155,156], although a broader consensus holds that thermalization with a classical environment necessarily destroys coherence^[157]. Indeed, by carefully controlling the coupling to the environment, quantum features can in principle be demonstrated with macroscopic opto-mechanical resonators that are cooled to the ground state^[158].

Due to the stiff lattice of diamond, its vibrational modes are particularly energetic, thus the probability of having a thermally initiated optical phonon at room temperature and pressure is low. At the same time, it is far from any electronic transitions — diamond phonon is therefore naturally well isolated from the environment in ambient conditions and obviates the need for the technically challenging

state preparations required in opto-mechanical resonator experiments. Furthermore, there are already proven, working bulk diamond waveguides/cavity structures^[102], alongside proven abilities of interfacing with ultrafast pulses — making a diamond based THz micro-photonics device an intriguing proposal^[40]. Therefore, the observation of non-classical dynamics in bulk diamond is a matter of both scientific and technological interest.

3.6.1 Cauchy-Schwarz inequality and quantumness

The arrival of quantum theory forced the re-examination of many fundamental concepts and led to the development of quantum optical theory, which was both spurred on by and led predictions to counter intuitive phenomena that are incompatible with the classical electromagnetism. Correlation measurements became the principle tools in demonstrating the classical and quantum natures of light. *Interference* observed from the mixing of two different field amplitudes and correlations observed in two different intensity fluctuations yield complementary information (quantified, respectively, by $g^{(1)}$ and $g^{(2)}$) on the light source and has practical applications, most famously in the field of astronomy, where the Michelson and Hanbury-Brown-Twiss interferometers^[159–163] are still the current tools of choice^[164].

In this experiment, a pump-probe pulse pair scatters from bulk diamond: the pump pulse spontaneously create a Stokes photon, which heralds the simultaneous generation of a phonon in the diamond, and the probe pulse annihilates the phonon to create an anti-Stokes photon. The coincident arrival of the herald (Stokes) and

readout (anti-Stokes) photons at two separate APDs signals the occurrence of the pump-probe scattering. This pump-probe scattering sequence can alternatively be viewed as an implementation of the quantum memory protocol, where the Stokes photon and phonon are generated as a correlated pair of excitations during the pump scattering, and the phase information contained in the phonon is then coherently transferred into the anti-Stokes photon during the probe scattering. As such, the anti-Stokes has *readout* the phase information that was created in the spontaneously scattered Stokes photon.

From the APD detections, I calculate the corresponding $g^{(2)}$ for the Stokes and anti-Stokes intensities and compare it with classical bounds to deduce the presence of a quantum process. The quantum memory readout interaction generates correlated Stokes/anti-Stokes photons, which is quantified by $g_{S,A}^{(2)}$ and is defined as

$$g_{S,A}^{(2)}(T) = \frac{P_{S,A}(T)}{P_S P_A}, \quad (3.13)$$

where T is the temporal separation between the pump-probe pulses. The probabilities of Stokes and anti-Stokes detections are P_S , P_A whilst the coincident detection of the two, $P_{S,A}$, depends on T . A key characteristic of classical light is that the second order cross-correlation, $g_{S,A}^{(2)}(T)$ is bounded by the Cauchy-Schwarz inequality $[g_{S,A}^{(2)}(t)]^2 \leq g_{S,S}^{(2)}(0)g_{A,A}^{(2)}(0)$, where $\{g_{S,S}^{(2)}(0), g_{A,A}^{(2)}(0)\}$ are the auto-correlations of the Stokes and anti-Stokes beam respectively. Assuming thermal statistics for both beams, the auto-correlations are given by $g_{S,S}^{(2)}(0) = g_{A,A}^{(2)}(0) = 2$ ^[165,166].

3.6.2 Pump preparation

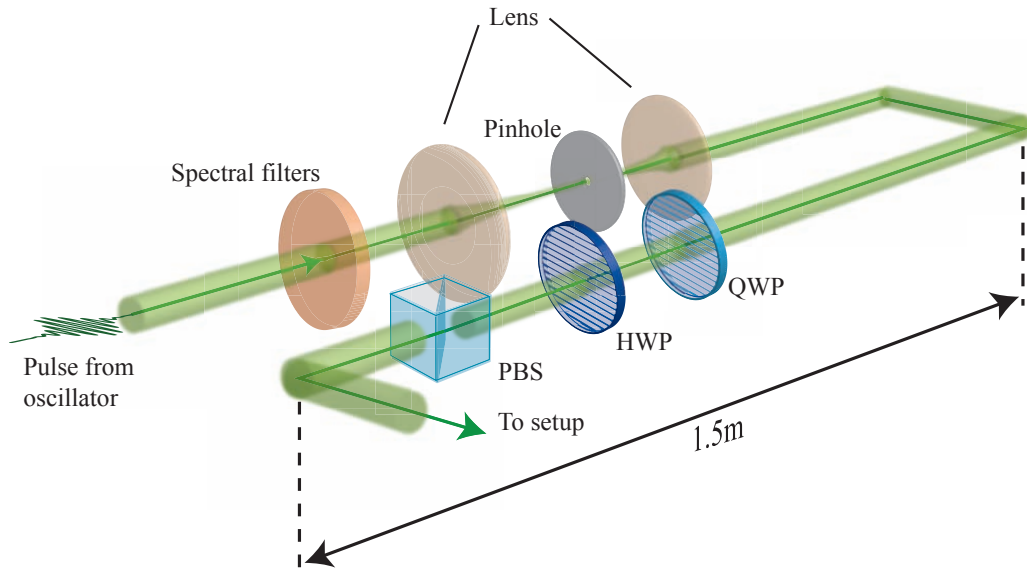


Figure 3.5 Pump pulses from a home built oscillator are filtered spectrally, spatially, as well as by polarisation to ensure there are no stray photons leaking into the detectors in the experiment.

At spontaneous scattering level of pump power, the rate of anti-Stokes production in diamond is very small, and SMFs — acting as spatial filters — are required for coupling light into the APDs to minimise contributions from thermal photon noise. Measurements suggest that the ratio of anti-Stokes to pump photons is $\sim 10^{-14}$, and the SMFs are 2 m further down the beam path from the diamond (Fig. 3.7). From these considerations, it can be seen that the spectral and spatial filtering of the pump beam is critical to the measurement.

The pump-probe pulses in this experiment are derived from a home-built Ti:sapphire oscillator, which generates a train of pulses centred at 808 nm, with ~ 18 nm

FWHM, and a repetition rate of 78 MHz. Figure 3.5 shows the 3 steps filtering process applied to the pump pulses before they are directed into the experiment. Although the Stokes and anti-Stokes wavelengths are at more than five times the measured bandwidth of the oscillator away from the pump, I found that, in the absence of spectral filtering before the diamond, there is an overwhelming amount of pump light at these wavelengths to render the Raman signals invisible to an Andor spectrometer. Therefore, the beam is first spectrally filtered by 3 bandpasses with nominal centre wavelength of 830 nm (transmission window width of 40 nm), which are then tilted with respect to the pump beam path by different degrees, such that the transmission window of each filter is centred on a different wavelength. The overall effect of the 3 filters is to introduce a lower transmission edge at 795 nm and an upper transmission edge at 820 nm. From the manufacturer's specifications, the transmission at the Stokes and anti-Stokes wavelengths is around 10^{-18} . As an asides, I found the pump leakage problem to be just as severe when testing with commercial oscillator systems (Coherent Mira and the Newport Mai-Tai), and this is therefore unlikely to be a problem that is particular to the home built oscillator.

For spatial filtering, the pump then passes through a telescope setup with a pinhole placed at the common focal plane of the two focussing lenses. Normal lens are constructed out of dispersive materials and lead to chromatic aberrations when used to focus broadband pulses (Fig. 3.6). Instead, I used two antireflective (AR) coated Thorlabs achromatic lenses of different focussing lengths, such that the outgoing beam is comparable to the spatial mode defined by the SMFs used in the experiment

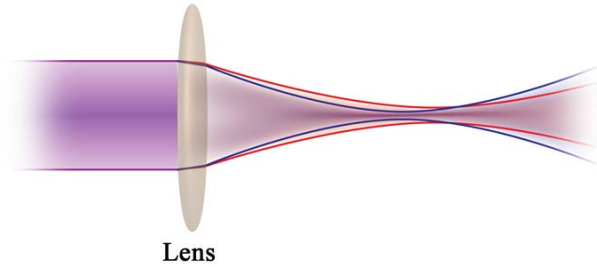


Figure 3.6 Chromatic aberration with a normally dispersive focussing lens. The red component of the incoming broadband source is focussed further away from the lens than the blue component of the incident light.

(around $2 \mu\text{m}$ in width). The pinhole is $15 \mu\text{m}$ in diameter, chosen to be around twice the expected spot size of the focussed beam, w_0 , using the formula

$$w_0 = \frac{f\lambda}{\pi d}, \quad (3.14)$$

for focussing distance f , wavelength λ and incoming beam width d (assuming it is well collimated). Compared to standard dispersive lenses, the achromats led to an increase of SMF coupling efficiency of 10% for the pump beam in the experiment, while the pinhole rejects typically 15-20% of the incident pump power.

Finally, zero-order Quarter-Wave Plate (QWP) and Half-Wave Plate (HWP) compensates for any ellipticity and rotations of the pump polarisation. In conjunction with a subsequent Polarising Beamsplitter (PBS), which is useful for polarisation purification, the pump beam power transmitted into the experiment can also be controlled. The beam path through the polarisation control arm is around 1.5 m, and on a day-to-day basis, aligning the beam through 2 irises placed at either end of

the arm can greatly aid the alignment process through the rest of the setup, which consists of another 3 m of so of optical path.

3.6.3 Experimental setup

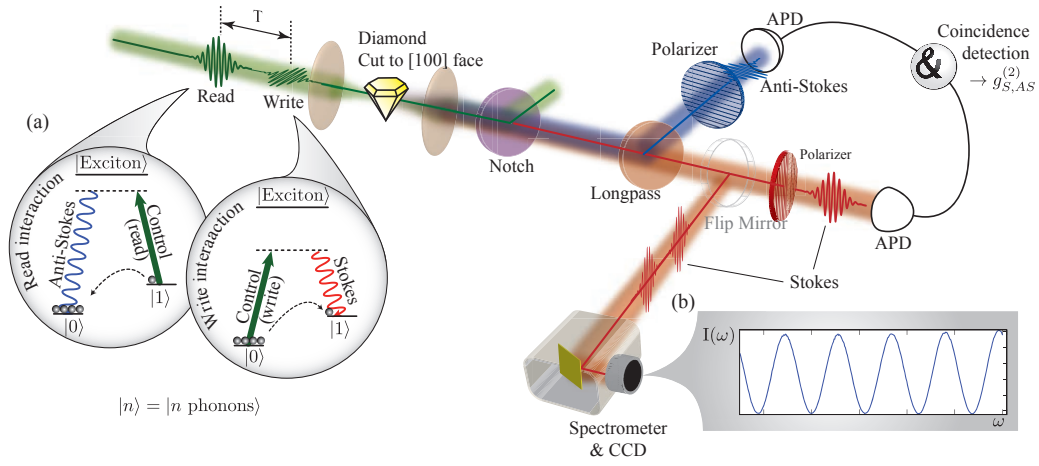


Figure 3.7 Raman quantum memory and decoherence measurement in diamond. A strong write pulse simultaneously creates a Stokes photon and an optical phonon. After a delay time T , a read pulse then either scatters an additional Stokes photon (coherence measurement), or maps the phonon into an anti-Stokes pulse (quantum memory). For the coherence measurement, the read and write pulse polarisations are aligned parallel and a flip mirror directs the Stokes pulses to a photon counting spectrometer. For the quantum memory, the read pulse is cross-polarised with respect to the write pulse, enabling separate detection of the Stokes and anti-Stokes photons with Geiger-mode APDs. The Stokes anti-Stokes cross-correlation is calculated from the rate of coincident detection events. (a) Simplified diamond level structure, showing Stokes and anti-Stokes scattering processes. (b) Data showing the measured spectral interference of the Stokes scattering probes the coherence of the phonons.

From the pump preparation setup (Fig. 3.5), the pump pulse is then directed into a Mach-Zehnder interferometer with an adjustable delay (controlled by a Newport MFA-CC motorised linear translation stage) and a HWP set at 45° to the pump

polarisation in one of the arms. This results in an orthogonally polarised pump-probe pair with an adjustable temporal separation between them.

Figure 3.7 shows the layout of the main experiment. The pump-probe pulses from the interferometer are focused with a 50 mm, AR coated achromatic lens down to $\sim 600 \mu\text{m}^2$ at the surface of the diamond and the signals were collimated by an identical lens. The crystal axis is kept parallel to the plane of polarisation of the pump-probe pulses through the entire experiment. In this geometry (c.f. section 2.2.3) the Raman scattered signals (both Stokes and anti-Stokes) generated by the pump and probe are orthogonally polarised. A set of Semrock notch filters, two centred at 830 nm and one at 808 nm, all of which with 20 nm spectral width, then rejects the 808 nm light (transmission of $\sim 10^{-12}$ at the pump wavelength).

The remaining Stokes and anti-Stokes photons are split into separate spatial paths using a 785 nm shortpass filter, and they are then coupled by SMFs into single photon counting APDs operating in Geiger mode. A Field-Programmable Gate Array (FPGA) is set up, and controlled by a LabView program, to count the APD outputs and to perform coincident measurements. By placing polarisation filters in front of the fibre couplers, we can ensure that only Stokes scattered from the pump and anti-Stokes from the probe pulses were detected by the APDs. To further improve signal to noise ratio, a 900 nm longpass is placed in the Stokes path and a 740 nm bandpass (25 nm width) is placed in the anti-Stokes path, just in front of the fibre couplers.

From the FPGA I obtain the joint probability $P_{S,A}$ of detecting both a Stokes and

anti-Stokes photon in coincidence, and the ‘singles rate’ P_S (P_A), the unconditional probabilities of detecting a Stokes (anti-Stokes) photon from a pulse. Contribution from APD dark counts are subtracted from the raw unheralded counts for the evaluation of P_S/P_A — dark count rates have been monitored over a 12 hours period, compared to 10 mins recording time for signal acquisition. *Accidental coincidences* resulting from random joint detections of uncorrelated Stokes and anti-Stokes photons are subtracted from the raw coincident counts. Since less than 1% of the detected anti-Stokes result in a coincident detection, the probability of accidental coincidences P_{acc} is calculated as

$$P_{\text{acc}} = \frac{N_S N_A}{R\mathcal{T}} \quad (3.15)$$

for dark count subtracted Stokes (anti-Stokes) counts $N_S(N_A)$, repetition rate of the experiment R and total detection period \mathcal{T} .

3.6.4 Observation of Cauchy-Schwarz violation

To verify the non-classical nature of the state of the diamond crystal during storage, I evaluate the normalised cross-correlation of the Stokes and anti-Stokes fields, given by $g_{S,A}^{(2)} = P_{S,A}/P_S P_A$. To do this, a variable electronic delay T_{el} is added between the output of the anti-Stokes detecting APD and the FPGA. The pump-probe separation is kept at 1 ps, while T_{el} is varied. Classically, the cross-correlation is upper bounded by the Cauchy-Schwarz inequality^[167] $g_{S,A}^{(2)} \leq \sqrt{g_{S,S}^{(2)} g_{A,A}^{(2)}}$, where the autocorrelation functions of the Stokes and anti-Stokes fields appear on the

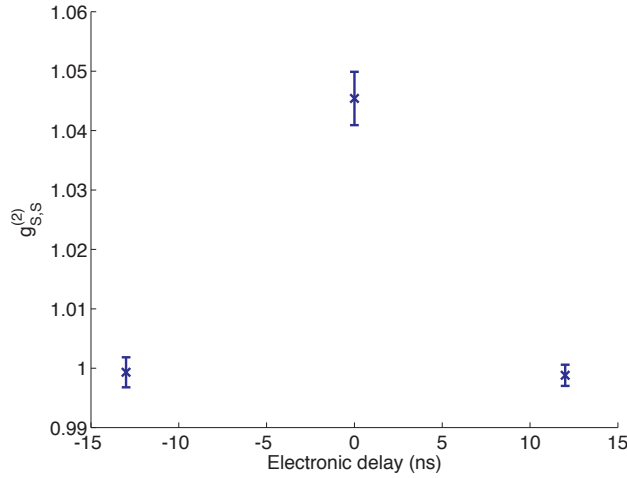


Figure 3.8 Auto-correlation function $g_{S,S}^{(2)}$. The value of $g_{S,S}^{(2)}$ at zero electronic delay is within classical bounds (< 2).

right hand side. Figure 3.8 shows that the measured values of the autocorrelation function $g_{S,S}^{(2)} < 2$ (at zero electronic delay), which is indicative of the classical photon statistics in the Stokes field when considered on its own.

The autocorrelation values for the Raman scattered fields bounded $g_{S,S}^{(2)} = g_{A,A}^{(2)} = 2$ (when the Stokes and anti-Stokes fields have thermal photon statistics), so that measured values of $g_{S,A}^{(2)}$ exceeding 2 are indicative of a true quantum memory. As shown in Fig. 3.9 (with T_{el} on the x axis), for $T = 1$ ps we observe values up to $g_{S,A}^{(2)} \approx 5.1$ [bold line, peak (a)], establishing that non-classical states are being stored and retrieved from the optical phonon modes in our diamond crystal. On the other hand, at $T_{el} = -12$ ns, anti-Stokes signals generated from a probe pulse is delayed until their arrivals at the FPGA coincide with the Stokes signals generated from the pump pulse in a subsequent pulse pair [peak (c)]. Here, Stokes and anti-Stokes signals arise from independent processes, and therefore show no more coincidences

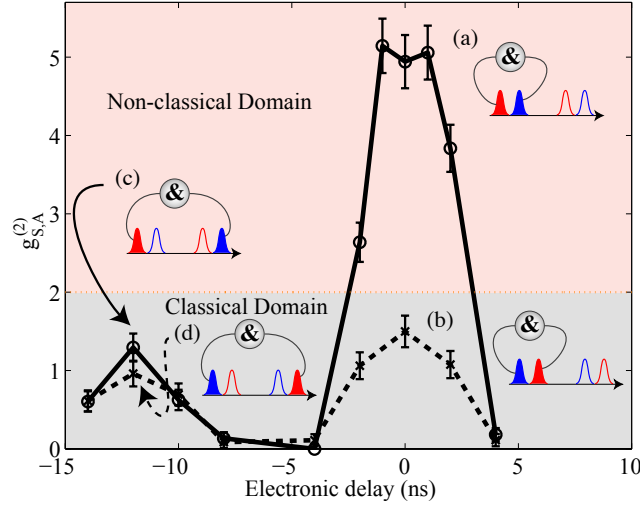


Figure 3.9 Non-classical correlations in the quantum memory. The bold line shows the measured cross correlation $g_{S,A}^{(2)}$ for $T = 1$ ps. (a) Violation of the Cauchy-Schwarz inequality $g_{S,A}^{(2)} < 2$ confirms non-classical operation. (c) The experiment is repeated at our laser repetition rate of 78 MHz, so that when the electronic delay is increased to 12 ns, accidental coincidences are measured between a write from one read-write sequence and a read from the subsequent read-write sequence, and no violations are observed. As a reference, the cross correlation is recorded when the read and write pulses are swapped (dashed line). Only accidental coincidences are observed [(b) & (d)]. The inset pulse sequences illustrate which pulses are being gated for a given electronic delay. Red pulses represent Stokes emission and blue pulses represent anti-Stokes emission.

than expected from Poissonian statistics. Each data point in Fig. 3.9 represents the total number of coincident Stokes/anti-Stokes detections in 10 minutes. The width of the peaks in Fig. 3.9 is around 5ns, which matches up with the coincidence window used in the FPGA.

As a check, I ran the measurement again, but this time, setting the polarisers in front of the fibre couplers to detect anti-Stokes generated from the pump and Stokes from the probe pulses only, shown as the dashed trace in Fig. 3.9. In this case,

all of the Raman signals are either initiated spontaneously, or from the background thermal phonon population. Thus, the peaks (b) and (d) also exhibit coincidences in line with values expected from Poissonian statistics.

The measured value of $g_{S,A}^{(2)}$ in Fig. 3.9 should be compared against the expected measured value in the presence of photon noise. In section 3.5.2, I have started to develop a model calculating the expected photon statistics of the Stokes and anti-Stokes fields individually to fit the measured power scaling behaviour. Here, the relevant quantity is the probability of joint Stokes/anti-Stokes detection $P_{S,A}$ given by

$$P_{S,A} = \text{Tr}\{\hat{S}^\dagger \hat{S} \hat{A}^\dagger \hat{A} \hat{\rho}_{S,A}\}, \quad (3.16)$$

and the reduced Stokes and anti-Stokes state $\hat{\rho}_{S,A} = \text{Tr}_B\{\hat{\rho}_{S,A,B}\}$ (for brevity, I now drop the dependence on the optical delay T , and it is to be understood that only Stokes photons from the pump and anti-Stokes from the probe pulses are detected). Chou^[168] had previously calculated an analytical expression for the cross-correlation function using Eq. (3.16), assuming both perfect readout and the ensemble initially being purely in the ground state, and found that

$$g_{S,A}^{(2)} = 1 + \frac{1}{p}, \quad (3.17)$$

where $p = \tanh |gt| / \cosh |gt|$ (for pump duration t). The behaviour in Eq (3.17) can be understood by considering that only heralded anti-Stokes are produced at low pump energies ($p \rightarrow 0$), whereas the readout anti-Stokes can stimulate emission of

other uncorrelated anti-Stokes photons at larger pump energies (therefore $g_{S,A}^{(2)} \rightarrow 1$).

To include the effects of coupling and detection noise in the APDs, I extend the reduced state $\hat{\rho}_{S,A}$ with two auxiliary photon modes $|\psi\rangle_{F_S,F_A} = |\alpha, \beta\rangle$ which are in the coherent state, and let the pump scatter from a mixed thermal phonon state as before in section 3.5.2. Given that the mean time between successive detections of Stokes photon ($\sim 1 \mu\text{s}$) is much longer than the dead time of the APDs (50 ns), shot-to-shot noise should be independent of each other and obey the Poissonian statistics given by the coherent states. The detection of a photon in the Stokes channel now corresponds to the projection operator $\hat{\Pi}_S^\dagger \hat{\Pi}_S = \hat{S}^\dagger \hat{S} + \hat{\pi}_S^\dagger \hat{\pi}_S$, where $\hat{\pi}_S$ is the annihilation operator for noise photon mode F_S , such that $\hat{\pi}_S |\alpha\rangle_{F_S} = \alpha |\alpha\rangle_{F_S}$. Likewise, detection of a photon in the anti-Stokes channel corresponds to the projection operator $\hat{\Pi}_A^\dagger \hat{\Pi}_A = \hat{A}^\dagger \hat{A} + \hat{\pi}_A^\dagger \hat{\pi}_A$, where $\hat{\pi}_A$ is the annihilation operator for the anti-Stokes noise mode F_A . The unheralded and joint detection probabilities are therefore given by

$$P_{S,A} = \text{Tr} \left\{ \hat{\Pi}_S^\dagger \hat{\Pi}_S \hat{\rho}_{S,A} \otimes |\alpha, \beta\rangle_{F_S,F_A} \langle \alpha, \beta| \right\} \quad (3.18)$$

$$P_S = \text{Tr} \left\{ \hat{\Pi}_S^\dagger \hat{\Pi}_S \hat{\rho}_S \otimes |\alpha\rangle_{F_S} \langle \alpha| \right\} \quad (3.19)$$

$$P_A = \text{Tr} \left\{ \hat{\Pi}_A^\dagger \hat{\Pi}_A \hat{\rho}_A \otimes |\beta\rangle_{F_A} \langle \beta| \right\}. \quad (3.20)$$

The expected measured cross-correlation in the presence of noise can then be evaluated as

$$g_{S,A}^{(2)} = \frac{\langle \hat{n}_{S,A} \rangle + |\alpha^2 \beta^2| + |\alpha|^2 \langle \hat{n}_A \rangle + |\beta|^2 \langle \hat{n}_S \rangle}{\left(\langle \hat{n}_S \rangle + |\alpha|^2 \right) \left(\langle \hat{n}_A \rangle + |\beta|^2 \right)}, \quad (3.21)$$

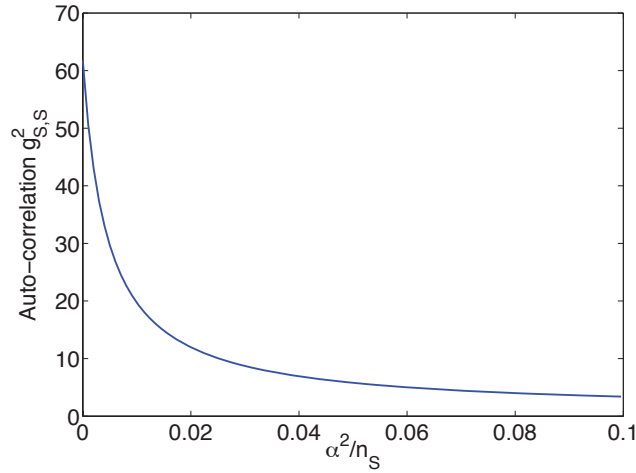


Figure 3.10 Theoretical prediction of cross-correlation function $g_{S,A}^{(2)}$ drop off in the presence of coherent state noise. The x axis represents the ratio of the mean photon number of the coherent noise state to the mean number of scattered Stokes photon per pulse.

where the number operators $\hat{n}_S = \hat{S}^\dagger \hat{S}$, $\hat{n}_A = \hat{A}^\dagger \hat{A}$ and $\hat{n}_{S,A} = \hat{S}^\dagger \hat{S} \hat{A}^\dagger \hat{A}$. In the limit of zero noise photons, $\{\alpha, \beta\} \rightarrow 0$, and Eq. (3.21) tends to the result in Eq. (3.17) — conversely, when the stray photons are dominant, the value of $g_{S,A}^{(2)}$ tends to 1. Figure 3.10 illustrates the drop off in the measured $g_{S,A}^{(2)}$ as more stray pump photons, for example, are coupled into the APDs. For the purpose of this illustration, $\beta = \alpha$, and the Raman coupling $|gt| \sim 0.1$, where the predicted $g_{S,A}^{(2)} \sim 60$ for zero photon noise — smaller than what would be predicted from Eq. (3.17) due to the phonons being in the thermal rather than ground state initially. Note that the measured $g_{S,A}^{(2)}$ drops off rapidly with small increments of stray photon noise — allowing 2% of the light detected at the Stokes APD channel to be stray noise decreases the expected $g_{S,A}^{(2)}$ from 60 to just over 10. This emphasises the need for quality spectral and spatial filtering in this experiment.

3.6.5 Quantum memory interaction

Having measured the $g^{(2)}$ and verified nonclassical motion of the diamond phonon, I then use the diamond as an on-demand optical quantum memory. The experiment is identical to the $g^{(2)}$ measurement, save for the use of an adjustable optical delay T between the pump/write pulse and the probe/read pulse instead of the fixed $T = 1$ ps used previously. As before, the polarisers in front of the fibre couplers are set to transmit Stokes scattered from the write pulse and anti-Stokes from the read pulse. The variable electronic delay, T_{el} , is now fixed to be at 0 ns, so that the various channels in the FPGA are synchronised and are detecting Stokes and anti-Stokes production from the same pump-probe pairs. The optical delay T is controlled by the motorised stage in the interferometer, and the probability $P_{\text{S,A}}$ of coincident detection of the heralding Stokes and readout anti-Stokes is measured as a function of the variable optical delay from $1 \lesssim T \lesssim 11$ ps.

Figure 3.11b plots the normalised probability $P_{\text{S,A}}$ against T . The rate of correlated Stokes/anti-Stokes production falls exponentially with T , and as explained in section 3.3, this experiment measures the population lifetime T_1 , and not the T_2 , of the diamond phonon. Comparing the intensities measured by the SMF coupled APD against a free-space coupled Andor spectrometer, and taking into account of manufacturer's specifications, I estimate the combined collection and detection efficiency η in this experiment to be around 1% for both Stokes and anti-Stokes channels. This suggests we are operating in the spontaneous scattering regime, with a scattering rate of $P_{\text{S}}/\eta \approx 0.1$ Stokes photons per pulse. This is in line with the

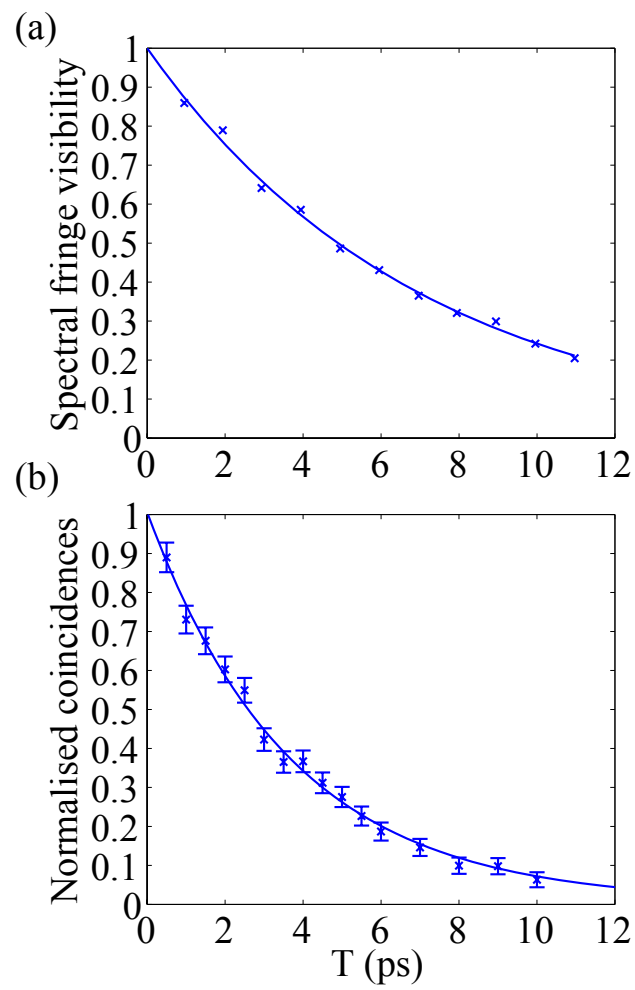


Figure 3.11 Population and coherence of non-classical phonons versus read-write delay. (a) The spectral fringe visibility of Stokes light monitors phonon coherence, with decay time T_2 . (b) Normalised $P_{S,A}$ coincidences between write Stokes and read anti-Stokes counts measuring population decay time T_1 . Solid lines are exponential fits.

power scaling of the Raman signals measured in section 3.5 — the probability that the write pulse generates more than one phonon is therefore small.

For a write/read delay of $T = 3$ ps (*i.e.* time-bandwidth product $B \gtrsim 20$), we find that $P_{S,A} \approx 9 \times 10^{-9}$. Noting the identity $P_{S,A} = P_{A|S}P_S$, where $P_{A|S}$ is the conditional probability that an anti-Stokes photon is detected, given the detection of a Stokes photon, we estimate the memory retrieval efficiency — that is, the conditional probability that an anti-Stokes photon is *emitted*, given that the memory was successfully charged — to be $\eta_{\text{ret}} = P_{A|S}/\eta \approx 0.1\%$. The retrieval and collection efficiencies could be significantly increased in an integrated photonic architecture, to which diamond is well suited^[102].

The above results show how the excitation of an optical phonon mediates the exchange of correlations between Stokes and anti-Stokes fields that are stronger than can be explained through any classical mechanism. But perhaps the spatial extent of the excitation quickly becomes localised, through the dephasing of neighbouring regions within the crystal. To test the global coherence of the optical phonons, I supplemented the quantum memory experiment with a TCUPS measurement. As detailed in section 2, TCUPS probe the coherence of the phonon mode, which for this purpose provides a diagnostic alternative to full quantum state tomography^[169]. The general layout of both experiments shares many similarities, and as shown in Fig. 3.7, I have combined the two experiments into one setup — from the phonon readout configuration, one only has to rotate one of the pump-probe pulses such that they are polarised in the same plane, and then use a flip mirror after the diamond to

by-pass the photon-counting detectors, directing the Stokes light into a spectrometer to measure the spectral fringe visibilities.

As shown in Fig. 3.11, both the Stokes spectral fringe visibility and the Stokes/anti-Stokes cross-correlation $g_{S,A}^{(2)}$ decay as the read-write delay T is increased. The coherence lifetime T_2 of the optical phonon mode determines the lifetime of the Stokes fringes, while the population lifetime T_1 determines the lifetime of the cross-correlations. The lifetimes satisfy the inequality $T_2/T_1 \leq 2$ (c.f. section 3.3), with the ratio decreasing as pure dephasing processes decohere the phonons. From repeated measurements, $T_2 \approx 6.9$ ps and $T_1 \approx 3.6$ ps, which gives a ratio $T_2/T_1 = 1.9 \approx 2$, suggesting that spectral diffusion and inhomogeneous broadening of the optical phonons can be neglected. From this we infer that the phonons remain coherent across the diamond crystal for as long as they survive. This agrees with the results of previous theoretical^[170] and experimental^[171] studies of Raman scattering in diamond, which concluded that the dominant decoherence mechanism for the optical phonons is the Klemens channel^[126], in which optical phonons decay into pairs of acoustic phonons with equal and opposite momenta due to anharmonic coupling. Indeed, calculations based on this mechanism alone predict $T_2 \approx 11$ ps^[170], which is close to our measured value. Interestingly, it is in principle possible to engineer diamond crystals with alternating layers of carbon-12 and carbon-13, by careful manipulation of the atmosphere during chemical vapour deposition^[172]. A super-lattice of these two isotopes exhibits acoustic band structure^[173], and it would be possible to engineer a diamond with gaps in the acoustic phonon dispersion relation placed appropriately

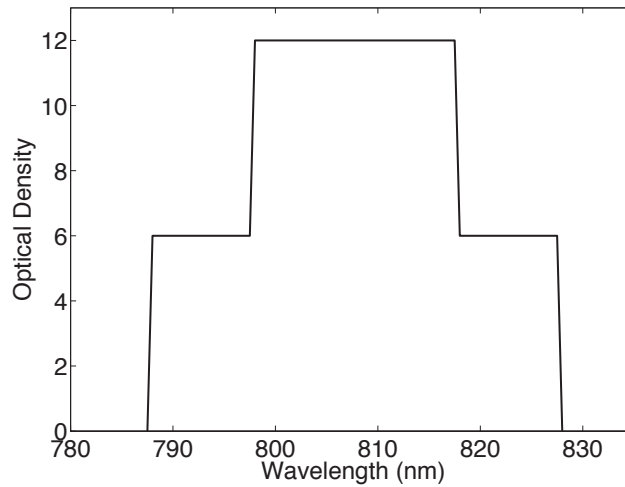


Figure 3.12 Schematic of the collective optical density of the 3 notch filters used for pump rejection after the diamond.

to forbid the Klemens channel decay. Such an approach could extend the coherence time of a diamond quantum processor, while retaining the ability to operate at room temperature. Modification of the phonon lifetime might also be achieved through controlled injection of the acoustic phonons into which the optical modes decay, as well as by changing the isotopic purity of the sample^[174,175].

3.6.6 Experimental considerations

Spectral filtering

I have already discussed in section 3.6.2 the critical role of spectral and spatial filtering. In particular, transmission at the Stokes and anti-Stokes wavelength is 10^{-18} . As well as the bandpasses before the diamond, three notch filters after the diamond reject the pump light, and Fig. 3.12 shows, schematically, the effective Optical Density (OD) of the notch filter block after angle tuning (using the Andor

spectrometer to observe pump leakage). The Optical Density is defined as

$$\text{OD} = -\log_{10} \mathcal{T}, \quad (3.22)$$

for transmission \mathcal{T} . Here, I would like to briefly discuss two of the other parameters I have considered in setting up the experiment.

Pump focussing

Spontaneous Raman scattering in a ground state ensemble creates a distributed excitation known as the Dicke state [Eq. (1.1)]. When interacting with a coherent light field, the light scatters from each atom with a position dependent phase, and the atoms in a Dicke state act cooperatively as a phase array. This mechanism is known to be responsible for phenomena such as superradiance^[176,177]. Here, this *collective enhancement* effect leads to emission of the Stokes light into a well defined spatial mode, whose transverse profile and intensity is dependent on the Fresnel number of the scattering geometry in the diamond^[138,178]. There are several approaches towards the calculations of the Stokes spatial profile, but in general, Stokes emission from an ensemble is peaked in the forward direction and broadly matches up with the pump profile. Instead of calculating the optimal focussing geometry from first principle, I have therefore opted for the trial-and-error approach and made some measurements.

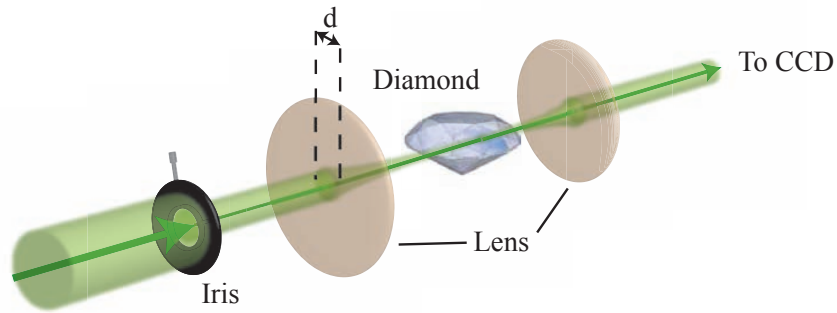


Figure 3.13 Setup to measure Stokes-to-pump ratio as a function of d .

For pump wavelength λ and crystal length L , the Fresnel number is

$$\mathcal{F} = \frac{\pi w_0^2}{\lambda L}, \quad (3.23)$$

where w_0 is the spot size of the beam, and is calculated from Eq. (3.14). Figure 3.13 shows the setup with which I measured the ratio of Stokes to pump photons as a function of Fresnel number, controlled by adjusting the width of an iris in front of the diamond. The Stokes intensity is measured on the Andor spectrometer and the pump photon number is estimated from power incident on a power meter placed after the iris. The result is plotted in Fig. 3.14, which shows that changing the Fresnel number by two orders of magnitude has only a moderate effect ($\sim 30\%$) on the Stokes-to-pump ratio, which should otherwise be a constant value in the spontaneous power limit (section 3.5). $\mathcal{F} \sim 0.1$ in both the TCUPS and quantum memory experiment.

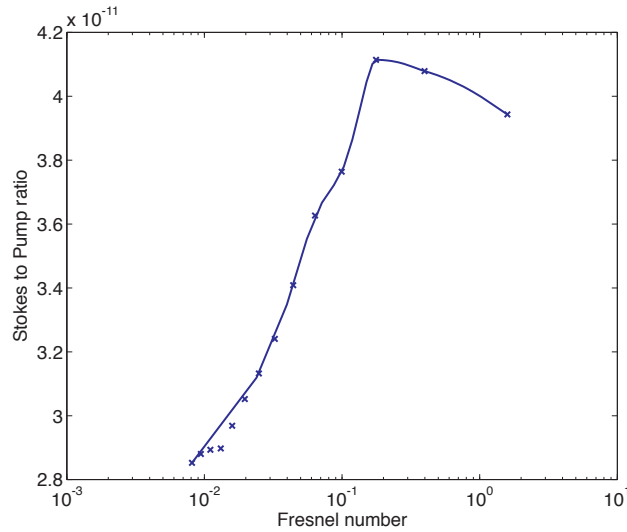


Figure 3.14 Ratio of Stokes to pump photons as a function of Fresnel power.

Fibre coupling

The main role of the SMFs is to act as spatial filters, coupling in Stokes and anti-Stokes photons that scattered off from the same phonon mode. In earlier iterations of the experiment I have used multi-mode fibres (MMFs) instead of SMFs, and found that the APDs were detecting many more photons at the Stokes and anti-Stokes wavelengths. As a result, coincidences due to the phonon readout interaction were overwhelmed by accidental coincidences due to the uncorrelated singles counts, and $g_{S,A}^{(2)}$ was only ~ 1.1 . The source of the uncorrelated photons is likely to be a mixture of stray photon noise from fluorescence, other higher order processes etc. and interaction with more than one phonon mode (the theoretical discussion in section 3.2 assumes that both Stokes and anti-Stokes couple to the same mode).

After scattering through the diamond, the pump beam is collimated to a width

of ~ 2 mm. For optimal coupling into the SMF, I used an 18.4 mm aspheric lens (Thorlabs C280TME) for Stokes collection, which gives a spot size of $2.5 \mu\text{m}$ in the focal plane from Eq. (3.14). This is comparable to the typical width of a SMF. Typical coupling efficiency of the pump beam is around 75% (without spatial filtering this number drops to $\sim 60\%$). By adjusting the width of an iris placed in front of a spectrometer, I have found the anti-Stokes beam width to be larger than the width of the C280TME aspheric lens. For the experiment, I have therefore used an achromat lens (focal length, 30 mm; optic width, 25 mm) for fibre coupling instead. Typical coupling efficiency for the pump beam is $\sim 40\%$, but it increased the coupling of (correlated) anti-Stokes into the fibre by 20% compared to the aspheric.

3.6.7 Directional emission

The Stokes pulse is detected along the write beam direction. The read pulse propagates along the same direction and so, by symmetry, the anti-Stokes emission is in the forward direction. From modelling done by M.R. Sprague, taking into account of the broadband nature of the signals, and off-axis pointing of the \mathbf{k} -vector in a Gaussian beam, it is found that the process is not perfectly phasematched: the anti-Stokes retrieval efficiency $\eta_{\text{ret}} = \alpha \eta_{\text{ret,ideal}}$ is reduced through imperfect phasematching by a factor $\alpha = \text{sinc}^2(\Delta k L/2)$, where $L = 0.5$ mm is the crystal length and Δk is the phase mismatch between the wavevector of the anti-Stokes photon and the sum of the wavevectors of the phonon and the read pulse; Δk is non-zero due to normal dispersion in the diamond. The crystal is short enough that $\alpha > 0.5$ for all frequen-

cies in the anti-Stokes pulse propagating on-axis, but α drops rapidly for off-axis scattering. Therefore the retrieved anti-Stokes photons are partially phasematched across their entire bandwidth in the forward direction, but not phasematched in other directions.

3.7 Stimulated Anti-Stokes Ultrafast Correlated Excitation Radiation Spectroscopy

Previous studies of optical phonon lifetimes include Raman spectroscopy^[86], Impulsive Stimulated Raman Spectroscopy (ISRS)^[179], as well as TCUPS, the technique explored in this thesis^[115,129]. In Raman spectroscopy, a steady state laser is Raman scattered from a diamond sample, and the linewidth of the scattered spectrum is directly measured on a spectrometer. ISRS utilises a femtosecond laser to probe the change in reflectivity of the crystal due to the induced lattice vibration, and the phonon dephasing time is extracted from the temporal evolution of the reflected intensity. TCUPS, on the other hand, measures the decay in coherence via the spectral interference pattern of the Stokes field generated from a pump-probe pulse pair (section 2). All three methods measure the phonon coherence lifetime T_2 .

The quantum memory experiment in this chapter is therefore also the first direct measurement of the T_1 lifetime of diamond in the literature. As a spectroscopic tool, it has been referred to by my research group as Stimulated Anti-Stokes Ultrafast Correlated Excitation Raman Spectroscopy (SAUCERS). As well as allow-

ing for easily interchangeable setups, by sharing similar experimental techniques to TCUPS, SAUCERS also inherit the advantages of the former experiment: namely, access to lifetime information without perturbations from hot phonons, and relatively quick measurements with readily available commercial equipments. Apart from the published results^[151] described in this chapter, I have also measured the coherence and population lifetimes of other diamond samples to test the technique's ability to distinguish the various types of diamonds.

3.7.1 Diamond samples

In this study 3 diamond samples are tested for their lifetimes. Figure 3.15 show the UV Photoluminescence (PL) images as obtained from a DiamondView instrument. The first is an electronic grade CVD sample used in the previous quantum memory readout experiment. It has < 5 p.p.b. (parts per billion) nitrogen impurity and dislocation density of around 10^{3-4} cm^{-2} . PL images (Fig. 3.15a) show sparsely populated blue lines signifying the presence of dislocations, which is known to emit a characteristic broadband light (*A-band*) centred at 435 nm ^[142,180].

The second sample is another CVD, specified by the manufacturer (Element 6) to also have a dislocation density of $< 10^4 \text{ cm}^{-2}$, but a higher nitrogen impurity of < 1 p.p.m. (parts per million). Here, the PL image (Fig. 3.15b) appears uniformly red, indicating the presence of evenly distributed nitrogen vacancy (NV^-) centers which emit at 638 nm ^[142]. The dislocation features appear when observed under a bi-refrangent microscope — see Fig. 2.12 and images in^[181].

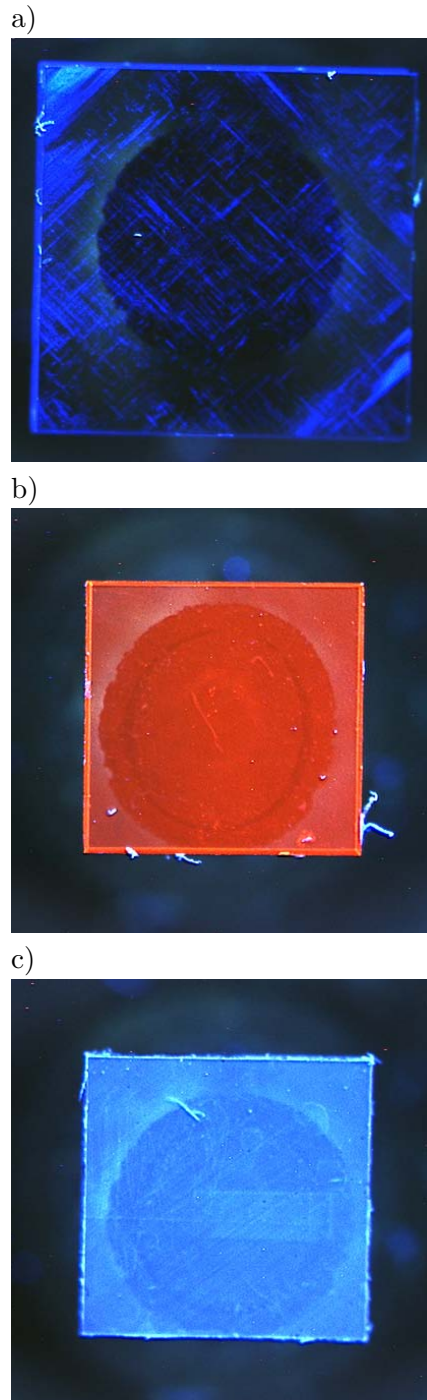


Figure 3.15 UV photoluminescence images of (a) electronic grade CVD, (b) non-electronic grade CVD and (c) natural IIa diamond.

The final sample is a natural IIa diamond with a high purity (N impurity of < 1 p.p.m., which is high for a natural sample, though short of the standards of a fabricated CVD diamond). These diamonds are known to have a very high dislocation density. Figure 3.15c shows that the A-band emission is once again the dominating feature under PL imaging. With a dislocation of 10^9 cm^{-2} , the straight line features are much more densely packed compared to sample the electronic grade CVD.

3.7.2 Measured lifetimes

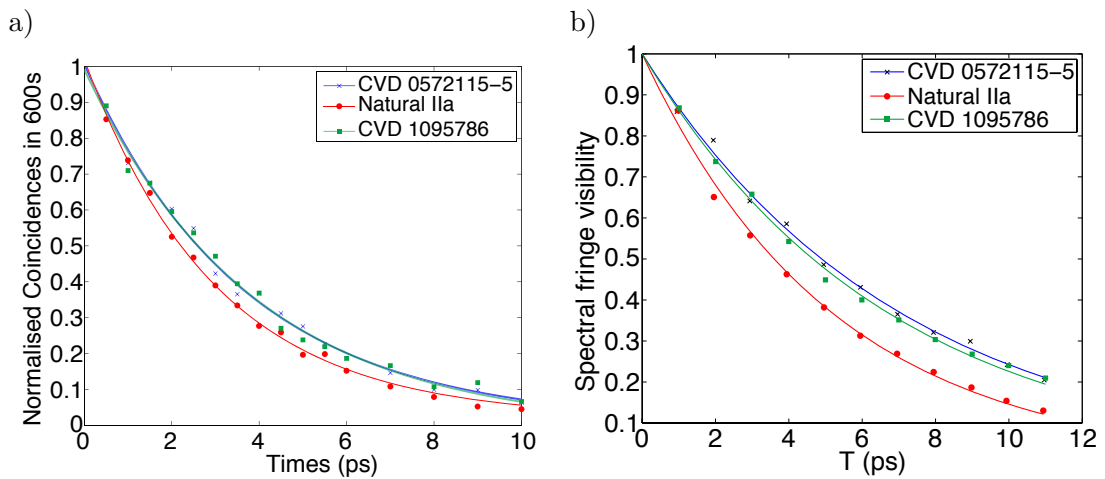


Figure 3.16 Population and coherence lifetimes of diamond phonons. a) Normalised coincidence counts between herald and read-out signals as a function of pump-probe delay in SAUCERS. The decay time is associated with population decay of diamond phonons. Each data point is obtained from 10 mins of measurement time. b) Spectral fringe visibility decay, due to phase decoherence of phonon, as observed from the spectrometer in TCUPS.

Figure 3.11a,b show one run measuring, respectively, the population and coherence lifetimes of the diamond samples. Averages and standard deviations from

Diamond	T ₂		T ₁		T ₂ /T ₁	
	Mean (ps)	Error (ps)	Mean (ps)	Error (ps)	Mean	Error
CVD-1	6.9	<0.4	3.6	0.2	1.9	0.2
CVD-2	6.6	<0.2	3.7	0.2	1.8	0.1
Natural IIa	5.2	<0.2	3.2	0.2	1.6	0.1

Table 3.1 Decoherence and population lifetimes of optical phonon. Means and errors of T₁, T₂ are obtained from 5 non-sequential measurements of each diamond sample, from which the means and errors of T₂/T₁ are calculated.

5 different measurement runs on each sample are summarised in Table 3.1. The natural IIa sample consistently has the shortest decay times in both measurements.

These measurements show $T_2/T_1 \sim 1.8$ for diamond phonons. This is consistent with a Raman line that is predominantly lifetime broadened, as modelled by the \hat{L}_1 process (c.f. section 3.3). The main mechanism responsible is the Klemens channel^[126], whereby an optical phonon decays into two acoustic phonons of equal energy. In a typical lattice structure there are multiple sources of inhomogeneous broadening, as modelled by the \hat{L}_2 process. Compared to most solid state systems, our diamond samples showed minimal inhomogeneous effects. However, the natural IIa sample, with a dislocation density several magnitudes larger than the others, has a lower T₂/T₁ ratio, and one may tentatively argue that this is due to of defects induced stress/strain in the lattice structure. Another known source of inhomogeneity is the isotopic constitution of ¹²C/¹³C in diamond^[182]. Previous experimental and theoretical studies^[174,175] have shown that, at low concentrations, a 1% rise in ¹³C density increases the linewidth by 5%. Without detailed knowledge of the diamond fabrication process and in the absence of a systematic experimental study, the pos-

sibility of a link between isotopic purity and our measured T_2/T_1 ratios cannot be entirely dismissed.

The spectrometer and CCD are important components in their differing roles as the accuracy limiting detector in both traditional Raman spectroscopy and TCUPS. Due to the finite pixel size of CCDs, typical spectral resolutions of commercially available spectrometers are of same order as Raman linewidths of diamonds, directly limiting measurement accuracy (see Fig. 2.15 for instance, which contains only half a dozen sample points within the Raman linewidth). In TCUPS the coherence time is obtained from the visibility of spectral fringes imaged on a CCD. As such, even though the spectrometer does not have sufficient resolution for the direct sampling of the Raman linewidth, accurate T_2 times could still be obtained from TCUPS through analysis of the spectrally broad features in the Stokes spectrum.

Low power pump-probe measurements are subject to thermal noise, fluorescence and higher order interactions, all of which are detrimental to signal-to-noise ratio. SAUCERS sidesteps these issues by utilising the quantum memory interaction and detection of the resulting quantum Stokes/anti-Stokes correlations. In the experiment, the number of correlated anti-Stokes generated by the readout interaction is typically 10 times larger than the contribution from the correlated anti-Stokes generated by the aforementioned noise [calculated from Eq. (3.15)]. Thus TCUPS and SAUCERS provide shot noise limited accuracy without the need of a high power pump, as in ISRS, which introduces problems associated with hot phonons creations.

Chapter 4

Diamond Entanglement

From a quantum-information perspective, the power of a quantum state lies in the existence of coherence (the off-diagonal elements in the state density) across different modes, which can easily be suppressed by coupling to an external environment, as shown theoretically in section 3.3, or even by insufficient isolation from external noise, as in section 3.6.4. Therefore, despite the irrelevance of physical size of the system (whether measured by spatial extent or by number of particles) in the theoretical formulation of quantum mechanics, in practice, demonstration of the fragile quantum effects have been mostly limited to few-particle systems^[96–98]. Experiments that demonstrate quantum features in larger systems^[106,183,184] require even larger resource overheads to achieve the necessary careful isolations from the environment, and these molecular, superconducting systems (for instance) hardly qualify as a typical object in the every day world, making the construction of scalable and practical quantum computational devices from these systems a daunting challenge

with today's technologies.

Ultrafast pulses provide a route to probing quantum coherences in large systems before they are suppressed by the environment, and quantum behaviours have recently been revealed in bio-molecules using ultrafast pump-probe techniques^[185,186]. As well as proving compatible with broadband techniques, diamond's vibrational modes are already well isolated from the ambient environment and provide the ideal workbench to showcase the same quantum features on a physical scale that is several orders of magnitudes larger than before — roughly 10^{16} atoms lie within the medium excitation for the given beam size [Eq. (3.14)]. The set of experiments in the previous chapters demonstrate that individual samples of bulk diamond are capable of exhibiting quantum behaviour at room temperature, and phonon modes are capable of preserving coherence, albeit for a short space of time. In this chapter, I describe an experiment where I verified the creation of a quantum state — the maximally entangled Bell state — that is distributed over two spatially separated pieces of bulk diamonds. This experiment is based on the well-known DLCZ scheme^[16], and combines the general procedures used in the pioneering atomic gas experiments^[56,105,106,187] with the techniques developed so far in this thesis.

The spirit of my final published paper^[188] is distributed throughout this chapter. Once again, I have partnered with M. S. Sprague for the experimental measurements and analysis. As well, contributions from my fellow co-authors are directly acknowledged within the relevant sections.

4.1 The experiment

4.1.1 Setup

A pump pulse first passes through the pump preparation step detailed in section 3.6.2 and is then rotated into a diagonally polarised pulse by use of a zero-order HWP. This is followed by a bi-refringent quartz crystal with its optical axis aligned at 45° to the pump polarisation, projecting the diagonally polarised pulse along two orthogonally polarised basis — as defined by the ‘fast’ and ‘slow’ axes of the crystal — and adds a temporal delay between between them. This splits each pulse into a cross-polarised pump-probe pair with a fixed 350 fs temporal separation. From here, the pump-probe pulses are directed into the main experiment shown in Fig. 4.1, which is an amalgamation of the two entanglement creation and verification steps shown in Fig. 1.10.

A custom made non-polarising 50:50 beamsplitter from CVI (BSNP-808-50-025) splits the pump-probe pulses into two spatial modes, and a HWP placed immediately behind one of the output ports rotates the pulses by 90° . The pump-probe pair in each arm are focussed with a 5 cm focal length achromatic lens through a 0.25 mm thick diamond plate 3 mm by 3 mm in size. An 800 nm longpass filter after each diamond separated the 900 nm Stokes and 735 nm anti-Stokes photons into two spatial modes, and the Polarising Beamsplitters PBS1, PBS2 combined separately the Stokes herald and anti-Stokes signals from each diamond into the same spatial modes. Notch filters (the same combination detailed in section 3.6.6 consisting of

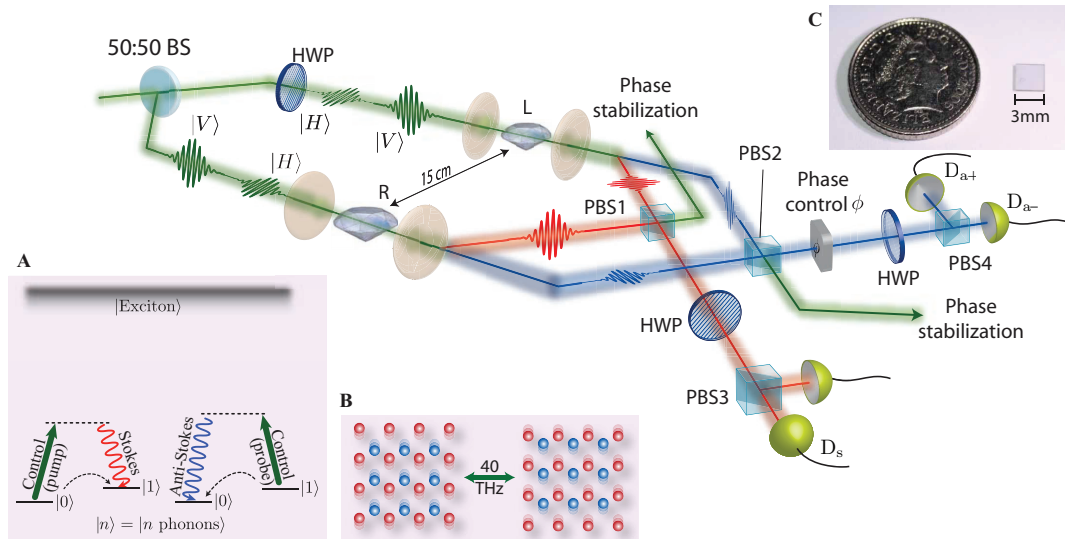


Figure 4.1 Schematic of the experimental layout for generating entanglement between two diamonds. A pump pulse is split by the beamsplitter BS and focused onto two spatially separated diamonds. Optical phonons are created by spontaneous Raman scattering, generating the orthogonally polarised heralding Stokes fields s_L , s_R [see inset (A): $|n\rangle$ represents phonon number states in diamond]. Polarisation beamsplitter PBS1 combines the spatial paths, and the half-wave plate HWP rotates and mixes the fields on PBS3, which are then directed into the single photon detector D_s . A probe pulse, with programmable delay, coherently maps the optical phonon into the orthogonally polarised anti-Stokes fields a_L , a_R [see inset (A)], which are similarly combined and mixed on PBS2, PBS4, and detected on the detectors D_{a+} , D_{a-} . The relative phase φ_a between the fields $a_{L,R}$ is controlled by a sequence of quarter- and half-wave plates (see text). Rejected pump beams from PBS1,2 are used to stabilise the interferometer. Displacements of neighboring atoms from their equilibrium positions are anti-correlated in the optical phonon mode [see inset (B)], with a vibrational period of 25 fs in diamond. Inset (C) shows one of the diamond samples, with a coin for scale.

2×830 nm and 1×808 nm filters) remove the remaining 805 nm light. The Stokes and anti-Stokes modes are then mixed with a HWP (45° to the signal polarisation planes) and PBS3, PBS4 to erase the ‘which way’ information. One output port from PBS3 (Stokes) and two output ports from PBS4 (anti-Stokes) are coupled into SMFs and detected with APDs. The coincidence detection window was 5 ns and the dead time 20 ns, compared to a pulse separation of 12 ns. Due to the low probability of excitation (10^{-3} probability of Stokes creation per pulse), the dead time of the detector can be assumed to have negligible effect on the count rates.

4.1.2 Theory

To see how entanglement is created and verified in the described sequence of events, I now use the Schrödinger picture to show the evolution of the joint state of the ensembles after each event, assuming idealised interactions where at most one excitation is created per scattering pulse — effects of higher-order interactions will be discussed after the presentation of the main result of the experiment. After the first pump pulse scatters in each arm, to first order in the Raman coupling g_{st} (pump pulse duration t), the joint Stokes and phonon state is

$$|\psi_s\rangle \approx \left[1 - ig_{st}\hat{S}^\dagger(t_s)\hat{B}^\dagger(t_s)\right] |\text{vac}\rangle, \quad (4.1)$$

using the Hamiltonian Eq. (3.1), where $|g_{st}|^2 \ll 1$ is the scattering probability and $|\text{vac}\rangle = |\text{vac}_{\text{opt}}\rangle \otimes |\text{vac}_{\text{vib}}\rangle$ is the idealised initial joint optical/vibrational vacuum state containing no photons and no phonons — I will later also numerically evaluate

the predicted results using a thermal phonon state; \hat{S} and \hat{B} are the bosonic annihilation operators for the Stokes and phonon modes, respectively, evaluated at the time t_s when the pump pulse exits the diamond. Equation (4.1) describes an entangled state consisting of optical and material modes that is analysed with the phonon readout experiment in the previous chapter. The joint state of the two diamonds is given by $|\Psi_s\rangle_{LR} = |\psi_s\rangle_L \otimes |\psi_s\rangle_R$.

After PBS1, the Stokes signal from the two diamonds are cross-polarised, and the combination of the HWP and PBS3 act as a beamsplitter for the two Stokes modes, which interfere on PBS3 with relative phase φ_s . Detection of a Stokes photon at a detector D_s behind PBS3 corresponds to application of the measurement^[189] $\hat{E} = \mathbb{1}_{\text{vib}} \otimes \langle \text{vac}_{\text{opt}} | \hat{S}(t'_s) \rangle$ (tensor product of $\mathbb{1}_{\text{vib}}$, the identity operator acting on the vibrational states with the projection operator $\langle \text{vac}_{\text{opt}} | \hat{S}(t'_s) \rangle$ acting on the photon states), where t'_s is the time at which the Stokes photon strikes D_s . Tracking the evolution of the Stokes operator through the optical setup $\hat{S}(t'_s) = \hat{S}_L(t_s) + e^{i\varphi_s} \hat{S}_R(t_s)$ (neglecting normalisation, global phases for brevity from now on and denoting operators for the two ensembles by the subscripts L,R), the ensemble state is

$$\hat{E}|\Psi_s\rangle_{LR} = [\hat{B}_L^\dagger(t_s) + e^{-i\varphi_s} \hat{B}_R^\dagger(t_s)]|\text{vac}_{\text{vib}}\rangle_{LR}, \quad (4.2)$$

where $|\text{vac}_{\text{vib}}\rangle_{LR}$ is a shorthand for $|\text{vac}_{\text{vib}}\rangle_L \otimes |\text{vac}_{\text{vib}}\rangle_R$. Equation (4.2) shows that the motion of the carbon atoms in the two diamonds are maximally entangled at t_s , containing a single phonon excitation distributed across the two crystals.

Observing a Stokes-scattered photon at D_s therefore allows us to infer the presence of entanglement between the diamonds. The purpose of the probe pulse is then to coherently transfer the entangled phonon state into the anti-Stokes mode for entanglement verification. In this case, readout occurs at $T = 350$ fs after t_s , which is short compared to the coherence lifetime of 7 ps. Phonon readout (with probability $|g_A t|^2 \ll 1$) during probe pulse scattering is equivalent of transforming the phonon operator, $\hat{B} \rightarrow \hat{B} - ig_A t \hat{A}$, so that the joint state of the diamonds and anti-Stokes modes is

$$|\Psi_a\rangle = \{\hat{B}_L^\dagger(t_a) + e^{-i\varphi_s} \hat{B}_R^\dagger(t_a) - ig_A t [\hat{A}_L^\dagger(t_a) + e^{-i\varphi_s} \hat{A}_R^\dagger(t_a)]\} |\text{vac}\rangle, \quad (4.3)$$

where \hat{A}_i is the annihilation operator for an anti-Stokes photon with the subscript $i = \{\text{L,R}\}$ denoting its operation on the left or right ensemble, and $t_a = t_s + T$. The anti-Stokes modes are combined spatially on PBS2, and interfered, with a controllable phase φ_a , by means of a HWP and PBS4. The numbers of anti-Stokes photons, N_\pm , that are detected emerging from the two output ports are given by

$$|\langle \text{vac} | \hat{A}_\pm(t'_a) | \Psi_a \rangle|^2 \propto |g_A t|^2 \sin^2[(\varphi_a + \varphi_s + \pi \pm \pi)/2] \quad (4.4)$$

where $\hat{A}_\pm(t'_a) = [\hat{A}_L(t_a) \pm e^{i\varphi_a} \hat{A}_R(t_a)]$ and t'_a is the time at which anti-Stokes photons are detected.

Equation (4.4) shows that the probability of detection of a heralded readout anti-Stokes at detectors D_{a+}, D_{a-} should vary sinusoidally with φ_a and in anti-

phase with each other. In fact, under these idealised pump-probe interactions, any finite visibility in the fringes of the intensity function $N_{\pm}(\varphi_a)$ is sufficient to prove the existence and a direct measurement of coherence between the diamonds — this is no longer true, however, when the effects of high-order interactions are considered, and in this experiment, entanglement is only verified after measurements of the rate of high-order scattering events (see later section on concurrence). To see this, let the detection of a Stokes photon at detector D_s signal that at most one phonon has been created between the two diamonds, from Eq. (4.2), the joint state density for the two phonons can be written as

$$\hat{\rho}_{B,LR} = \begin{pmatrix} p_{01} & d \\ d^* & p_{10} \end{pmatrix}, \quad (4.5)$$

where $p_{01}(p_{10})$ is the probability of creating a phonon in diamond L(R) and is estimated by the probability of detecting an anti-Stokes photon in coincidence with the heralding Stokes from each diamond; d represents the coherence between the two modes^[168]. Detecting the readout anti-Stokes field in the \hat{A}_{\pm} basis is then equivalent to applying a phase shift followed by a Hadamard/beamsplitter transformation

directly on the phonon modes

$$\begin{aligned} \hat{\rho}_{\text{B,LR}} &\rightarrow \begin{pmatrix} 1 & 1 \\ 1 & -1 \end{pmatrix} \begin{pmatrix} e^{i\varphi_a} & 0 \\ 0 & 1 \end{pmatrix} \begin{pmatrix} p_{01} & d \\ d^* & p_{10} \end{pmatrix} \begin{pmatrix} e^{i\varphi_a} & 0 \\ 0 & 1 \end{pmatrix} \begin{pmatrix} 1 & 1 \\ 1 & -1 \end{pmatrix} \\ &= \begin{pmatrix} p_{01} + p_{10} + de^{i\varphi_a} + d^*e^{-i\varphi_a} & \dots \\ \dots & p_{01} + p_{10} - de^{i\varphi_a} + d^*e^{-i\varphi_a} \end{pmatrix}, \quad (4.6) \end{aligned}$$

where the phase offset in Eq. (4.4) is absorbed into d . Intensities of the anti-Stokes signal at $D_{a\pm}$ are given by the diagonal terms in the state density (4.6), which results in fringe visibility

$$V_{\hat{\rho}} = \frac{2d}{p_{01} + p_{10}}. \quad (4.7)$$

4.2 Experimental techniques

In order to observe the signatures of entanglement in this experiment, alignment procedures had to be developed to overcome the challenges of bringing Raman signals generated independently from two diamond samples, and too weak to be measured by conventional sensors, into focus within a common volume $\sim 1 \mu\text{m}^3$ in size for fibre coupling at 2 m or so further down the beam path. Further, the signals are around 100 nm away from the pump, and therefore have significantly different beam propagation characteristics — in terms of both focussing and temporal properties. At the same time, the phases φ_s, φ_a required independent stabilisation and control, since phase fluctuation leads to suppression of the time-averaged diagonal term in the state density, as demonstrated in section 3.5.2, in which case the intrinsic visibility

[Eq. (4.7)] of the intensity fringe [Eq. (4.4)] would not be observed.

4.2.1 Alignment of translation stage

All of the experiments in this thesis contain at least one interferometer. In TCUPS and the phonon readout experiment, an unbalanced Mach-Zehnder interferometer generates an adjustable temporal delay between the pump-probe pulses, and in this entanglement experiment, one is placed in between the BS and diamond R to match the arrival times of Stokes pulses at PBS1, another between diamond R and PBS2 to synchronise the timing of the anti-Stokes pulses.

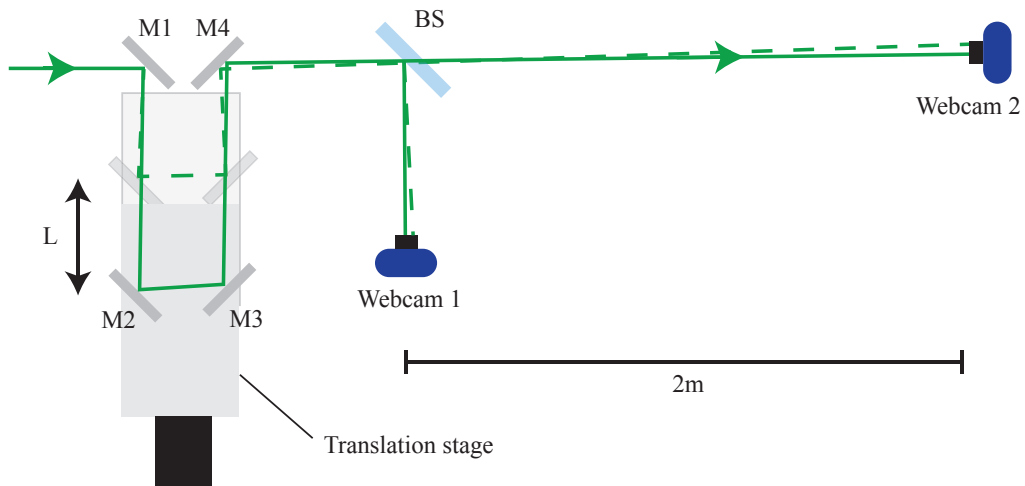


Figure 4.2 Schematic of alignment procedure for a translation stage, illustrating beam displacement (green solid and dotted lines) due to imperfectly aligned mirrors (M1-4) in the trombone line.

As shown in Fig. 4.2, a retroreflector (comprising M3,4) is mounted on the stage and used in a trombone configuration to generate a programmable optical delay. Mirrors (M1-4) need to be adjusted to produce minimum beam displacement as the

translation stage is shifted in the indicated direction. This ensures that both the pump and probe pulses address the same volume inside the diamond and scatter from the same phonon mode as well as maintaining fibre coupling efficiency for the signals further down the beam path. For the alignment process, webcam 1 is used in conjunction with a BS to monitor the beam in the near field, and webcam 2 monitors the beam displacement in the far field (around 2 m away).

Let the direction of the beam paths between $\{M1,2; M2,3; M3,4\}$ be represented by the vectors $\{\mathbf{v}_{12}; \mathbf{v}_{23}; \mathbf{v}_{34}\}$ respectively and express the outgoing beam \mathbf{v}_{out} as a function $f(\mathbf{v}_{12}, \mathbf{v}_{23}, \mathbf{v}_{34})$ of the three ‘legs’ in the trombone, then, after initial alignment of mirrors, to first approximation

$$\mathbf{v}_{\text{out}} \approx \mathbf{v}_{\text{out},0} + \left(a(L)\delta\tilde{\mathbf{v}}_{12} \cdot \frac{\partial}{\partial \mathbf{v}_{12}} + b(L)\delta\tilde{\mathbf{v}}_{23} \cdot \frac{\partial}{\partial \mathbf{v}_{23}} + c(L)\delta\tilde{\mathbf{v}}_{34} \cdot \frac{\partial}{\partial \mathbf{v}_{34}} \right) f(\mathbf{v}_{12}, \mathbf{v}_{23}, \mathbf{v}_{34}), \quad (4.8)$$

where $\mathbf{v}_{\text{out},0}$ represents the ideal outgoing, non-displacing beam and the tilde denotes a normalised version of the vector. Inspection of the geometry of the trombone would suggest that the ratios $a(L)/b(L), c(L)/b(L)$ are greatest as the translation stage is set furthest away from M1,4, and least when closest to M1,4. Therefore, the logical approach to mirror alignment is to first set the stage at either extreme of its translation and note the beam displacements on the two webcams, then, pick a ‘best guess’ of $\mathbf{v}_{\text{out},0}$ by marking out the median beam positions on both cameras. For one iteration, adjust mirror pairs M1,2 to align the beam towards the median positions on camera when the stage is set away from M1,4, and adjust M2,3 when stage is set

closest to M1,4. Repeat until the beam displacement cannot be further minimised. Then, start a second iteration, adjusting mirror pair M3,4 instead of M1,2. This alignment process assumes that the stage translates perfectly linearly. Given the physical scale of the optical setup, the stage itself should have less than 1 mrad of angular deviation or so (the Newport MFA stage chosen for the entanglement experiment has a specified deviation of $<200 \mu\text{rad}$).

At the end of the alignment¹, an SMF placed 2 m away from M4 saw a decrease of 5% in the coupling efficiency of the pump beam as the translation stage travels through its entire range of 25 mm. Further corroboration of the accuracy of the translation stage alignment can be found in the visibility drop off test in section 2.3.6.

4.2.2 Fibre coupling

The entanglement experiment setup splits the pump-probe pulses into two ensembles, and the pump focussing in the two arms must match down to μm precision in order for the Raman signals from the diamond to converge exactly at the fibre tip with roughly matched coupling efficiencies. Key to the alignment procedure is the use of a fibre coupler with a micrometer driven actuator, such as the Thorlabs MAX250D/M fibre coupling package. Since the focussing distance of the aspheric lens in the fibre coupling system is wavelength dependent, the ability to record the relative focussing positions of the pump, Stokes and anti-Stokes signals save significant time from the day-to-day alignment procedure.

¹In addition, after an unhealthy quantity of Thorlabs lab-snack.

To optimise SMF coupling, I start with the pump beam in one of the L/R arms and ensure that it is well collimated by the lens after the diamond, and couple it into all of the SMFs without the ensuing notch and spectral filters. With no further adjustments on the SMFs, the pump beam from the other arm is also coupled by adjusting only the position of collimating lens after the diamond and the mirror tilt in the subsequent beam path. Once completed, this sets both collimating lens to their final positions, and no further adjustments are required for the remainder of the experiment.

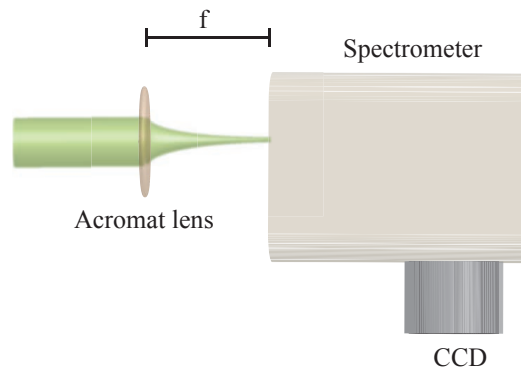


Figure 4.3 Free space coupling into Andor spectrometer.

Next, the pump beam from one of the arms is diverted and focussed into the free-space coupled Andor spectrometer instead of the SMF. Optimising the in-coupling intensity sets the optimal position for the lens (at distance ‘ f ’ from the entrance slit of the spectrometer in Fig. 4.3), and since all of the focussing optics in the experiment are achromats (except for the fibre coupling aspherics, which are not involved in this step), I can position the diamond at the focal point within the confocal setup (Fig. 4.1) by optimising the in-coupling of the Stokes signal into the spectrometer

(using suitable filters to reject the pump light). This step is repeated for the other diamond, after which the Stokes signal from the diamonds are individually coupled into the SMF, guided into the APD for detection, and the count rate is optimised with minor adjustments of the diamond position, and fibre tip position in the fibre mount.

At the conclusion of the Stokes coupling procedure, the anti-Stokes fields from both diamonds should automatically be focussing at the same point, and coupling can be optimised by adjustments of the relevant fibre tip positions. As mentioned above, the Stokes and anti-Stokes signals are separated with a 800 nm longpass filter, which I have found from experience is an easily bent piece of optic when mounting — the curvature alters the reflected beam such that the coupling efficiency at the SMF does not exceed 40% (otherwise at 70-80%). The induced astigmatism is not obvious to the eye, and it may require multiple attempts of careful mounting to solve the issue.

4.2.3 Pulse synchronisation

For interference to be observed, the Stokes and anti-Stokes from both diamonds must arrive at the detectors simultaneously. This is achieved by first taking out the bandpass filters in the pump filtering setup (Fig. 3.5), allowing pump light to leak through at the Stokes and anti-Stokes wavelengths and couple into the SMFs. This pump leakage is then detected on the spectrometer, and zero delay is found for both paths by moving the translation stages until the spectral fringe spacing increases to

infinity.

At this point, with the spectral filters re-inserted into the pump filtering setup, Stokes and anti-Stokes pulses from the two diamonds are overlapping partially in time. However, for my initial measurements, the readout anti-Stokes were observed to interfere with a low visibility, and further improvements leading to the results that will be shown later in the following sections were obtained by fine tuning the temporal overlap of the pulses. The fringe visibility was optimised by displacing the translation stages in a 2D search — it was ultimately found that the temporal overlap for the Stokes signals was perfect, but the anti-Stokes from both diamonds arrived with a relative delay of around 40 fs after performing the pump synchronisation procedure.

4.2.4 Phase stabilisation

A pair of retroreflectors mounted on piezoelectric transducers are inserted, one each, into the Stokes and anti-Stokes beam paths before PBS1,2 and they are controlled via a feedback loop to stabilise the relative phases $\varphi_{s,a}$ between the signal fields from the two arms. While most of pump is transmitted by the 800 nm longpass filters and shares common paths with the Stokes field, significant portion of the broadband pump (bandwidth ~ 20 nm) is also reflected alongside the anti-Stokes. Thus, as indicated in Fig. 4.1, pump light exiting from the unused ports of PBS1,2 is then directed into two signal acquisition setups for phase stabilisation. Within each is a polariser aligned to mix the cross-polarised pump signals from the L/R

arms, followed by a photodiode that detects the interfered signal intensity (used as the feedback signal). For the anti-Stokes path, an extra narrow bandpass filter (5nm bandwidth) is inserted after PBS2 to lengthen the pump pulses since the temporal separation (c.f. above section on pulse synchronisation) would otherwise significantly reduce the observable interference component in the intensity signal.

At each detector, the pump interference generates an intensity component $I_{\text{int}}(\phi_{\text{LR}}) \propto \sin \phi_{\text{LR}}$ that varies sinusoidally with the relative phase ϕ_{LR} between the pump pulses from the L/R arms. The intensity signal is then passed into a computer, which generates a control output signal $u(t)$ to the piezo controllers by use of a Matlab script — $u(t)$ is evaluated by

$$u(t) = K_0 e(t) + K_1 \int_0^t e(t') dt' \quad (4.9)$$

following conventional PI controller protocol. Here, the error signal $e(t)$ is the difference between the acquired intensity and the user defined set point, which is chosen to be $I_{\text{int}}(n\pi)$ where n is an integer and $\dot{I}_{\text{int}}(\phi_{\text{LR}})$ is greatest; K_0 , K_1 are proportionality constants that are increased incrementally, through a trial and error approach, just before the output signal is induced into continuous oscillations.

Fast silicon (Si) photodiodes (Thorlabs DET10A/M) were used as the detectors for the pump, which turned out to be an inconvenient choice since a time averaged signal is required to generate error signal in Eq. (4.9). Instead, the 1 ns rise time of the photodiodes means that the output signals from them are pulsed in time, due

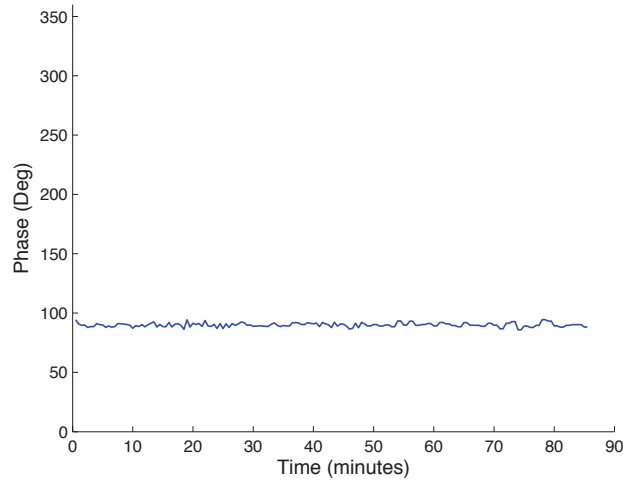


Figure 4.4 Evolution of relative pump phase ϕ_{LR} with the stabilisation feedback loop (created by M.R. Sprague) running.

to the pulsed nature of the pump itself. Data acquisition is achieved by passing the current signals from the photodiodes into a BNC connector block (National Instruments BNC-2110) that is connected to a DAQ card (National Instruments PCI-6221 M series) in the computer. To obtain a time averaged response, the BNC cable running from the photodiode is connected to the connector block through a T junction, where a high impedance ($\sim M\Omega$) resistor terminates the unused port. The resistor is thus added in parallel to the current source, acting as a lowpass filter^[190] as well as amplifying the voltage acquired by the DAQ card. Figure 4.4 shows that with the stabilisation script running, the relative phase of the pump ϕ_{LR} can be stabilised to $\sim 1.7^\circ$. Since the pump light share common paths with the Stokes and anti-Stokes signals up to PBS1,2, after which the Stokes and anti-Stokes fields from the L/R arms share common paths amongst themselves, phase stabilisation on the pump light ensures stability of φ_s, φ_a .

4.2.5 Anti-Stokes phase control

The implementation of the control loop can in principle be used to stabilise φ_a at various values within a 2π period (taking into account of the wavelength dependence in the phase of the pump and anti-Stokes signal) rather than at one particular set point. However, in the experiment I have used a more elegant solution based on an implementation of the Pancharatnam-Berry phase^[191,192], as proposed by N. Langford^[193] to step through φ_a and profile the function $N_{\pm}(\varphi_a)$.

Following the pulse synchronisation procedure, the anti-Stokes state after PBS2 is [c.f. Eq. (4.3)]

$$|\psi_a\rangle = \frac{1}{\sqrt{2}} \left(|H\rangle + e^{i\phi_a} |V\rangle \right), \quad (4.10)$$

where the cross-polarised components $|H\rangle$ (horizontal), $|V\rangle$ (vertical) represent contributions from the R, L diamonds respectively. $|\psi_a\rangle$ is a single qubit state and can be represented as a point on the Bloch sphere, and it turns out that a sequence of QWP-HWP-QWP can implement an arbitrary rotation around the z axis (running through the $|H\rangle, |V\rangle$ points).

According to Pancharatnam and Berry's theory, an arbitrary state that evolves adiabatically along a closed loop on the surface of the Bloch sphere gains a 'geometric' phase, given by the solid angle subtended by the enclosed surface. To implement a rotation around the z axis, the states $|H\rangle, |V\rangle$ (basis states of the z rotation) must also gain a phase and brought back to its original positions on the Bloch sphere after evolution by the set of wave plates. Therefore, Langford^[193] suggested the following

application of wave plates for a z rotation:

$$\hat{R}_z(\theta) = \hat{U}_{\frac{\lambda}{4}}\left(\frac{\pi}{4}\right) \hat{U}_{\frac{\lambda}{2}}\left(-\frac{\pi}{4} - \frac{\theta}{4}\right) \hat{U}_{\frac{\lambda}{4}}\left(\frac{\pi}{4}\right) \quad (4.11)$$

$$= \begin{pmatrix} e^{-i\frac{\theta}{2}} & 0 \\ 0 & e^{i\frac{\theta}{2}} \end{pmatrix}, \quad (4.12)$$

where θ is the angle to be rotated around the Bloch sphere; $\hat{U}_{\frac{\lambda}{4}}(\zeta) \left[\hat{U}_{\frac{\lambda}{2}}(\zeta) \right]$ represents rotation by an QWP (HWP), with the major axis aligned at ζ rad to the vertical.

To summarise, the ‘phase control’ in Fig. 4.1 consists of a QWP-HWP-HWP combination, with both QWP set at 45° to the anti-Stokes polarisations, and each 10° rotation of the HWP corresponds to adding 40° in phase between the anti-Stokes modes from the two arms.

4.3 Results

4.3.1 Anti-Stokes interference

Figure 4.5 shows the measured sinusoidal oscillation in the heralded anti-Stokes detections at the two detectors N_{\pm} as φ_a is varied for a set φ_s . As well as generating heralded readout anti-Stokes photons, the pump-probe process also produces uncorrelated anti-Stokes, thereby limiting the cross-correlation $g_{S,A}^{(2)}$ for the Stokes and anti-Stokes fields from a single diamond (section 3.6.4). For this entanglement experiment, these uncorrelated anti-Stokes photons limit the maximum attainable

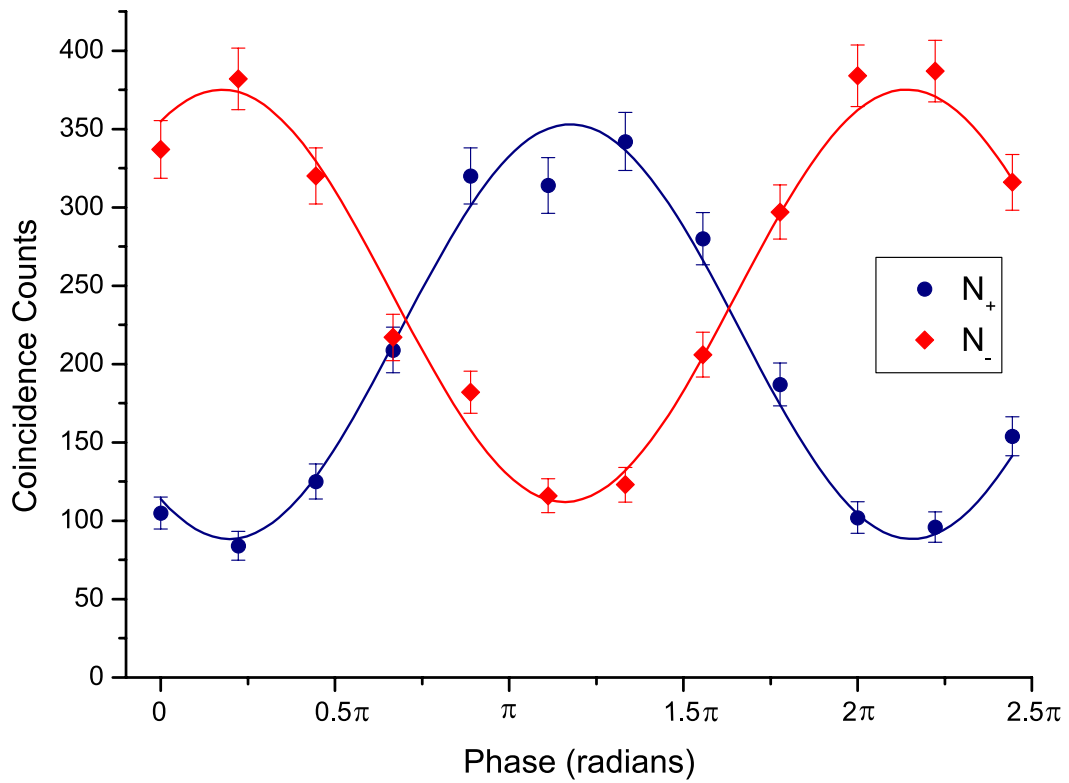


Figure 4.5 Coincidence between herald and read-out photons. The visibility is $V = (61 \pm 3)\%$ for N_+ and $V = (55 \pm 3)\%$ for N_- . The difference in visibility between the measurement sets we attribute to the different rate of accidental coincidences between the two detectors. Error bars on the plot are estimated from the standard deviation of a Poissonian process.

visibility in the N_{\pm} fringes, which can be evaluated to^[168]

$$V_{\text{ideal}} = \frac{g_{S,A}^{(2)} - 1}{g_{S,A}^{(2)} + 1} \quad (4.13)$$

for two samples with identical $g_{S,A}^{(2)}$'s and are purely in the ground states initially.

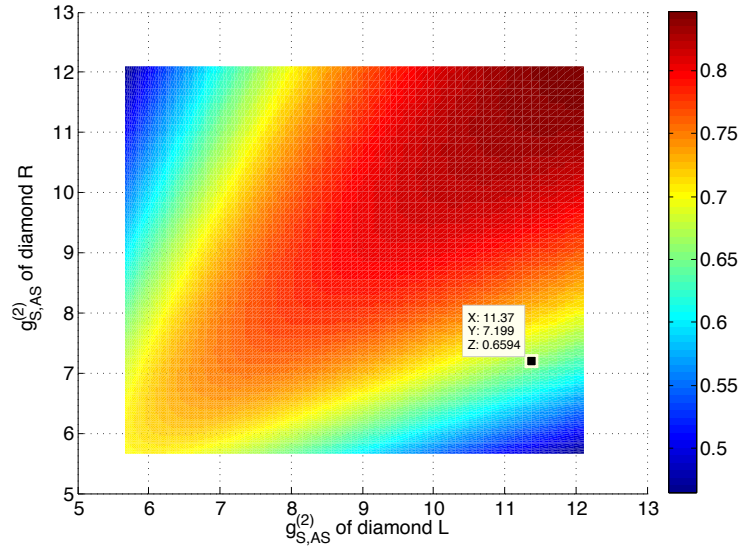


Figure 4.6 The maximum attainable visibility in the anti-Stokes intensity fringes from two diamonds with different $g_{S,A}^{(2)}$'s.

The cross-correlations $g_{S,A}^{(2)}$ for the two diamonds in this experiment were measured to be 11.4 and 7.2. To obtain the maximum achievable visibility for these two diamonds, I first evaluated the reduced Stokes and anti-Stokes state density $\hat{\rho}_{S,A}$ from the joint Raman signals and phonon state $\hat{\rho}_{S,A,B}$ using the same procedures detailed in section 3.5.2, assuming both photon fields are in the vacuum state and thermal phonon state initially. The tensor product of the reduced state with itself then forms the joint Raman signal state for the two arms $\hat{\rho}_{LR} = \hat{\rho}_{S,A} \otimes \hat{\rho}_{S,A}$ after

pump-probe scattering. Representing the detection of a Stokes photon at D_s by $\hat{S}_+^\dagger \hat{S}_+$, detection of anti-Stokes photon at $D_{a+}(D_{a-})$ by $\hat{A}_+^\dagger \hat{A}_+(\hat{A}_-^\dagger \hat{A}_-)$, and coincidence detections at $D_s, D_{a\pm}$ by $\hat{S}_+^\dagger \hat{S}_+ \hat{A}_\pm^\dagger \hat{A}_\pm$, the visibility of the intensity fringes N_\pm can be evaluated

$$V_{\text{theory}} = \frac{\langle (\hat{S}_L^\dagger \hat{S}_L + \hat{S}_L^\dagger \hat{S}_R + \hat{S}_R^\dagger \hat{S}_L + \hat{S}_R^\dagger \hat{S}_R) (\hat{A}_L^\dagger \hat{A}_R + \hat{A}_R^\dagger \hat{A}_L) \rangle}{\langle (\hat{S}_L^\dagger \hat{S}_L + \hat{S}_L^\dagger \hat{S}_R + \hat{S}_R^\dagger \hat{S}_L + \hat{S}_R^\dagger \hat{S}_R) (\hat{A}_L^\dagger \hat{A}_L + \hat{A}_R^\dagger \hat{A}_R) \rangle}. \quad (4.14)$$

Using Eq. (3.21) in the noiseless limit $\alpha = \beta = 0$, Eq. (4.14) is shown in a 2D plot as a function of $g_{S,A}^{(2)}$ for the two diamonds in Fig. 4.6. The predicted maximum visibility is evaluated to be 66% for this experiment — lower than the 75% value reported in the published account of this work^[188] due to the use of an initial thermal rather than vacuum phonon state. Within this context, the measured fringe visibility of $(61 \pm 3)\%$ (for N_+) implies that the alignment procedure developed during the course of this thesis has been successful at producing a good mode-overlap between the Raman-scattered modes interfered from the two diamonds. In addition, the effects of spontaneous emission of anti-Stokes photons, phonon decoherence, and scattering into higher order spatial modes, which would otherwise generate uncorrelated photons and limit the measured visibility, have been minimal, and corroborates with the various assumptions and arguments laid out in the thesis.

Although it has not been necessary to do so for this experiment, the effects of stray photon and fluorescence noise can be included by following the general procedure in section 3.6.4. First, augment the joint Raman signal state with noise

states $\hat{\rho}_{\text{LR}} \otimes |\alpha_{\text{L}}\beta_{\text{L}}\alpha_{\text{R}}\beta_{\text{R}}\rangle_{\text{LR}}\langle\alpha_{\text{L}}\beta_{\text{L}}\alpha_{\text{R}}\beta_{\text{R}}|$, where $\alpha_{\text{L,R}}(\beta_{\text{L,R}})$ are the coherent state amplitudes for the Stokes(anti-Stokes) modes in the L,R arms respectively. Since the noise photons from the two arms do not necessarily have good temporal overlap, they would not contribute to the interference effects and the measurement operators corresponding to these modes are $\hat{\pi}_{S_+}^\dagger \hat{\pi}_{S_+} = \frac{1}{2} \left(\hat{\pi}_{\text{SL}}^\dagger \hat{\pi}_{\text{SL}} + \hat{\pi}_{\text{SR}}^\dagger \hat{\pi}_{\text{SR}} \right)$, $\hat{\pi}_{A_+}^\dagger \hat{\pi}_{A_+} = \hat{\pi}_{A_-}^\dagger \hat{\pi}_{A_-} = \frac{1}{2} \left(\hat{\pi}_{\text{AL}}^\dagger \hat{\pi}_{\text{AL}} + \hat{\pi}_{\text{AR}}^\dagger \hat{\pi}_{\text{AR}} \right)$, where $\hat{\pi}_{S_+,L,R}(\hat{\pi}_{A_\pm,L,R})$ are the annihilation operators for the Stokes(anti-Stokes) fields at the $D_s(D_{a\pm})$ detectors, L and R arms respectively. Therefore, with the noise contribution, the expected visibility would be

$$\begin{aligned}
V_{\text{noise}} = & \left[\langle \hat{S}_+^\dagger \hat{S}_+ \left(\hat{A}_L^\dagger \hat{A}_R + \hat{A}_R^\dagger \hat{A}_L \right) \rangle + \left(|\alpha_{\text{L}}|^2 + |\alpha_{\text{R}}|^2 \right) \langle \hat{A}_L^\dagger \hat{A}_R + \hat{A}_R^\dagger \hat{A}_L \rangle \right] \\
& / \left[\langle \hat{S}_+^\dagger \hat{S}_+ \left(\hat{A}_L^\dagger \hat{A}_L + \hat{A}_R^\dagger \hat{A}_R \right) \rangle + \left(|\alpha_{\text{L}}|^2 + |\alpha_{\text{R}}|^2 \right) \langle \hat{A}_L^\dagger \hat{A}_L + \hat{A}_R^\dagger \hat{A}_R \rangle \right. \\
& \left. \left(|\beta_{\text{L}}|^2 + |\beta_{\text{R}}|^2 \right) \langle \hat{A}_L^\dagger \hat{A}_L + \hat{A}_R^\dagger \hat{A}_R \rangle + \left(|\alpha_{\text{L}}|^2 + |\alpha_{\text{R}}|^2 \right) \left(|\beta_{\text{L}}|^2 + |\beta_{\text{R}}|^2 \right) \right].
\end{aligned} \tag{4.15}$$

Equation (4.15) is highly dependent on the precise ratio of the relative amount of noise contribution at the Stokes and anti-Stokes wavelengths from the two arms. It is included here for completeness since it would only be useful with a much more thorough noise characterisation that has been done or required in this experiment.

4.3.2 Concurrence

Under ideal circumstances, the detection of a single Stokes photon at detector D_s is associated with the diamond ensemble state according to Eq. (4.2) and ensures that any finite fringe visibility signifies the presence of coherence between the diamond ensemble by Eq. (4.7). However, the APD is not a photon number resolving detector, and a detection click at D_s may very well herald the creation of a separable phonon state of form $\hat{B}_L^\dagger \hat{B}_R^\dagger |\text{vac}_{\text{vib}}\rangle_{\text{LR}}$ through a second order interaction in $|gst|$. Transforming the phonon operator $\hat{B} \rightarrow \hat{B} - ig_A t \hat{A}$ as before to represent readout, the resulting state

$$|\Psi'_a\rangle = \left(\hat{B}_L^\dagger - ig_A t \hat{A}_L^\dagger \right) \left(\hat{B}_R^\dagger - ig_A t \hat{A}_R^\dagger \right) |\text{vac}\rangle \quad (4.16)$$

is also separable and likewise generates an interference pattern when detected in the \hat{A}_\pm basis. As a result, the measured visibility in Fig. 4.5 must exceed a threshold value, V_{thresh} , to ensure that the contributions from higher-order interactions are sufficiently small compared to the single anti-Stokes interactions. Further, since the phonon-to-photon readout mapping is a local operation (acting separately on each diamond) that cannot increase entanglement^[106], the photon entanglement is a strict lower bound to the phonon entanglement.

Entanglement produces correlations between different degrees of freedoms which surpasses what is allowed by classical physics^[194], but the degree by which the classical bounds are exceeded can be quantified in various ways^[18,195]. The *entanglement*

of formation is one such measure, which aims to solve the problem by quantifying the number of maximally entangled Bell states that are needed to form an arbitrary bipartite state. Like many other quantifications of entanglement, entanglement of formation is a function requiring a non-trivial minimisation over all possible pure state decompositions of the state density. Fortunately, Wootters^[196] has obtained an explicit formula that obviates the need for the minimisation step via the quantity *concurrence* $C(\hat{\rho})$, which is given by

$$C(\hat{\rho}) = \max \{0, \lambda_1 - \lambda_2 - \lambda_3 - \lambda_4\}. \quad (4.17)$$

The set of $\{\lambda_i\}$ are the eigenvalues of the matrix $\sqrt{\sqrt{\hat{\rho}}\hat{\tilde{\rho}}\sqrt{\hat{\rho}}}$ in decreasing order, and $\hat{\tilde{\rho}} = (\hat{\sigma}_y \otimes \hat{\sigma}_y) \hat{\rho}^* (\hat{\sigma}_y \otimes \hat{\sigma}_y)$ is the spin-flipped version of the complex conjugate of the state density $\hat{\rho}$. The concurrence is zero for any separable state and increases *monotonically* towards 1 for maximally entangled state (i.e. concurrence for a set of state densities arranged in order of increasing entanglement preserves the given order).

To verify that the higher order terms are insufficient to generate the fringe visibility in Fig. 4.5, I measure the rate of two phonons scattering events (where two anti-Stokes are detected given the detection of a heralding Stokes photon) to estimate the high order term in the state density. Concurrence is then calculated from this extended density matrix, including the two phonons term, as a witness to the existence of entanglement. Let $|nm\rangle$ represents the generation of $n(m)$ anti-Stokes

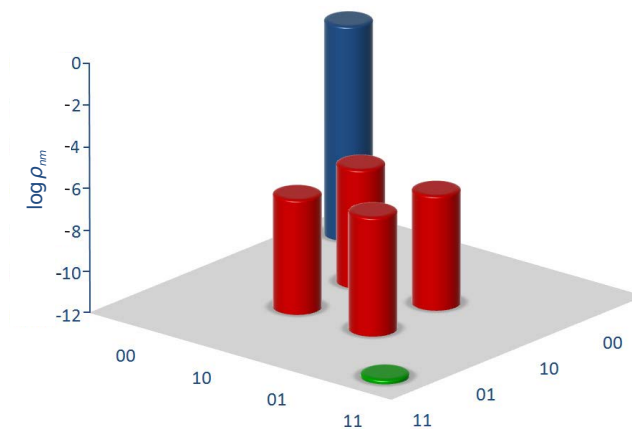


Figure 4.7 Density matrix of the heralded anti-Stokes modes. The density matrix elements are $p_{00} = 1 - 2.3 \times 10^{-5}$, $p_{01} = 1.2 \times 10^{-5}$, $p_{10} = 1.1 \times 10^{-5}$, $d = 7.0 \pm 0.3 \times 10^{-6}$, $p_{11} = 2.0 \pm 1.1 \times 10^{-11}$. The diagonal element probabilities are maximum likelihood estimates, measured with no interference between the anti-Stokes modes of the two diamonds. No corrections for background counts, accidental coincidences, or system inefficiencies were made in these measurements. The higher order term is inherent to the process of spontaneous emission, and the vacuum component is related to the anti-Stokes readout, collection and detector efficiencies.

photons in the L(R) diamonds, conditioned on detection of a Stokes photon at D_s , then, in this number basis, the concurrence for a state density with the form given in Fig. 4.7 is^[106,196]

$$C = 2 \max(|d| - \sqrt{p_{00}p_{11}}, 0). \quad (4.18)$$

Here, the coherence d is obtained from the measured visibility using Eq. (4.7), and p_{nm} 's are the diagonal terms in the density matrix (for the $|nm\rangle$ states). p_{01}, p_{10} are estimated separately by the rate of heralded anti-Stokes production in each diamond; $p_{00} \simeq 1 - p_{01} - p_{10}$ is the probability of no readout interaction given the detection of a Stokes photon; and p_{11} is the probability of detecting a three-fold coincidence from detectors D_s, D_{a+}, D_{a-} with unbalanced path lengths between the

L,R arms in the experiment to prevent the anti-Stokes modes from interfering (which may lead to photon bunching at PBS4, such that two-fold coincidence is generated even though three photons are produced). Note that only 6 out of the possible 16 elements in the density matrix in Fig. 4.7 are measured. Non-zero values in any other elements would only increase the amount of coherence in the state, and therefore the concurrence^[106]. As such, the concurrence derived from Fig. 4.7 is a strict lower bound of the true concurrence for the joint diamond state.

From measurements, the concurrence values are estimated to be $(5.2 \pm 2.6) \times 10^{-6}$ for the N_+ fringe and $(3.8 \pm 2.6) \times 10^{-6}$ for the N_- fringe using the raw coincident counts. Subtracting accidental coincidences due to the dark counts of the APD detectors and Stokes detections, the concurrences for the N_+ , N_- fringes are $(5.6 \pm 2.6) \times 10^{-6}$, $(4.9 \pm 2.6) \times 10^{-6}$ respectively, which are on the order of the maximum value of the concurrence (for $V = 1$, and $p_{11} = 0$, $C_{\max} = p_{01} + p_{10} = 2.3 \times 10^{-5}$). The maximum value is limited by coupling, detector and the anti-Stokes readout efficiency.

The frequency of triple coincidence occurrences, as indicated in Fig. 4.7, is exceedingly rare — a total of only 3 triple coincidences (with no background subtraction) were detected over 1.9×10^{14} runs of the experiment². Viewed alternatively, given the measured probabilities $\{p_{nm}$'s}, this triple coincident probability sets a ‘threshold visibility’ value of $V_{\text{thresh}} \approx 38.9\%$ [from Eqs. (4.7), (4.18)], which is indeed surpassed by the measured visibility — this is consistent with the requirement

²This is over three times the value of US national debt in US\$, as of April 2012.

for positive concurrence.

With such a low triple coincidence value, the calculation of concurrence and the accompanying confidence intervals is a non-trivial problem tackled by M.R. Sprague, my co-first author in the associated paper^[188], and the methodology used is outlined here for reference. In Poissonian statistics, the probability of observing X events given a distribution mean value μ is

$$P(X|\mu) = \frac{\mu^X e^{-\mu}}{X!}. \quad (4.19)$$

From Eq. (4.18), for concurrence to be zero and approximating $p_{00} \sim 1$, the expected number of triple detections μ_0 should be $\mu_0 > d^2 N p_s = 9.1 \pm 0.9$ (assuming Poissonian statistics on the APD counts), where N is the number of experiments and $p_s \sim 1 \times 10^{-3}$ is the probability of generating a Stokes photon. To confirm the existence of entanglement, in the *frequentist* approach to the problem, one has to calculate the confidence level \mathcal{C} , defined as the fraction of experiments whose ‘true’ Poissonian parameter μ lies between $0 \leq \mu \leq \mu_0$ ^[197], which is given by

$$\mathcal{C} = \int_0^{\mu_0} P(X = 3|\mu) d\mu. \quad (4.20)$$

The confidence level for N_+ and N_- are $(98 \pm 1)\%$ and $(94 \pm 2)\%$ respectively using the visibilities obtained from the raw coincidence counts and the fitted values for d . The corresponding figures for background subtracted (coincidences from dark APD counts) coincidences are $(98.7 \pm 0.6)\%$ and $(98 \pm 1)\%$ for N_+ and N_- respectively

— this forms the basis for the claim that the diamonds have been entangled.

To obtain the confidence interval — defined as interval $[\mu_{lo} \mu_{hi}]$ for which $P(\mu \in [\mu_{lo} \mu_{hi}]) = \mathcal{C}'$, where \mathcal{C}' is a predetermined confidence level — for the quoted concurrences, however, one first calculates a normalised probability function

$$R(X, \mu) = \frac{P(X|\mu)}{P(X|\mu_{max})}, \quad (4.21)$$

where μ_{max} is the best estimate for the true Poissonian parameter which is given by the number of detected triple coincidences ($= 3$). Then, for each constant μ , arrange the probabilities $P(X|\mu)$ by the associated normalised value $R(X, \mu)$ in descending order and calculate the sum of $P(X|\mu)$ in the same order until the predetermined confidence level \mathcal{C}' is surpassed — this marks the acceptance interval $[X_{lo} X_{hi}]$ for a given μ , such that $P(X \in [X_{lo} X_{hi}]|\mu) = \mathcal{C}'$. From here, the confidence interval $[\mu_{lo} \mu_{hi}]$ is given by the lowest and highest values of μ which are within the acceptance range for $P(X = 3|\mu)$.

The confidence interval and level can also be calculated using Bayesian statistics, by constructing an *a priori* probability distribution $P(\mu)$ to generate an *a posteriori* probability function $P(\mu|X)$ ^[198–200]. However, the optimal choice of $P(\mu)$ for a given measurement is an open problem, though calculations using some of the more conventional choices based on the literature suggests that the derived confidence intervals are broadly similar to the frequentist approach.

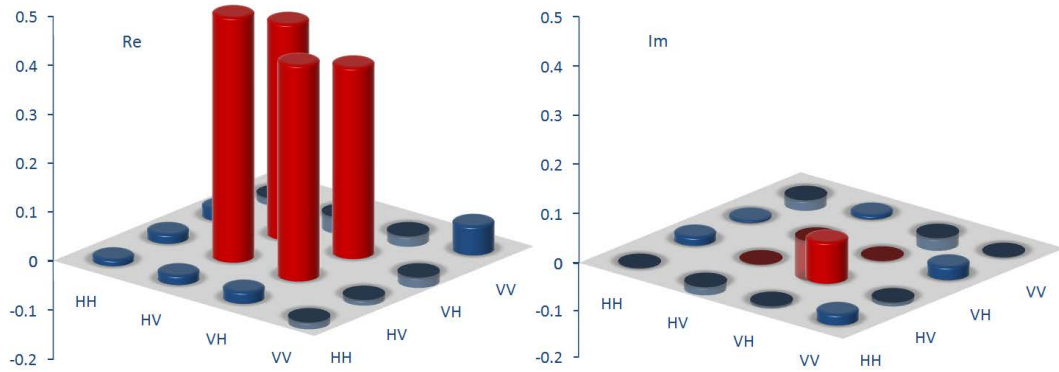


Figure 4.8 Reconstructed joint polarisation state of the Stokes/anti-Stokes modes, projected into the sub-space containing one photon in each mode. The state appears to be highly entangled in polarisation after post-selection of this sub-space, which demonstrates strong coherence between the diamonds, suggestive of near-maximal entanglement. This complements the evidence for genuine entanglement provided by Fig. 4.7.

4.3.3 Quantum (reduced) state tomography

A prerequisite for the creation of an entangled, rather than a separable, state in this experiment is that only one phonon has been created between the pair of diamonds, and the two phonon scattering rate is negligible. Having shown that to be definitively true with a calculation of positive concurrence obtained from the density matrix in Fig. 4.7 that includes this two phonons term, I then made a measurement to estimate the quality of the entanglement between the two phonon modes themselves.

Essentially, the detection scheme in this experiment (Fig. 4.1) maps the Stokes mode from the L(R) arms into $|H\rangle(|V\rangle)$ polarisations at PBS3 and anti-Stokes from L(R) into $|V\rangle(|H\rangle)$ at PBS4. Under an idealised pump-probe interaction, the re-

sulting joint Stokes/anti-Stokes state is a pure state of the form

$$|\Psi\rangle_{S,A} = \frac{1}{\sqrt{2}} \left(|HV\rangle_{S,A} + e^{i\phi} |VH\rangle_{S,A} \right), \quad (4.22)$$

for a relative phase ϕ . The presence of phonon decoherence would convert Eq. (4.22) into a mixed state, with concurrence < 1 . Therefore, to measure the concurrence between the phonon states of the diamonds, I performed quantum state tomography^[201] on the joint Stokes/anti-Stokes modes, post-selecting on the detection of both photons. This suppresses the contribution from the vacuum component in Fig. 4.7, which is caused by inefficiencies in coupling, detection, and read-out of the anti-Stokes mode.

In the experimental setup, QWPs and HWPs are seated in front of PBS3,4 so that the detectors can measure the joint Stokes/anti-Stokes state in the set of basis states of the Pauli matrices ($|HV\rangle, |DA\rangle, |RL\rangle$ etc.). 36 measurements are made using detectors D_s, D_{a+} and the accidental coincidences are subtracted [Eq. (3.15)] from the raw coincidences. Figure 4.8 shows the reconstructed state $\hat{\rho}_{S,A}$ using a Matlab script written by N. Langford which implements a maximum likelihood analysis with convex optimisation^[201] on this background subtracted data. The concurrence from this post-selected state is 0.85 and the fidelity to the nearest Bell state [of the form in Eq. (4.22)] was found by J. Nunn to be 0.91^[188]. This sets an upper limit to the maximum amount of entanglement that can be achieved in the non-post-selected state for the two diamonds as read-out efficiency, coupling

and detector efficiencies approach unity (i.e. $p_{00} \rightarrow 0$).

In this experiment, short-lived quantum correlations were revealed by combining an ultrafast interferometric pump-probe scheme with photon counting techniques. The large optical bandwidth enabled the resolution of extremely fast dynamics in the solids, and also operation at high data rates, providing sufficient statistics to establish entanglement even in the presence of losses. This approach lays the foundation for future studies of quantum phenomena in many-body, strongly-interacting systems coupled to strongly decohering environments and points towards a novel platform for ultrafast quantum information processing at room temperature.

Chapter 5

Conclusions

From its conception in the 1980's^[202], it has been apparent that quantum computing has the potential to be a hugely disruptive technology, and this has only been reinforced by further investigations in the 1990's revealing ever more remarkable capabilities in this fertile field of research — such as cryptographic security that is guaranteed by the laws of physics^[203], exponentially fast factorisation^[204] and search^[205] algorithms. The 2000's saw rapid progress in the physical realisation of these ideas, demonstrating the manipulations of qubits in an ever increasing range of systems, including, for instance, NMR^[6], superconductors^[206] and trapped ions^[207]. Even as this trend has continued into recent years, efforts have been made to bring these quantum technologies from the laboratory settings to the every day world, and experiments in the solid states such as RE doped crystals^[33], diamond NV centres^[208], and increasingly sophisticated setups using warm atomic gas^[28,31,32] form part of this progression.

In this thesis, I performed a series of experiments to show that optical phonon in diamonds, a previously overlooked system, has the same capabilities as the more proven atomic gases, while being endowed with the same unique advantages which make diamond a material that has long been recognised as ideal for the construction of practical quantum devices. As well as proving to be easy to use (quantum signatures can be obtained from diamond in ambient environment, with no optical pumping), these demonstrations also prove to be rather interesting from a fundamental point of view. In chapter 2, I have explained that a phonon is nothing but a collective vibrational *motion* of atoms, which is otherwise a well-understood concept that can be easily related to using classical physics, and in chapter 4, I have also pointed out that the phonon mode in each diamond encompasses around 10^{16} atoms for the given optical geometries in my experiments. In light of this, the observations of counterintuitive quantum dynamics in chapters 3 & 4 within such an intuitive classical system seem to suggest that the historical distinction between the ‘classical’ and ‘quantum’ realms is a rather artificial construct. At the same time, it is exciting to note that bulk mechanical oscillators can be now cooled to the thermal ground state^[184,209,210], and given the results in this thesis, there is every indication that quantum effects will be observed in ever more massive objects, leading to improved understanding of the decoherence process which leads to the transition from quantum to classical behaviours^[211].

5.1 Summary

The genesis of the ideas contained in this thesis lies in the pioneering work done by F. Waldermann^[114], whose investigations into the viabilities of photon storage in various diamond systems were in turn motivated by the pursuit of a practical linear optical quantum computation device. In chapter 1, I started with an exposition of the capabilities and requirements of quantum computation, and the role of a quantum memory, capable of single photon storage, in a quantum network. I outlined the basic principles behind different implementations of photon storage in atomic ensembles, as well as contrasting atomic gases (an oft-used medium in these types of experiments) with solid state NV centres as storage mediums.

Chapter 2 introduces Stokes scattering from optical phonons in diamond and discusses the advantages of using phonons as testbed for quantum effects. Unlike scattering in atomic gases, the regular structure of a solid crystal introduces anisotropies to light-matter interactions, and I included a condensed description of the underlying group theory which leads to the polarisation selection rules in the Raman scattering process. The Raman scattering mechanisms are further discussed, and the theoretical results of the group theory calculations are related to the focussing geometry used in subsequent experiments. From here, I described my first experiment (TCUPS) which essentially extends an experimental technique first used by Waldermann^[212] to characterise phonon decoherence for various diamond samples. Using the Schrödinger picture to describe state evolution, and Heisenberg picture to describe operator evolution, the experiment is interpreted as a temporal equivalent

of the Young's slits experiment, where the distinguishability of the Stokes modes scattered from a pump-probe pulse pair is directly related to the phonon coherence.

While Stokes scattering is a first order Raman scattering process, anti-Stokes scattering, the interaction of interest in chapter 3, is a second order process, and quantum mechanics predict that Stokes and anti-Stokes photons are emitted as a correlated photon pair through a quantum memory write-read interaction. The degree of correlation is experimentally measured to exceed the Cauchy-Schwarz inequality — which sets an upper bound to the maximal achievable degree of correlation between two classical states — in a single photon level experiment. This result demonstrates nonclassical motion in bulk diamond. Anti-Stokes production in the spontaneous and stimulated scattering limits are demonstrated through a power measurement and the results are shown to fit well against a numerical model, which is then also used to demonstrate the sensitivity of the single photon level measurement to stray photon noise. Extension of the theoretical model developed in chapter 2 shows that the population lifetime of the phonon can be obtained using the correlated anti-Stokes production process, and an explicit relation to the phonon coherence time is derived. The population lifetimes of 3 diamond samples are then compared in a novel spectroscopic experiment (SAUCERS) against coherence times obtained from TCUPS, which suggests that pure dephasing effects are negligible in diamond.

The entanglement experiment in chapter 4 is essentially an adaptation of the atomic ensemble entanglement experiment^[106] (which is in turn based on the DLCZ

protocol^[16]). Here, two diamonds act as two spatially separated quantum memories, and the two phonon modes are entangled, then verified, via projective measurements in the Bell state. Since this experiment is essentially an amalgamation of all of the preceding setups detailed in the thesis, the section on experimental technique in this chapter is of relevance to all experiments in this thesis. From a theoretical discussion of the interactions, I have shown that the unavoidable high-order interactions in the pump-probe process can mimic the quantum interference signatures of entanglement, and, in fact, the observed interference effect is close to the limit that is expected for the given experimental conditions. To form a strict verification of entanglement, I measured the rate of the higher-order scattering process, and concluded, through the entanglement measure *concurrence*, that it was insufficient to cause the observed amount of interference in the experiment. Using a conventional state tomography technique, it can also be shown that, in the limit of unit detection and readout efficiencies, the joint ensemble state created between the diamond pair can reach a fidelity of 0.9 with the nearest Bell state.

5.2 Outlook

This thesis has demonstrated that diamond phonon is a viable resource for constructing room-temperature solid state quantum devices. As a further proof of its potential for this purpose, in parallel to the work here, a random number generator has recently been implemented using diamond phonon^[213]. However, the results in this thesis also point to some room for improvements if bulk diamond were to be

used for single photon level operations. For example, in chapter 4, the concurrence of the joint state [Eq. (4.18)], including the higher-order scattering terms, is estimated to be several orders of magnitudes lower than the level that can in principle be reached — which is estimated from the concurrence of the post-selected, reduced state density (Fig. 4.8). Key to improving the quality of the generated entanglement is to improve the detection (including coupling) and readout efficiencies, since the coherence of the entangled state scales linearly with the measured rate of readout anti-Stokes production [Eq. (4.7)].

In my experiments, the detection rate of the signal photons is mainly limited by the coupling efficiencies of the Stokes and anti-Stokes signals into the SMFs, which are essential components of the setup that are used to reject unwanted photons. Efforts to improve mode-matching were hampered by the fact that at the single photon level, the Stokes and anti-Stokes beams were too weak to be imaged, and a reliable method of measuring the coupling efficiency of the fibres could not be established. This obstacle can in principle be bypassed by using bulk diamond that has been etched into a waveguide structure as part of an integrated micro-photonics chip. Here, the output optical modes would be defined by the waveguide structure, which can be tailored to match the relevant fibre modes. Diamond etching techniques already exist^[102], and doubtless the capabilities of the techniques will only improve in time.

It has been already mentioned in chapter 3 that the optical phonon lifetime can be influenced by increasing the isotopic purity of the sample, until the phonon

lifetime is limited by the Klemens decay channel^[126]. This in turn can be suppressed by constructing a superlattice of C¹² and C¹³ atoms. In order to suppress Klemens decay in all three dimensions, the super-lattice may have to be structured along all three axis. However, in a diamond waveguide structure, it may be sufficient to engineer the super-lattice to suppress phonon decay along the light propagation direction only, since phonon confinement can be achieved by controlling the width of the waveguide^[214], forbidding phonon propagations perpendicular to waveguide axis.

Due to its dispersion, anti-Stokes readout in diamond is not a phasematched process, resulting in a reduced rate of heralded anti-Stokes production. The effect of phase mismatch is more severe for longer interaction lengths, and this is corroborated by the measured $g_{S,A}^{(2)}$ value for the 0.5 mm thick diamond in chapter 3 (~ 5) being smaller than that of the 0.25 mm thick samples used in chapter 4 (~ 10). In fact, I have also attempted a correlation measurement using a 3 mm thick diamond sample and found that $g_{S,A}^{(2)} \sim 1$. Due to the lack of availability of samples with differing thickness, I have been unable to confirm that this drop off matches up with what would be expected from theoretical calculations of phase mismatch. But assuming this to be a significant effect, I propose to solve this issue using a diamond lattice consisting of two interweaving stacks whose $[1\ 0\ 0]$ axes are at 45° to each other. In an experiment, this sample would be orientated such that the $[1\ 0\ 0]$ axes of one of these sets (set ‘A’) of diamond layers would be aligned parallel to incoming pump-probe pulses, and the other (set ‘B’) at 45° to polarisation of the incident light. Polarisation

selection rules would dictate that the pump light generates orthogonally polarised Stokes light from set A, while scattering from set B would generate Stokes light polarised parallel to the pump (Fig. 2.6). Anti-Stokes scattering from the probe light would obey the same polarisation selection rule and simultaneously readout into both polarisation basis, but here, the layer thickness of this diamond stack can be chosen such that the readout anti-Stokes would be quasi-phasesmatched for both polarisations. A waveguide consisting of such a stack would be able to generate an arbitrarily high Raman scattering cross-section, while avoiding the constraints of phase mismatch.

Bibliography

- [1] K. Gibson and T. Ingold, *Tools, language, and cognition in human evolution*, Cambridge University Press (1994).
- [2] M. Hilbert and P. López, *The World's Technological Capacity to Store, Communicate, and Compute Information*, *Science*, **332**, pp. 60–65 (2011).
- [3] *Proceedings 35th Annual Symposium on Foundations of Computer Science*, in *Proceedings of the 35th Annual Symposium on Foundations of Computer Science*, SFCS '94, p. 124, IEEE Computer Society, Washington, DC, USA (1994).
- [4] R. Jozsa and N. Linden, *On the role of entanglement in quantum-computational speed-up*, *Proceedings of the Royal Society of London. Series A: Mathematical, Physical and Engineering Sciences*, **459**, pp. 2011–2032 (2003).
- [5] C. Monroe, D. M. Meekhof, B. E. King, W. M. Itano, and D. J. Wineland, *Demonstration of a Fundamental Quantum Logic Gate*, *Physical Review Letters*, **75**, pp. 4714–4717 (1995).
- [6] J. A. Jones and M. Mosca, *Implementation of a quantum algorithm on a nuclear magnetic resonance quantum computer*, **109**, pp. 1648–1653 (1998).
- [7] D. Deutsch and R. Jozsa, *Rapid Solution of Problems by Quantum Computation*, *Proceedings of the Royal Society of London. Series A: Mathematical and Physical Sciences*, **439**, pp. 553–558 (1992).
- [8] C. Negrevergne, T. S. Mahesh, C. A. Ryan, M. Ditty, F. Cyr-Racine, W. Power, N. Boulant, T. Havel, D. G. Cory, and R. Laflamme, *Benchmarking Quantum Control Methods on a 12-Qubit System*, *Physical Review Letters*, **96**, p. 170501 (2006).
- [9] K.-A. Brickman, P. C. Haljan, P. J. Lee, M. Acton, L. Deslauriers, and C. Monroe, *Implementation of Grover's quantum search algorithm in a scalable system*, *Phys. Rev. A*, **72**, p. 050306 (2005).
- [10] L. DiCarlo, J. M. Chow, J. M. Gambetta, L. S. Bishop, B. R. Johnson, D. I. Schuster, J. Majer, A. Blais, L. Frunzio, S. M. Girvin, and R. J. Schoelkopf,

- Demonstration of two-qubit algorithms with a superconducting quantum processor*, Nature, **460**, pp. 240–244 (2009).
- [11] A. Politi, J. C. F. Matthews, and J. L. O’Brien, *Shor’s Quantum Factoring Algorithm on a Photonic Chip*, Science, **325**, p. 1221 (2009).
- [12] C. Bennett and G. Brassard, *Quantum Cryptography: Public key distribution and coin tossing*, Proceedings of the IEEE International Conference on Computers, Systems, and Signal Processing, Bangalore, p. 175 (1984).
- [13] C. H. Bennett, G. Brassard, C. Crépeau, R. Jozsa, A. Peres, and W. K. Wootters, *Teleporting an unknown quantum state via dual classical and Einstein-Podolsky-Rosen channels*, Phys. Rev. Lett., **70**, pp. 1895–1899 (1993).
- [14] D. Bouwmeester, J.-W. Pan, K. Mattle, M. Eibl, H. Weinfurter, and A. Zeilinger, *Experimental quantum teleportation*, Nature, **390**, pp. 575–579 (1997).
- [15] H. Buhrman, R. Cleve, and W. van Dam, *Quantum Entanglement and Communication Complexity*, **30**, pp. 1829–1841 (2001).
- [16] L. M. Duan, M. D. Lukin, J. I. Cirac, and P. Zoller, *Long-distance quantum communication with atomic ensembles and linear optics*, Nature, **414**, pp. 413–418 (2001).
- [17] N. Sangouard, C. Simon, H. de Riedmatten, and N. Gisin, *Quantum repeaters based on atomic ensembles and linear optics*, Rev. Mod. Phys., **83**, pp. 33–80 (2011).
- [18] R. Horodecki, P. Horodecki, M. Horodecki, and K. Horodecki, *Quantum entanglement*, Rev. Mod. Phys., **81**, pp. 865–942 (2009).
- [19] E. Knill, R. Laflamme, and G. J. Milburn, *A scheme for efficient quantum computation with linear optics*, Nature, **409**, pp. 46–52 (2001).
- [20] P. Kolchin, *Electromagnetically-induced-transparency-based paired photon generation*, Physical Review A (Atomic, Molecular, and Optical Physics), **75**, 033814 (2007).
- [21] S. Chen, Y.-A. Chen, T. Strassel, Z.-S. Yuan, B. Zhao, J. Schmiedmayer, and J.-W. Pan, *Deterministic and Storable Single-Photon Source Based on a Quantum Memory*, Phys. Rev. Lett., **97**, p. 173004 (2006).
- [22] D. N. Matsukevich, T. Chanelière, S. D. Jenkins, S.-Y. Lan, T. A. B. Kennedy, and A. Kuzmich, *Deterministic Single Photons via Conditional Quantum Evolution*, Phys. Rev. Lett., **97**, p. 013601 (2006).

- [23] Z.-S. Yuan, Y.-A. Chen, S. Chen, B. Zhao, M. Koch, T. Strassel, Y. Zhao, G.-J. Zhu, J. Schmiedmayer, and J.-W. Pan, *Synchronized Independent Narrow-Band Single Photons and Efficient Generation of Photonic Entanglement*, Phys. Rev. Lett., **98**, p. 180503 (2007).
- [24] H. J. Kimble, M. Dagenais, and L. Mandel, *Photon Antibunching in Resonance Fluorescence*, Phys. Rev. Lett., **39**, pp. 691–695 (1977).
- [25] C. Cohen-Tannoudji, *Manipulating atoms with photons*, Physica Scripta, **1998**, p. 33 (1998).
- [26] J. I. Cirac, P. Zoller, H. J. Kimble, and H. Mabuchi, *Quantum State Transfer and Entanglement Distribution among Distant Nodes in a Quantum Network*, Phys. Rev. Lett., **78**, pp. 3221–3224 (1997).
- [27] H. P. Specht, C. Nolleke, A. Reiserer, M. Uphoff, E. Figueroa, S. Ritter, and G. Rempe, *A single-atom quantum memory*, Nature, **473**, pp. 190–193 (2011).
- [28] D. F. Phillips, A. Fleischhauer, A. Mair, R. L. Walsworth, and M. D. Lukin, *Storage of Light in Atomic Vapor*, Phys. Rev. Lett., **86**, pp. 783–786 (2001).
- [29] M. Fleischhauer and M. Lukin, *Quantum memory for photons: Dark-state polaritons*, Physical Review A, **65**, p. 22314 (2002).
- [30] S. A. Moiseev and S. Kröll, *Complete Reconstruction of the Quantum State of a Single-Photon Wave Packet Absorbed by a Doppler-Broadened Transition*, Phys. Rev. Lett., **87**, p. 173601 (2001).
- [31] A. E. Kozhokin, K. Mølmer, and E. Polzik, *Quantum Memory for Light*, Phys. Rev. A, **62**, p. 033809 (2000).
- [32] K. F. Reim, J. Nunn, V. O. Lorenz, B. J. Sussman, K. C. Lee, N. K. Langford, D. Jaksch, and I. A. Walmsley, *Towards high-speed optical quantum memories*, Nature Photonics, **4**, pp. 218–221 (2010).
- [33] W. Tittel, M. Afzelius, T. Chanelière, R. Cone, S. Kröll, S. Moiseev, and M. Sellars, *Photon-echo quantum memory in solid state systems*, Laser & Photonics Reviews, **4**, pp. 244–267 (2010).
- [34] S. Borkar, *Design perspectives on 22nm CMOS and beyond*, in *Design Automation Conference, 2009. DAC '09. 46th ACM/IEEE*, pp. 93–94 (2009).
- [35] M. Hochberg and T. Baehr-Jones, *Towards fabless silicon photonics*, Nat Photon, **4**, pp. 492–494 (2010).
- [36] S. Praver and A. D. Greentree, *APPLIED PHYSICS: Diamond for Quantum Computing*, Science, **320**, pp. 1601–1602 (2008).

- [37] J. R. Weber, W. F. Koehl, J. B. Varley, A. Janotti, B. B. Buckley, C. G. Van de Walle, and D. D. Awschalom, *Quantum computing with defects*, Proceedings of the National Academy of Sciences, **107**, pp. 8513–8518 (2010).
- [38] J. Wrachtrup, *Defect center room-temperature quantum processors*, Proceedings of the National Academy of Sciences, **107**, pp. 9479–9480 (2010).
- [39] A. Politi, M. J. Cryan, J. G. Rarity, S. Yu, and J. L. O’Brien, *Silica-on-Silicon Waveguide Quantum Circuits*, Science, **320**, pp. 646–649 (2008).
- [40] B. J. Smith, D. Kundys, N. Thomas-Peter, P. G. R. Smith, and I. A. Walmsley, *Phase-controlled integrated photonic quantum circuits*, Opt. Express, **17**, pp. 13516–13525 (2009).
- [41] W. Akhtar, V. Filidou, T. Sekiguchi, E. Kawakami, T. Itahashi, L. Vlasenko, J. J. L. Morton, and K. M. Itoh, *Coherent storage of photoexcited triplet states using ^{29}Si nuclear spins in silicon*, ArXiv e-prints (2011).
- [42] Y.-R. Chang, H.-Y. Lee, K. Chen, C.-C. Chang, D.-S. Tsai, C.-C. Fu, T.-S. Lim, Y.-K. Tzeng, C.-Y. Fang, C.-C. Han, H.-C. Chang, and W. Fann, *Mass production and dynamic imaging of fluorescent nanodiamonds*, Nat Nano, **3**, pp. 284–288 (2008).
- [43] J. Che, T. Cagin, W. Deng, and W. A. G. III, *Thermal conductivity of diamond and related materials from molecular dynamics simulations*, The Journal of Chemical Physics, **113**, pp. 6888–6900 (2000).
- [44] D. J. Spence, E. Granados, and R. P. Mildren, *Mode-locked picosecond diamond Raman laser*, Opt. Lett., **35**, pp. 556–558 (2010).
- [45] A. V. Gorshkov, A. André, M. D. Lukin, and A. S. S. rensen, *Photon storage in Lambda-type optically dense atomic media. II. Free-space model*, Physical Review A (Atomic, Molecular, and Optical Physics), **76**, 033805 (2007).
- [46] J. Nunn, K. Reim, K. C. Lee, V. O. Lorenz, B. J. Sussman, I. A. Walmsley, and D. Jaksch, *Multimode Memories in Atomic Ensembles*, Physical Review Letters, **101**, 260502 (2008).
- [47] A. V. Gorshkov, A. Andre, M. Fleischhauer, A. S. Sorensen, and M. D. Lukin, *Universal Approach to Optimal Photon Storage in Atomic Media*, Physical Review Letters, **98**, 123601 (2007).
- [48] C. Liu, Z. Dutton, C. H. Behroozi, and L. V. Hau, *Observation of coherent optical information storage in an atomic medium using halted light pulses*, Nature, **409**, pp. 490–493 (2001).
- [49] K.-J. Boller, A. Imamolu, and S. E. Harris, *Observation of electromagnetically induced transparency*, Phys. Rev. Lett., **66**, pp. 2593–2596 (1991).

- [50] S. E. Harris, *Electromagnetically Induced Transparency*, *Physics Today*, **50**, pp. 36–42 (1997).
- [51] M. Fleischhauer and M. D. Lukin, *Dark-State Polaritons in Electromagnetically Induced Transparency*, *Physical Review Letters*, **84**, pp. 5094–5097 (2000).
- [52] S. Manz, T. Fernholz, J. Schmiedmayer, and J.-W. Pan, *Collisional decoherence during writing and reading quantum states*, *Physical Review A (Atomic, Molecular, and Optical Physics)*, **75**, p. 040101 (2007).
- [53] A. Lvovsky, B. Sanders, and W. Tittel, *Optical quantum memory*, *Nature Photonics*, **3**, pp. 706–714 (2009).
- [54] A. Javan, O. Kocharovskaya, H. Lee, and M. O. Scully, *Narrowing of electromagnetically induced transparency resonance in a Doppler-broadened medium*, *Physical Review A (Atomic, Molecular, and Optical Physics)*, **66**, p. 013805 (2002).
- [55] A. Kuzmich, W. P. Bowen, A. D. Boozer, A. Boca, C. W. Chou, L.-M. Duan, and H. J. Kimble, *Generation of nonclassical photon pairs for scalable quantum communication with atomic ensembles*, *Nature*, **423**, pp. 731–734 (2003).
- [56] T. Chaneliere, D. N. Matsukevich, S. D. Jenkins, S. Y. Lan, T. A. B. Kennedy, and A. Kuzmich, *Storage and retrieval of single photons transmitted between remote quantum memories*, *Nature*, **438**, pp. 833–836 (2005).
- [57] M. D. Eisaman, A. Andre, F. Massou, M. Fleischhauer, A. S. Zibrov, and M. D. Lukin, *Electromagnetically induced transparency with tunable single-photon pulses*, *Nature*, **438**, pp. 837–841 (2005/12/08/print).
- [58] A. V. Turukhin, V. S. Sudarshanam, M. S. Shahriar, J. A. Musser, B. S. Ham, and P. R. Hemmer, *Observation of Ultraslow and Stored Light Pulses in a Solid*, *Physical Review Letters*, **88**, p. 023602 (2001).
- [59] J. J. Longdell, E. Fraval, M. J. Sellars, and N. B. Manson, *Stopped Light with Storage Times Greater than One Second Using Electromagnetically Induced Transparency in a Solid*, *Physical Review Letters*, **95**, 063601 (2005).
- [60] E. L. Hahn, *Spin Echoes*, *Physical Review*, **80**, pp. 580–594 (1950).
- [61] J. Ruggiero, J. Le Gou
”et, C. Simon, and T. Chanelière, *Why the two-pulse photon echo is not a good quantum memory protocol*, *Physical Review A*, **79**, p. 53851 (2009).
- [62] P. M. Ledingham, W. R. Naylor, J. J. Longdell, S. E. Beavan, and M. J. Sellars, *Nonclassical photon streams using rephased amplified spontaneous emission*, *Phys. Rev. A*, **81**, p. 012301 (2010).

- [63] A. Alexander, J. Longdell, M. Sellars, and N. Manson, *Photon Echoes Produced by Switching Electric Fields*, Physical Review Letters, **96**, p. 43602 (2006).
- [64] N. Sangouard, C. Simon, M. Afzelius, and N. Gisin, *Analysis of a quantum memory for photons based on controlled reversible inhomogeneous broadening*, Physical Review A, **75**, p. 032327 (2007).
- [65] G. Hétet, J. J. Longdell, A. L. Alexander, P. K. Lam, and M. J. Sellars, *Electro-Optic Quantum Memory for Light Using Two-Level Atoms*, Physical Review Letters, **100**, p. 023601 (2008).
- [66] G. Hétet, M. Hosseini, B. M. Sparkes, D. Oblak, P. K. Lam, and B. C. Buchler, *Photon echoes generated by reversing magnetic field gradients in a rubidium vapor*, Opt. Lett., **33**, pp. 2323–2325 (2008).
- [67] T. Böttger, Y. Sun, C. W. Thiel, and R. L. Cone, *Spectroscopy and dynamics of $\text{Er}^{3+} : \text{Y}_2\text{SiO}_5$ at 1.5 μm* , Physical Review B (Condensed Matter and Materials Physics), **74**, p. 075107 (2006).
- [68] B. Lauritzen, J. c. v. Minář, H. de Riedmatten, M. Afzelius, N. Sangouard, C. Simon, and N. Gisin, *Telecommunication-Wavelength Solid-State Memory at the Single Photon Level*, Physical Review Letters, **104**, p. 080502 (2010).
- [69] A. V. Gorshkov, A. Andre, M. D. Lukin, and A. S. Sorensen, *Photon storage in Lambda-type optically dense atomic media. II. Free-space model*, Physical Review A, **76**, p. 033805 (2007).
- [70] J. Nunn, I. A. Walmsley, M. G. Raymer, K. Surmacz, F. C. Waldermann, Z. Wang, and D. Jaksch, *Mapping broadband single-photon wave packets into an atomic memory*, Physical Review A (Atomic, Molecular, and Optical Physics), **75**, 11401 (2007).
- [71] I. Novikova, A. V. Gorshkov, D. F. Phillips, A. S. Sorensen, M. D. Lukin, and R. L. Walsworth, *Optimal Control of Light Pulse Storage and Retrieval*, Physical Review Letters, **98**, 243602 (2007).
- [72] M. P. Hedges, J. J. Longdell, Y. Li, and M. J. Sellars, *Efficient quantum memory for light*, Nature, **465**, pp. 1052–1056 (2010).
- [73] M. Hosseini, B. M. Sparkes, G. Campbell, P. K. Lam, and B. C. Buchler, *High efficiency coherent optical memory with warm rubidium vapour*, Nature Communications, **2** (2011).
- [74] V. Damon, M. Bonarota, A. Louchet-Chauvet, T. Chanelière, and J.-L. Le Gouët, *Revival of silenced echo and quantum memory for light*, New Journal of Physics, **13**, p. 093031 (2011).

- [75] D. L. McAuslan, P. M. Ledingham, W. R. Naylor, S. E. Beavan, M. P. Hedges, M. J. Sellars, and J. J. Longdell, *Photon-echo quantum memories in inhomogeneously broadened two-level atoms*, Physical Review A (Atomic, Molecular, and Optical Physics), **84**, p. 022309 (2011).
- [76] M. Afzelius, C. Simon, H. De Riedmatten, and N. Gisin, *Multimode quantum memory based on atomic frequency combs*, Physical Review A, **79**, p. 52329 (2009).
- [77] H. de Riedmatten, M. Afzelius, M. U. Staudt, C. Simon, and N. Gisin, *A solid-state light-matter interface at the single-photon level*, Nature, **456**, pp. 773–777 (2008).
- [78] M. Bonarota, J. Ruggiero, J. L. L. Gouët, and T. Chanelière, *Efficiency optimization for atomic frequency comb storage*, Physical Review A (Atomic, Molecular, and Optical Physics), **81**, p. 033803 (2010).
- [79] A. Amari, A. Walther, M. Sabooni, M. Huang, S. KrÄäll, M. Afzelius, I. Usmani, B. Lauritzen, N. Sangouard, H. de Riedmatten, and N. Gisin, *Towards an efficient atomic frequency comb quantum memory*, Journal of Luminescence, **130**, pp. 1579 – 1585 (2010), [|ce:title|Special Issue based on the Proceedings of the Tenth International Meeting on Hole Burning, Single Molecule, and Related Spectroscopies: Science and Applications \(HBSM 2009\) - Issue dedicated to Ivan Lorgere and Oliver Guillot-Noel|/ce:title|](#).
- [80] M. Afzelius, I. Usmani, A. Amari, B. Lauritzen, A. Walther, C. Simon, N. Sangouard, J. Minář, H. De Riedmatten, N. Gisin, et al., *Demonstration of atomic frequency comb memory for light with spin-wave storage*, Physical review letters, **104**, p. 40503 (2010).
- [81] E. Saglamyurek, N. Sinclair, J. Jin, J. A. Slater, D. Oblak, F. Bussieres, M. George, R. Ricken, W. Sohler, and W. Tittel, *Broadband waveguide quantum memory for entangled photons*, Nature, **469**, pp. 512–515 (2011).
- [82] C. Raman and K. Krishnan, *A new type of secondary radiation*, Nature, **121**, p. 501 (1928).
- [83] N. Bloembergen, *A Quarter century of stimulated Raman scattering1*, Encounters in Nonlinear Optics: Selected Papers of Nicolaas Bloembergen, with Commentary, p. 375 (1996).
- [84] M. G. Raymer and J. Mostowski, *Stimulated Raman scattering: Unified treatment of spontaneous initiation and spatial propagation*, Phys. Rev. A, **24(4)**, pp. 1980–1993 (1981).
- [85] M. G. Raymer and I. A. Walmsley, *Progress in Optics*, Elsevier Science Publishers B.V., xxviii edition (1990).

- [86] S. A. Solin and A. K. Ramdas, *Raman Spectrum of Diamond*, Physical Review B (Condensed Matter and Materials Physics), **1**, pp. 1687–1698 (1970).
- [87] T. K. Cheng, S. D. Brorson, A. S. Kazeroonian, J. S. Moodera, G. Dresselhaus, M. S. Dresselhaus, and E. P. Ippen, *Impulsive excitation of coherent phonons observed in reflection in bismuth and antimony*, Applied Physics Letters, **57**, pp. 1004–1006 (1990).
- [88] P. D. Maker and R. W. Terhune, *Study of Optical Effects Due to an Induced Polarization Third Order in the Electric Field Strength*, Physical Review, **137**, pp. A801–A818 (1965).
- [89] O. Boyraz and B. Jalali, *Demonstration of a silicon Raman laser*, Opt. Express, **12**, pp. 5269–5273 (2004).
- [90] T. K. Liang and H. K. Tsang, *Efficient Raman amplification in silicon-on-insulator waveguides*, Applied Physics Letters, **85**, pp. 3343–3345 (2004).
- [91] S. M. Spillane, T. J. Kippenberg, and K. J. Vahala, *Ultralow-threshold Raman laser using a spherical dielectric microcavity*, Nature, **415**, pp. 621–623 (2002).
- [92] M. G. Raymer and I. A. Walmsley, *Quantum theory of spatial and temporal coherence properties of stimulated Raman scattering*, Phys. Rev. A, **32(1)**, pp. 332–344 (1985).
- [93] K. F. Reim, P. Michelberger, K. C. Lee, J. Nunn, N. K. Langford, and I. A. Walmsley, *Single-Photon-Level Quantum Memory at Room Temperature*, Physical Review Letters, **107**, p. 053603 (2011).
- [94] D. G. England, P. S. Michelberger, T. F. M. Champion, K. F. Reim, K. C. Lee, M. R. Sprague, X.-M. Jin, N. K. Langford, W. S. Kolthammer, J. Nunn, and I. A. Walmsley, *High-Fidelity Polarization Storage in a Gigahertz Bandwidth Quantum Memory*, ArXiv e-prints (2011).
- [95] J. Bell, *On the Einstein-Podolsky-Rosen paradox*, Physics (US) Discontinued with Vol. 4, no. 1, 1968, **1** (1964).
- [96] C. F. Roos, M. Riebe, H. Häffner, W. Hänsel, J. Benhelm, G. P. T. Lancaster, C. Becher, F. Schmidt-Kaler, and R. Blatt, *Control and Measurement of Three-Qubit Entangled States*, Science, **304**, pp. 1478–1480 (2004).
- [97] J. Volz, M. Weber, D. Schlenk, W. Rosenfeld, J. Vrana, K. Saucke, C. Kurtsiefer, and H. Weinfurter, *Observation of Entanglement of a Single Photon with a Trapped Atom*, Phys. Rev. Lett., **96**, p. 030404 (2006).
- [98] B. B. Blinov, D. L. Moehring, L. M. Duan, and C. Monroe, *Observation of entanglement between a single trapped atom and a single photon*, Nature, **428**, pp. 153–157 (2004).

- [99] M. Steffen, M. Ansmann, R. C. Bialczak, N. Katz, E. Lucero, R. McDermott, M. Neeley, E. M. Weig, A. N. Cleland, and J. M. Martinis, *Measurement of the Entanglement of Two Superconducting Qubits via State Tomography*, *Science*, **313**, pp. 1423–1425 (2006).
- [100] P. Neumann, N. Mizuochi, F. Rempp, P. Hemmer, H. Watanabe, S. Yamasaki, V. Jacques, T. Gaebel, F. Jelezko, and J. Wrachtrup, *Multipartite Entanglement Among Single Spins in Diamond*, *Science*, **320**, pp. 1326–1329 (2008).
- [101] M. V. G. Dutt, L. Childress, L. Jiang, E. Togan, J. Maze, F. Jelezko, A. S. Zibrov, P. R. Hemmer, and M. D. Lukin, *Quantum Register Based on Individual Electronic and Nuclear Spin Qubits in Diamond*, *Science*, **316**, pp. 1312–1316 (2007).
- [102] A. Faraon, P. E. Barclay, C. Santori, K.-M. C. Fu, and R. G. Beausoleil, *Resonant enhancement of the zero-phonon emission from a colour centre in a diamond cavity*, *Nat Photon*, **5**, pp. 301–305 (2011).
- [103] F. Dolde, I. Jakobi, B. Naydenov, N. Zhao, S. Pezzagna, C. Trautmann, J. Meijer, P. Neumann, F. Jelezko, and J. Wrachtrup, *Room-temperature entanglement between single defect spins in diamond*, *Nature Physics*, **9**, pp. 139–143 (2013).
- [104] H. Bernien, B. Hensen, W. Pfaff, G. Koolstra, M. S. Blok, L. Robledo, T. H. Taminiau, M. Markham, D. J. Twitchen, L. Childress, and R. Hanson, *Heralded entanglement between solid-state qubits separated by 3 meters*, *ArXiv e-prints* (2012).
- [105] D. N. Matsukevich and A. Kuzmich, *Quantum State Transfer Between Matter and Light*, *Science*, **306**, pp. 663–666 (2004).
- [106] C. W. Chou, H. de Riedmatten, D. Felinto, S. V. Polyakov, S. J. van Enk, and H. J. Kimble, *Measurement-induced entanglement for excitation stored in remote atomic ensembles*, *Nature*, **438**, pp. 828–832 (2005).
- [107] D. L. Moehring, P. Maunz, S. Olmschenk, K. C. Younge, D. N. Matsukevich, L. M. Duan, and C. Monroe, *Entanglement of single-atom quantum bits at a distance*, *Nature*, **449**, pp. 68–71 (2007).
- [108] H. Zhang, X.-M. Jin, J. Yang, H.-N. Dai, S.-J. Yang, T.-M. Zhao, J. Rui, Y. He, X. Jiang, F. Yang, G.-S. Pan, Z.-S. Yuan, Y. Deng, Z.-B. Chen, X.-H. Bao, S. Chen, B. Zhao, and J.-W. Pan, *Preparation and storage of frequency-uncorrelated entangled photons from cavity-enhanced spontaneous parametric downconversion*, *Nat Photon*, **5**, pp. 628–632 (2011).
- [109] C. Clausen, I. Usmani, F. Bussières, N. Sangouard, M. Afzelius, H. de Riedmatten, and N. Gisin, *Quantum storage of photonic entanglement in a crystal*, *Nature*, **469**, pp. 508–511 (2011).

- [110] I. Usmani, C. Clausen, F. Bussi eres, N. Sangouard, M. Afzelius, and N. Gisin, *Heralded quantum entanglement between two crystals*, Arxiv preprint arXiv:1109.0440 (2011).
- [111] C. Kittel and P. McEuen, *Introduction to solid state physics*, Wiley New York (1986).
- [112] W. Hayes and R. Loudon, *Scattering of Light by Crystals*, Dover Publications, New York (2004).
- [113] G. Kresse, J. Furthm uller, and J. Hafner, *Ab initio Force Constant Approach to Phonon Dispersion Relations of Diamond and Graphite*, EPL (Europhysics Letters), **32**, p. 729 (1995).
- [114] F. C. Waldermann, *Applications of coherent phonons in quantum optics: prospects for optically controlled ensemble quantum memories in the solid state*, Ph.D. thesis, University of Oxford (2008).
- [115] K. C. Lee, B. J. Sussman, J. Nunn, V. O. Lorenz, K. Reim, D. Jaksch, I. A. Walmsley, P. Spizzirri, and S. Praver, *Comparing phonon dephasing lifetimes in diamond using Transient Coherent Ultrafast Phonon Spectroscopy*, Diamond and Related Materials, **19**, pp. 1289–1295 (2010).
- [116] *WebQC.org Chemical portal*. <http://www.webqc.org/symmetrypointgroup-oh.html> (2012).
- [117] G. Herzberg and B. L. Crawford, *Infrared and Raman Spectra of Polyatomic Molecules.*, The Journal of Physical Chemistry, **50**, pp. 288–288 (1946).
- [118] E. Wilson, J. Decius, and P. Cross, *Molecular Vibrations: The Theory of Infrared and Raman Vibrational Spectra*, Dover Books on Chemistry Series, Dover Publications (1980).
- [119] S. Sternberg, *Group theory and physics*, Cambridge University Press, Cambridge (1995).
- [120] H. Willes and R. M. Weber, *Raman scattering in materials science*, Springer, Berlin New York (2000).
- [121] M. H. Nazare, *Properties, growth and applications of diamond*, Institution of Electrical Engineers, London (2001).
- [122] W. Weber, *Raman Scattering in Materials Science*, Springer, Berlin (2000).
- [123] A. Fox, *Optical properties of solids*, Oxford master series in condensed matter physics, Oxford University Press (2010).
- [124] A. Neves, *Properties, Growth and Applications of Diamond*, Institution of Electrical Engineers, London (2001).

- [125] R. Loudon, *Selection rules for defect-activated lattice bands and vibronic transitions in face-centred cubic, diamond and zinc blende lattices*, Proceedings of the Physical Society, **84**, p. 379 (1964).
- [126] P. G. Klemens, *Anharmonic Decay of Optical Phonons*, Physical Review, **148**, pp. 845–848 (1966).
- [127] J. Asmussen and D. Reinhard, *Diamond films handbook*, Marcel Dekker, New York (2002).
- [128] G. Balasubramanian, P. Neumann, D. Twitchen, M. Markham, R. Kolesov, N. Mizuochi, J. Isoya, J. Achard, J. Beck, J. Tissler, V. Jacques, P. R. Hemmer, F. Jelezko, and J. Wrachtrup, *Ultralong spin coherence time in isotopically engineered diamond*, Nat Mater, **8**, pp. 383–387 (2009).
- [129] F. C. Waldermann, B. J. Sussman, J. Nunn, V. O. Lorenz, K. C. Lee, K. Surmacz, K. H. Lee, D. Jaksch, I. A. Walmsley, P. Spizziri, P. Olivero, and S. Praver, *Measuring phonon dephasing with ultrafast pulses using Raman spectral interference*, Physical Review B (Condensed Matter and Materials Physics), **78**, 155201 (2008).
- [130] J. R. Maze, P. L. Stanwix, J. S. Hodges, S. Hong, J. M. Taylor, P. Cappellaro, L. Jiang, M. V. G. Dutt, E. Togan, A. S. Zibrov, A. Yacoby, R. L. Walsworth, and M. D. Lukin, *Nanoscale magnetic sensing with an individual electronic spin in diamond*, Nature, **455**, pp. 644–647 (2008).
- [131] J. Ristein, W. Zhang, and L. Ley, *Hydrogen-terminated diamond electrodes. I. Charges, potentials, and energies*, Physical Review E (Statistical, Nonlinear, and Soft Matter Physics), **78**, 041602 (2008).
- [132] C. Aku-Leh, J. Zhao, R. Merlin, J. Menéndez, and M. Cardona, *Long-lived optical phonons in ZnO studied with impulsive stimulated Raman scattering*, Physical Review B (Condensed Matter and Materials Physics), **71**, p. 205211 (2005).
- [133] N. Bloembergen, M. Colles, J. Reintjes, and C. Wang, *On the spectral line shape and cross-section in transient Raman scattering*, Indian Journal of Pure and Applied Physics, **9**, pp. 874–876 (1971).
- [134] A. Laubereau, D. von der Linde, and W. Kaiser, *Decay Time of Hot TO Phonons in Diamond*, Physical Review Letters, **27**, pp. 802–805 (1971).
- [135] M. Gaukroger, P. Martineau, M. Crowder, I. Friel, S. Williams, and D. Twitchen, *X-ray topography studies of dislocations in single crystal CVD diamond*, Diamond and Related Materials, **17**, pp. 262 – 269 (2008).
- [136] L. Bergman and R. J. Nemanich, *Raman and photoluminescence analysis of stress state and impurity distribution in diamond thin films*, Journal of Applied Physics, **78**, pp. 6709–6719 (1995).

- [137] W. J. Borer, S. S. Mitra, and K. V. Namjoshi, *Line shape and temperature dependence of the first order Raman spectrum of diamond*, Solid State Communications, **9**, pp. 1377–1381 (1971).
- [138] L. M. Duan, J. I. Cirac, and P. Zoller, *Three-dimensional theory for interaction between atomic ensembles and free-space light*, Physical Review A (Atomic, Molecular, and Optical Physics), **66**, p. 023818 (2002).
- [139] W. Wasilewski and M. G. Raymer, *Pairwise entanglement and readout of atomic-ensemble and optical wave-packet modes in traveling-wave Raman interactions*, Physical Review A (Atomic, Molecular, and Optical Physics), **73**, 063816 (2006).
- [140] K. Hammerer, A. S. Sørensen, and E. S. Polzik, *Quantum interface between light and atomic ensembles*, Reviews of Modern Physics, **82**, pp. 1041–1093 (2010).
- [141] M. G. Raymer and I. A. Walmsley, *The quantum coherence properties of stimulated Raman scattering*, Progress in Optics, **23** (1990).
- [142] A. M. Zaitsev, *Optical Properties of Diamond*, Springer (2001).
- [143] K.-H. Chen, Y.-L. Lai, L.-C. Chen, J.-Y. Wu, and F.-J. Kao, *High-temperature Raman study in CVD diamond*, Thin Solid Films, **270**, pp. 143–147 (1995).
- [144] M. S. Liu, L. A. Bursill, S. Prawer, and R. Beserman, *Temperature dependence of the first-order Raman phonon line of diamond*, Physical Review B (Condensed Matter and Materials Physics), **61**, pp. 3391–3395 (2000).
- [145] A. Laubereau and W. Kaiser, *Vibrational dynamics of liquids and solids investigated by picosecond light pulses*, Reviews of Modern Physics, **50**, pp. 607–665 (1978).
- [146] A. Debernardi and M. Cardona, *First principles calculation of the real part of phonon self energy in compound semiconductors*, Physica B: Condensed Matter, **263-264**, pp. 687–690 (1999).
- [147] A. Debernardi, *Phonon linewidth in III-V semiconductors from density-functional perturbation theory*, Physical Review B (Condensed Matter and Materials Physics), **57**, pp. 12847–12858 (1998).
- [148] R. Boyd, *Nonlinear Optics*, Academic Press, Boston (2003).
- [149] J. J. Liu, D. Y. T. Chiu, D. C. Morton, D. H. Kang, V. V. Zhirnov, J. J. Hren, and J. J. Cuomo, *Band gap structure and electron emission property of chemical-vapor-deposited diamond films*, Solid-State Electronics, **45**, pp. 915–919 (2001).

- [150] A. Debernardi, S. Baroni, and E. Molinari, *Anharmonic Phonon Lifetimes in Semiconductors from Density-Functional Perturbation Theory*, Physical Review Letters, **75**, pp. 1819–1822 (1995).
- [151] K. C. Lee, B. J. Sussman, M. R. Sprague, P. Michelberger, K. F. Reim, J. Nunn, N. K. Langford, P. J. Bustard, D. Jaksch, and I. A. Walmsley, *Macroscopic non-classical states and terahertz quantum processing in room-temperature diamond*, Nature Photonics, **6**, pp. 41–44 (2012).
- [152] G. Lindblad, *On the generators of quantum dynamical semigroups*, Communications in Mathematical Physics, **48**, pp. 119–130 (1976).
- [153] K. Kang, D. Abdula, D. G. Cahill, and M. Shim, *Lifetimes of optical phonons in graphene and graphite by time-resolved incoherent anti-Stokes Raman scattering*, Physical Review B (Condensed Matter and Materials Physics), **81**, p. 165405 (2010).
- [154] A. Glazer and J. Wark, *Statistical Mechanics: A Survival Guide*, Statistical Mechanics: A Survival Guide, Oxford University Press, USA (2001).
- [155] G. Milburn, *Intrinsic decoherence in quantum mechanics*, Physical Review A, **44**, p. 5401 (1991).
- [156] J. Ellis, S. Mohanty, and D. Nanopoulos, *Quantum gravity and the collapse of the wavefunction*, Physics Letters B, **221**, pp. 113–119 (1989).
- [157] W. Strunz, F. Haake, and D. Braun, *Universality of decoherence for macroscopic quantum superpositions*, Physical Review A, **67**, p. 022101 (2003).
- [158] A. Cho, *Faintest Thrum Heralds Quantum Machines*, Science, **327**, pp. 516–518 (2010).
- [159] A. A. Michelson, *The relative motion of the Earth and the Luminiferous ether*, American Journal of Science, **22**, p. 120 (1881).
- [160] R. H. Brown and R. Q. Twiss, *Interferometry of the Intensity Fluctuations in Light. IV. A Test of an Intensity Interferometer on Sirius A*, Proceedings of the Royal Society of London. Series A. Mathematical and Physical Sciences, **248**, pp. 222–237 (1958).
- [161] R. H. Brown and R. Q. Twiss, *Interferometry of the Intensity Fluctuations in Light. III. Applications to Astronomy*, Proceedings of the Royal Society of London. Series A. Mathematical and Physical Sciences, **248**, pp. 199–221 (1958).
- [162] R. H. Brown and R. Q. Twiss, *Interferometry of the Intensity Fluctuations in Light II. An Experimental Test of the Theory for Partially Coherent Light*, Proceedings of the Royal Society of London. Series A. Mathematical and Physical Sciences, **243**, pp. 291–319 (1958).

- [163] R. H. Brown and R. Q. Twiss, *Interferometry of the Intensity Fluctuations in Light. I. Basic Theory: The Correlation between Photons in Coherent Beams of Radiation*, Proceedings of the Royal Society of London. Series A. Mathematical and Physical Sciences, **242**, pp. 300–324 (1957).
- [164] C. Foellmi, *Intensity interferometry and the second-order correlation function $g^{(2)}$ in astrophysics*, Astronomy and Astrophysics, **507**, pp. 1719–1727 (2009).
- [165] R. Loudon, *Non-classical effects in the statistical properties of light*, Reports on Progress in Physics, **43**, p. 913 (1980).
- [166] L. Mandel, *Non-Classical States of the Electromagnetic Field*, Physica Scripta, **1986**, p. 34 (1986).
- [167] R. Loudon, *The Quantum Theory of Light*, Oxford University Press (2004).
- [168] C. W. Chou, *Towards a Quantum Network with Atomic Ensembles*, Ph.D. thesis, California Institute of Technology (2006).
- [169] M. Lobino, C. Kupchak, E. Figueroa, and A. Lvovsky, *Memory for light as a quantum process*, Physical review letters, **102**, p. 203601 (2009).
- [170] A. Debernardi, S. Baroni, and E. Molinari, *Anharmonic Phonon Lifetimes in Semiconductors from Density-Functional Perturbation Theory*, Physical Review Letters, **75**, pp. 1819–1822 (1995).
- [171] M. Liu, L. Bursill, S. Prawer, and R. Beserman, *Temperature dependence of the first-order Raman phonon line of diamond*, Physical Review B, **61**, pp. 3391–3395 (2000).
- [172] G. Balasubramanian, P. Neumann, D. Twitchen, M. Markham, R. Kolesov, N. Mizuochi, J. Isoya, J. Achard, J. Beck, J. Tessler, et al., *Ultralong spin coherence time in isotopically engineered diamond*, Nature Materials, **8**, pp. 383–387 (2009).
- [173] A. Cattellani and L. Sorba, *Acoustic-wave transmission in semiconductor superlattices*, Physical Review B, **38**, p. 7717 (1988).
- [174] K. C. Hass, M. A. Tamor, T. R. Anthony, and W. F. Banholzer, *Lattice dynamics and Raman spectra of isotopically mixed diamond*, Physical Review B, **45**, pp. 7171–7182 (1992).
- [175] R. Chrenko, *^{13}C -doped diamond: Raman spectra*, Journal of applied physics, **63**, pp. 5873–5875 (1988).
- [176] M. O. Scully and A. A. Svidzinsky, *The Super of Superradiance*, Science, **325**, pp. 1510–1511 (2009).

- [177] M. Scully, *Correlated spontaneous emission on the Volga*, Laser Physics, **17**, pp. 635–646 (2007), 10.1134/S1054660X07050064.
- [178] M. Sørensen and A. Sørensen, *Three-dimensional theory of stimulated Raman scattering*, Physical Review A, **80**, p. 033804 (2009).
- [179] K. Ishioka, M. Hase, M. Kitajima, and H. Petek, *Coherent Optical Phonons in Diamond*, Applied Physics Letters, **89**, p. 231916 (2007).
- [180] P. J. Dean, *Bound Excitons and Donor-Acceptor Pairs in Natural and Synthetic Diamond*, Physical Review, **139**, pp. A588–A602 (1965).
- [181] P. L. Hanley, I. Kiflawi, and A. R. Lang, *On Topographically Identifiable Sources of Cathodoluminescence in Natural Diamonds*, Philosophical Transactions of the Royal Society of London. Series A, Mathematical and Physical Sciences, **284**, pp. 329–368 (1977).
- [182] A. K. Ramdas, S. Rodriguez, M. Grimsditch, T. R. Anthony, and W. F. Banholzer, *Effect of isotopic constitution of diamond on its elastic constants: C13 diamond, the hardest known material*, Physical Review Letters, **71**, pp. 189–192 (1993).
- [183] S. Gerlich, S. Eibenberger, M. Tomandl, S. Nimmrichter, K. Hornberger, P. J. Fagan, J. TÅxen, M. Mayor, and M. Arndt, *Quantum interference of large organic molecules*, Nat Commun, **2**, pp. 263– (2011).
- [184] A. O’Connell, M. Hofheinz, M. Ansmann, R. Bialczak, M. Lenander, E. Lucero, M. Neeley, D. Sank, H. Wang, M. Weides, et al., *Quantum ground state and single-phonon control of a mechanical resonator*, Nature, **464**, pp. 697–703 (2010).
- [185] G. Panitchayangkoon, D. Hayes, K. Fransted, J. Caram, E. Harel, J. Wen, R. Blankenship, and G. Engel, *Long-lived quantum coherence in photosynthetic complexes at physiological temperature*, Proceedings of the National Academy of Sciences, **107**, p. 12766 (2010).
- [186] E. Collini, C. Y. Wong, K. E. Wilk, P. M. G. Curmi, P. Brumer, and G. D. Scholes, *Coherently wired light-harvesting in photosynthetic marine algae at ambient temperature*, Nature, **463**, pp. 644–647 (2010).
- [187] K. S. Choi, H. Deng, J. Laurat, and H. J. Kimble, *Mapping photonic entanglement into and out of a quantum memory*, Nature, **452**, pp. 67–71 (2008).
- [188] K. C. Lee, M. R. Sprague, B. J. Sussman, J. Nunn, N. K. Langford, X.-M. Jin, T. Champion, P. Michelberger, K. F. Reim, D. England, D. Jaksch, and I. A. Walmsley, *Entangling Macroscopic Diamonds at Room Temperature*, Science, **334**, pp. 1253–1256 (2011).

- [189] G. Milburn, *Quasi-probability methods for multimode conditional optical gates (Invited)*, JOSA B, **24**, pp. 167–170 (2007).
- [190] G. Boreman, *Basic Electro-Optics for Electrical Engineers*, Tutorial Texts in Optical Engineering, SPIE Optical Engineering Press (1998).
- [191] S. Pancharatnam, *Achromatic combinations of birefringent plates*, Proceedings Mathematical Sciences, **41**, pp. 137–144 (1955), 10.1007/BF03047098.
- [192] M. V. Berry, *Quantal Phase Factors Accompanying Adiabatic Changes*, Proceedings of the Royal Society of London. A. Mathematical and Physical Sciences, **392**, pp. 45–57 (1984).
- [193] N. K. Langford, *Encoding, manipulating and measuring quantum information in optics*, Ph.D. thesis, School of Physical Sciences, University of Queensland (2007).
- [194] V. Vedral, *Quantifying entanglement in macroscopic systems*, Nature, **453**, pp. 1004–1007 (2008).
- [195] V. Vedral, M. B. Plenio, M. A. Rippin, and P. L. Knight, *Quantifying Entanglement*, Phys. Rev. Lett., **78(12)**, pp. 2275–2279 (1997).
- [196] W. Wootters, *Entanglement of formation of an arbitrary state of two qubits*, Physical Review Letters, **80**, pp. 2245–2248 (1998).
- [197] G. J. Feldman and R. D. Cousins, *Unified approach to the classical statistical analysis of small signals*, Phys. Rev. D, **57**, pp. 3873–3889 (1998).
- [198] J. O. Berger, *The Case for Objective Bayesian Analysis*, Bayesian Analysis, **1**, pp. 385–402 (2006).
- [199] M. Goldstein, *Subjective Bayesian Analysis: Principle and practice*, BAYESIAN ANALYSIS, **1**, pp. 403–420 (2006).
- [200] S. E. Fienberg, *Does it Make Sense to be an “Objective Bayesian”? (Comment on Articles by Berger and by Goldstein)*, Bayesian Analysis, **1**, pp. 429–432 (2006).
- [201] D. F. V. James, P. G. Kwiat, W. J. Munro, and A. G. White, *Measurement of qubits*, Phys. Rev. A, **64**, p. 052312 (2001).
- [202] D. Deutsch, *Quantum Theory, the Church-Turing Principle and the Universal Quantum Computer*, Proceedings of the Royal Society of London. Series A, Mathematical and Physical Sciences (1934-1990), **400**, pp. 97–117 (1985).
- [203] A. K. Ekert, *Quantum cryptography based on Bell’s theorem*, Phys. Rev. Lett., **67**, pp. 661–663 (1991).

- [204] P. Shor, *Algorithms for quantum computation: Discrete logarithms and factoring*, Proceedings of the 35th Annual Symposium on Foundations of Computer Science, **124** (1994).
- [205] L. K. Grover, *A Fast quantum mechanical algorithm for database search* (1996), proceedings STOC 1996, 212-219.
- [206] J. Clarke and F. K. Wilhelm, *Superconducting quantum bits*, Nature, **453**, pp. 1031–1042 (2008).
- [207] J. Cirac and P. Zoller, *Quantum computations with cold trapped ions*, Physical Review Letters, **74**, pp. 4091–4094 (1995).
- [208] A. Nizovtsev, S. Kilin, F. Jelezko, T. Gaebel, I. Popa, A. Gruber, and J. Wrachtrup, *A quantum computer based on NV centers in diamond: Optically detected nutations of single electron and nuclear spins*, Optics and Spectroscopy, **99**, pp. 233–244 (2005), 10.1134/1.2034610.
- [209] J. D. Teufel, T. Donner, D. Li, J. W. Harlow, M. S. Allman, K. Cicak, A. J. Sirois, J. D. Whittaker, K. W. Lehnert, and R. W. Simmonds, *Sideband cooling of micromechanical motion to the quantum ground state*, Nature, **475**, pp. 359–363 (2011).
- [210] J. Chan, T. P. M. Alegre, A. H. Safavi-Naeini, J. T. Hill, A. Krause, S. Groeblacher, M. Aspelmeyer, and O. Painter, *Laser cooling of a nanomechanical oscillator into its quantum ground state*, ArXiv e-prints (2011).
- [211] F. Marquardt and S. M. Girvin, *Optomechanics*, Physics, **2**, p. 40 (2009).
- [212] F. C. Waldermann, B. J. Sussman, J. Nunn, V. O. Lorenz, K. C. Lee, K. Surmacz, K. H. Lee, D. Jaksch, I. A. Walmsley, P. Spizziri, P. Olivero, and S. Praver, *Decoherence measurement of single phonons using spectral interference*, ArXiv e-prints (2008).
- [213] P. J. Bustard, D. Moffatt, R. Lausten, G. Wu, I. A. Walmsley, and B. J. Sussman, *Quantum random bit generation using stimulated Raman scattering*, Opt. Express, **19**, pp. 25173–25180 (2011).
- [214] M. Stroschio and M. Dutta, *Phonons in Nanostructures*, Cambridge University Press (2001).